Properties of magnetically doped topological insulator thin films

Memory presented by

Martha Lasia

Instituto de Ciencias de Materiales

de Madrid (CSIC)

to receive the title of

Doctor in Physics

at the University Autonóma Madrid

Faculty of Science

Madrid, October 2014

Acknowledgments

First of all, I would like to thank my advisor, Professor Luis Brey, for directing this Ph.D. thesis. I am deeply grateful for his scientific guidance, for his advice and support.
I am grateful to the members of our research group at the ICMM. I want to thank Professor Maria Jose Calderon and Professor Ramon Aguado, for the all the help I received when starting my PhD. thesis and for their patience and support with all the documents which had to be done.
I want to thank the people at Nordita in Stockholm, where I spend nearly six months of estancia breve. It was an important experience for me and I am grateful for their support and hospitality. I especially want to thank Professor Alexander V. Balatsky for his scientific guidance and the many scientific opportunities he gave me at Nordita.
The results presented in this thesis have been developed in the framework of the research projects: FIS2009-08744: Quantum effect and correlations in nano structures for information processing and storage, Instituto Sciencia y Maeteriales de Madrid (ICMM) - CSIC, Project director: Luis Brey (ICMM), Founding: Ministerio de Ciencia y Innovacion (Spanish Ministry of Science) MICINN-Spain via Grant FIS2009-08744 and MEC-Spain via grant FIS2012-33521.

The thesis was realised during four years of the following scholarship: 1. September 2010 - 31. August 2014: Beca FPI BES-2010-033307, Ministerio de Ciencia e Innovación, ICMM.

Contents

II

III

Appendix

CHAPTER 0

Introducción y Conclusión

0.1 Aislantes topológicos

Aislantes topológicos son estados únicos de la materia que son aislantes en el bulk con estados metálicos en la superficie. El estado topológico más simple que no es trivial es el estado cuántico Hall, donde los electrones de velocidades oportunas estn separados por el bulk y el sistema se caracteriza por una conductividad Hall que no es zero. La primera observación experimental de aislantes topológicos se hizo en los pozos cuánticos de HgTe. Aislantes topológicos de tres dimensiones y cintas finas de aislantes topológicos están utilizado para observar las propiedades de transporte y ópticas de los estados superficiales metálicos.
En los siguientes captulos presentare un sumario de mis publicaciones.

0.2 El aislante topologico Bi_2Se_3 dopado con impurezas magnéticas a temperaturas finitas

Teoría

En la primera publicación estudiamos las propiedades magnéticas de Bi2Se3 dopado con impurezas magnticas isoelectrónicas. Obtenemos que a temperatura cero las impurezas se orden ferromagnéticamente, pero cuando sube la temperatura del sistema el sistema experiencia una transición de fase de primer orden a una fase de spin-density-wave antes de

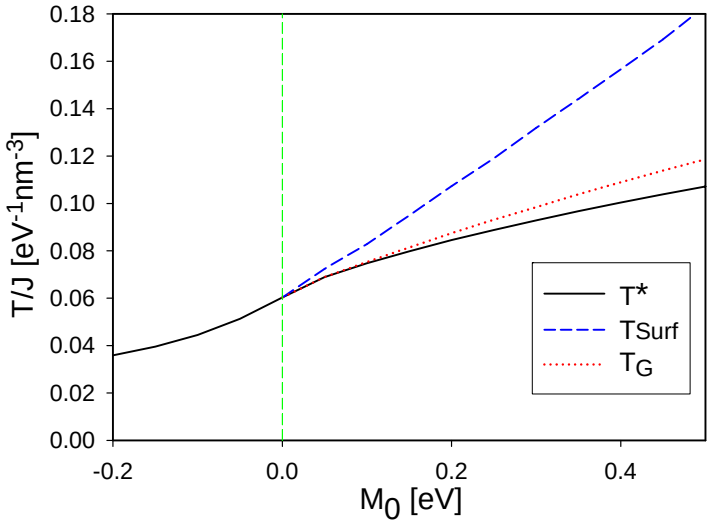

El diagrama de la fase de un TI dopado con impurezas magnéticas como una funcón del parametro M_0.

que el sistema llega a la fase paramagnética. El origen de esta fase es la dependencia no trivial de la susceptibilidad de spin en el momento. Ademas analizamos el acoplamiento de la fase magnética no uniforme con el sistema electrnico de Dirac que se produce en las superficies del aislante topologico.

Conclusión

En conclusion hemos estudiado el diagrama de fase de Bi_2Se_3 dopado con impurezas magnéticas. A temperaturas bajas las impurezas magnticas orden ferromagnéticamente en la dirección z. Elevando la temperatura, el TI se somete a dos transiciones. Una transición del primer orden de la fase ferromagnética a la fase de spin-density-wave y cuando se sube la temperatura mas ocurre una transición del segundo orden a la fase paramagnética. Este resultado podría explicar experimentos recientes que sugieren la existencia, como función de temperatura, de dos fases magnóeticas diferentes in Bi_2Se_3 dopado con Fe. Hemos estudiado también el efecto de los estados superficiales calculando la magnetización como función de la temperatura de una lámina de Bi_2Se_3 aislante

topológico. Hemos encontrado que la magnetización de la superficie sobrevive hasta unas temperaturas mas altas que la fase spin-density-wave de la lámina. La existencia de un rango de temperaturas para las que la magnetización mayor prácticamente desaparece, mientras que existe una magnetización finita en la superficie, podría explicar algunos resultados experimentales que observan un gap en la superficie de Bi_2Se_3 pero sin magnetización de la lámina [45, 47]. Es importante analizar el comportamiento del diagrama de fases como una función del parámetro del gap M_0. En la Fig. 2.7 mostramos el diagrama de fases de una lámina de un TI magnéticamente dopado como una función de M_0. Para $M_0<0$ el sistema es un aislante normal y no hay estados de la superficie. También el acoplamiento spin-órbita es pequeño y la fase SDW no existe. Para $M_0>0$ el sistema es un del TI y el gap aumenta con M_0. TI con gaps ms grandes tienen ms estados superficiales metlicos y por lo tanto el orden de FM en la superficie es más robusto. Tambin el acoplamiento eficaz spin-órbita es ms fuerte y T y T_G aumentan con M_0. Los resultados en la Fig. 2.7 muestran que el rango de temperaturas donde existe la fase de SDW aumenta con M_0. Finalmente, hacemos una estimacin de la temperatura crtica. A partir de los parámetros de la estructura de banda de Bi_2Se_3, elegimos la densidad de las impurezas magnéticas como $5x10^{20}cm^{-3}$, el momento angular total de un solo ion magntico es S = 3/2, y el acoplamiento de cambio efectivo Nm^3 J_{eff} = 250meV y obtenemos T^G_{bulk}=18K. Estos valores pueden cambiar por factores de 2 cambiando los iones magnéticos o la densidad de impurezas. Es bien sabido que las aproximaciones mean-field tienden a sobreestimar la temperatura de transicin debido a la negligencia de las fluctuaciones. En los semiconductores magnéticos diluidos fluctuaciones térmicas reducen el valor de la temperatura de Curie aproximado de 30% [58], y esperamos una reduccin similar en aislantes topológicos.

0.3 El efecto magnéto-eléctrico iso-eléctronico en aislantes topológicos y materials multiferroicos

Teoría

Durante mi estancia breve en Estocolmo hemos estudiado la posibilidad de monopolos magnéticos en materiales multiferroicos. Una carga eléctrica en el centro de un vaco esférico rodeado por un material multi-

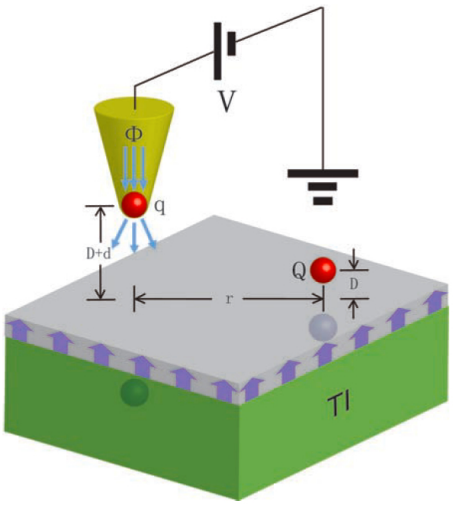

Illustración de un setup experimental para observar un monopol magnético, Qi *e*t al. [28].

ferroico induciría un monopolo magnético imagino por el efecto magneto-eléctrica. El campo magnético del monopolio podría ser medido experimentalmente. Se estudia la evolución temporal de la magnetización y la polarización para esta configuración y calculamos la frecuencia angular en el caso de un sistema dinámico.

Conclusión

Hemos incluido dependencias temporales a las ecuaciones constitutivas para calcular el efecto magneto-eléctrico dinámico. En relacin con la teora eléctro-magneto hemos calculado las ecuaciones dinámicas de la magnetización y polarización.

0.4 Propiedades ópticas de laminas finas de aislantes topológicos

Teoría

En la ultima publicación usamos el Hamiltonian de tres dimensiones y estudiamos las propiedades ópticas de laminas ultra-finas de aislantes topológicos donde el acoplamiento entre fermiones de Dirac en superficies opuestas resultado en dos bandas hiperbólicas degenarados con

gaps. El gap es un umbral para la absorción óptica y resulta en un pico en la parte imaginaria de la conductividad óptica. Un campo de Zeeman aplicado perpendicular a la lamina divide las bandas hiperbólicas degeneradas y una estructura de doble paso aparece en la absorción óptica, mientras que aparece una estructura de doble pico en la parte imaginaria de la conductividad óptica longitudinal. El campo Zeeman rompe la simetra de inversión temporal y para los campos de Zeeman más grande que el gap de las superficies de acoplamiento, la zero frecuencia de la conductividad Hall esta cuantificada a e^2/h. Este resultado implica grandes valores del ángulo de rotación Kerr y una cuantificación del ángulo de Faraday. En laminas ultra finas, la ausencia de dispersión múltiple de la luz y la conductividad de bulk, hace que el ángulo Kerr permanezca bastante grande en un rango amplio de frecuencias.

Conclusión

Hemos estudiado la estructura de bandas y las propiedades ópticas de laminas ultra-finas de aislantes topológicos. Para que nuestros cálculos no dependen del cutoff de la energía hemos usado un k.p Hamiltonian en tres dimensiones y obtenemos las propiedades electrónicas. Para la conductividad óptica hemos usado la expresión abajo que describe correctamente los contribuciones diamagnéticos y paramagnéticos y hemos obtenido directamente los partes reales y imaginarias de la conductividad de ella.

$$\sigma_{\alpha,\beta} = i\frac{e^2\hbar}{V}\int \frac{d^2\mathbf{k}}{(2\pi)^2}\sum_{m,n}\frac{n_F(\varepsilon_{n,\mathbf{k}})-n_F(\varepsilon_{m,\mathbf{k}})}{\varepsilon_{m,\mathbf{k}}-\varepsilon_{n,\mathbf{k}}}\frac{<n,\mathbf{k}|j_\alpha|m,\mathbf{k}><m,\mathbf{k}|j_\beta|n,\mathbf{k}>}{\hbar(\omega+i\eta)-(\varepsilon_{m,\mathbf{k}}-\varepsilon_{n,\mathbf{k}})}$$

En laminas ultra-finas de aislantes topológicos el acoplo entre estados superficiales opuestos abre un gap en el espectro electrónico que inhibe una absorción óptica para frecuencias menor que el gap E_g. El gap esta reflejado en un pico en la parta imaginaria de $\sigma_{xx}(\omega)$. Este pico indica la existencia de una excitación de carga inter-banda.
Un campo Zeeman z appliquéd perpendicularmente a las laminas del TI, rompe la simetria de inversion temporal y separa las bandas con gap de los laminas ultra-finas. La parte real de la conductividad óptica longitudinal muestra bordes de absorción a energas $2\Delta_z \pm E_g$, mientras que la parte imaginaria muestra picos a las mismas energías. Para valores del campo Zeeman $2\Delta_z > E_g$, la zero frecuencia de la conductividad Hall esta cuantificada a $\sigma_{xy} = e^2/h$. Ese valor grande de la conductividad Hall produce una rotación grande de la polarización de la luz cuando se transmite o refleja en la lamina del TI.

A frecuencia zero el ángulo Faraday tiene el valor $\theta_F = e^2/\hbar c = 1/137$ y presenta un pico a frecuencias $2\Delta_z \pm E_g$. La rotación Kerr tiene el valor$\theta_K = -\pi/2$ en frecuencia zero y valores absolutos grandes en frecuencias finitas.
Los valores de los ángulos de rotación Faraday y Kerr son bastante robustas porque nos son afectadas por portadores del bulk o por dispersion multiple de la luz en la lamina ultra-fines des los aislantes topológicos.

CHAPTER 1

Introduction

Topological insulators are unique states of matter which are insulating in the bulk but have metallic states on the surface. The simplest topological non-trivial state is the quantum Hall state where electrons of opposite velocities are separated by a bulk and the system is characterised by a non-vanishing Hall conductivity. The first experimental observation of topological insulators was made in HgTe quantum wells. Three dimensional topological insulators and thin films of topological insulators are used to observe transport and optical properties of the metallic surface states.
In the following part of this chapter I will start with an introduction to the topic of topological insulators and describe the differences in two and three dimensions as well as describe the importance of topological insulators as a research field in the future.

1.1 Topological insulators in two and three dimensions

Band insulators and topological insulators

Topological insulators have been the research topic of great interest and high hopes for future applications for the last decade. The first theoretical prediction goes back to 1986, when time-reversal symmetry protected edge states were expected to exist in quantum wells. In 2007 this prediction was realised in HgTe quantum wells.
In this introduction I want to show the development that led from the dis-

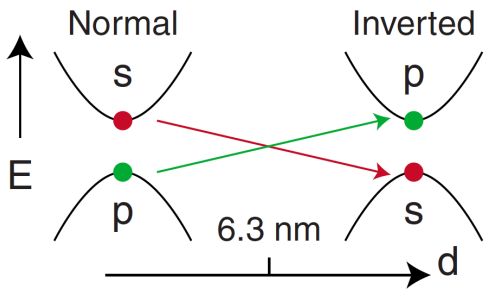

Figure 1.1: Band structure as a function of quantum well thickness for HgTe [1]. In the normal band structure the valence band (vb) comes from p (p-orbitals) states while the conduction band (cb) comes from s (s-orbitlas) states. In the inverted band structure the vb is made of s states and the cb of p states. For HgTe quantum wells the bands invert at a critical thickness of 6.3nm.

covery of the Hall effect in 1879 to the first topological insulators in three dimensions and finish with an outlook on the future of applications of topological insulators. I will introduce the quantum spin Hall effect and talk about the first topological insulator HgTe. I will show how magnetic impurities effect the surface states of topological insulators and talk about thin films of topological insulators.
To start the introduction I chose the simplest state of matter which is the insulating state. In band insulators the electrons are confined in the valence band, which is separated from the conduction band by a band gap. There are no low-energy excitations which could make the electrons overcome this large band gap. Therefore the entire system is insulating.
In a topological insulator relativistic effects modify the band structure which turns out differently from the band structure of an insulator. Spin-orbit coupling leads to an inversion of the valence and conduction bands. Metallic surface states appear at an interface between a system with such inverted band structure and a trivial insulator (vacuum).
In weak topological insulators the surface states can be described by a single Dirac cone sitting at a high-symmetrical point (in the centre) of the Brillouin zone. These surface states are protected by time-reversal symmetry and a gap only opens when perturbations of magnetic character are introduced on the surface.The robustness of the surface states in a topological insulator is what distinguishes its topology from this of a trivial insulator.

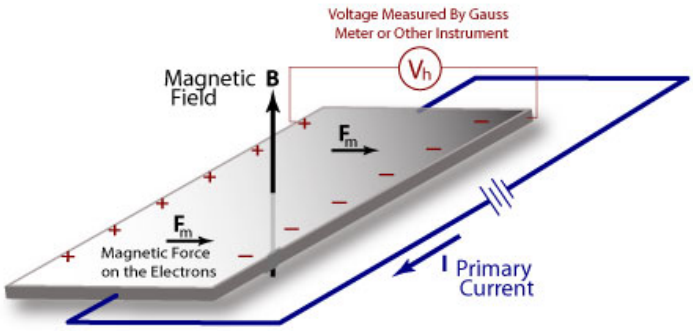

Figure 1.2: Schematic picture of the Hall effect. A current flows from the front to the back while a perpendicular magnetic field is applied. The field separates the charges and pushes the negative carriers on one side making a measurable current flow from left to right. Picture by [2].

The first example of a topological non-trivial state of matter is the integer quantum Hall (QH) state.

The quantum Hall insulator

The Hall effect

An electrical current flowing through a conductor in a magnetic field feels a transverse force which pushes the carriers to one side. As seen in Fig.1.2 the positive charges are separated from the negative charge carriers. While the different charge carriers accumulate on the different sides, a voltage between the two sides of the conductor is measured (in the figure the carriers move from left to right). This effect was discovered by E. Hall in 1879.
The Hall resistivity is given by,

$$\rho_{xy} = \frac{B}{en_q}, \tag{1.1}$$

with B the applied magnetic field, e the charge of the electron and n_q the density of the charged particles.

The quantum Hall effect

Around hundred years later von Klitzing [3] discovered that in a high mobility two-dimensional electron gas, at an interface with a semiconductor material, a strong enough magnetic field leads to plateaus in the Hall resistivity ρ_{xy}. At each of the plateaus the longitudinal resistivity ρ_{xx} and conductivity σ_{xx} vanish by many orders of magnitude see Fig.1.3. The Hall resistance varies stepwise with the magnetic field and each step height is given by h/e^2.
The energy of the electrons in the electron gas can be described by the theory of Landau where charged particles in a uniform magnetic field have a quantised energy, the Landau levels $E_n = \hbar\omega_c(n + 1/2)$ with $n = 0, 1, 2, ...$ and ω_c the cyclotron frequency.
Each Landau level is degenerate and the number of states per unit area in a Landau level is given by $\frac{eB}{2\pi\hbar c}$. Instead of a linear function for the resistivity and conductivity they are now quantised and given by $\rho_{xy} = h/(Ne^2)$ and $\sigma_{xy} = Ne^2/h$, where N is the number of occupied Landau levels in the system.
Von Klitzings team was not the first to predict or experimentally observe a quantisation of the Hall conductance. Ando, Matsumoto and Uemura [4] were the first to calculate the quantisation in 1975 but did not believe their own theoretical predictions. Experiments on MOSFETs (metal-oxide-semiconductor transistor) confirmed the theoretical results, but von Klitzing was the first to show the exact quantisation of the Hall conductivity and he received the Nobel prize for his discovery in 1985.
σ_{xy} and σ_{xx} are very precise quantities up to a precision of 10^{-7}. They are robust against non-magnetic perturbations and changes in the magnetic field.
The non-zero Hall conductivity σ_{xy} indicates that the topology of the integer quantum Hall (IQH) state is different than the topology of the trivial insulator where $\sigma_{xy} = 0$.

TKNN Invariant

Another way to distinguish between the topology of a normal insulator and the IQH state was given by Thouless, Kohmoto, Nightingale and den Nijs in 1982 [5]. They classified the different topologies by different Chern numbers or TKNN invariants.
The TKKN invariant distinguishes classes of materials by topology. Those kind of materials which can be continuously deformed into each other

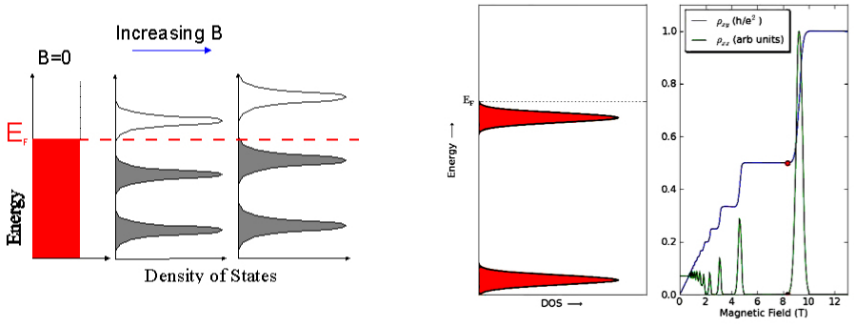

Figure 1.3: On the left: Landau levels for magnetic fields of different strengths. If the Fermi energy E_F lies between two Landau levels a gap opens and the systems becomes an insulator. On the right: The Hall resistance depending on the magnetic field. For small magnetic fields the Hall resistance behaves linear with the magnetic field up until a certain field strength. Plateaus appear and the quantised behaviour of σ_{xy} is visible. σ_{xx} goes to zero at each plateau. Figure via wikipedia.org.

without closing the energy gap belong to the same class. A band insulator has Chern number zero while a topological insulator has Chern number different to zero. It can only change at a quantum phase transition where the energy gap goes to zero. In two dimensions the Chern number also indicates the number of edge states in the system. The Chern number ν is directly related to the Hall conductivity by the following formula [6]:

$$\sigma_{xy} = \frac{e^2}{h} \sum_{n_{occ.}} \int \frac{dk}{2\pi} \nabla \gamma_n(\mathbf{k}) = \nu \frac{e^2}{h}, \tag{1.2}$$

where k is the momentum, $n_{occ.}$ is the density of the occupied states and γ_n is the phase of the wave function around the boundary of the magnetic Brillouin zone. Comparing this formula with the above equation for the quantum Hall conductivity we see that the Chern number ν is equal to N, the number of occupied Landau levels.

Edge States in the quantum Hall (QH) system

The appearance of edge states can be understood by looking at an interface between an insulator and a quantum Hall state, both have different

topological invariants. At the interface the invariant has to change, in other words the gap has to close and this is where gapless edge states appear [1]. In the QH system the edge or surface states are protected against backscattering and the Hall conductivity σ_{xx} is equal to zero. The reason is that states at the interface propagate in one direction only at the edge, they are chiral. There are no states available for backscattering in this system. The wave functions of the electrons on different surfaces do not overlap and this protection against backscattering results in a non-zero Chern number.
Soon after the quantum Hall state with external magnetic field was realised, new models like the Haldane model (1988) [7] proposed the QH effect without magnetic field. The Haldane model contains spinless fermions on the two-dimensional honeycomb lattice with an inhomogenous magnetic field.
Another possible model without an external magnetic field is a combination of two QH systems with opposite magnetic fields. The sum of these fields would give zero net field but also zero net Hall conductivity and therefore zero Chern number. The protection of the edge states would be lost and the system would be topologically equivalent to a trivial insulator.
Kane and Mele [8] came up with a model that restores time-reversal symmetry by adding spin-dependencies and restoring the spin degree of freedom. A gap is induced by spin-orbit coupling and the edge states are protected by the Kramer's theorem. This model is known as the quantum spin Hall effect and it led to the discovery of the first topological insulator in two dimensions HgTe.

1.2 HgTe a topological insulator in two dimensions

Quantum spin Hall (QSH) effect

The QH effect occurs in layered materials at high magnetic fields and results from the formation of conducting one-dimensional channels that develop at the edge of the sample [9]. Each of these edge channels exhibits a quantised conductance directly related to the values of the QH conductance. The QH state is the first topologically non-trivial state, where the quantisation of the Hall conductance is protected by a topological invariant.
Transport in the edge channels happens dissipationless but the exper-

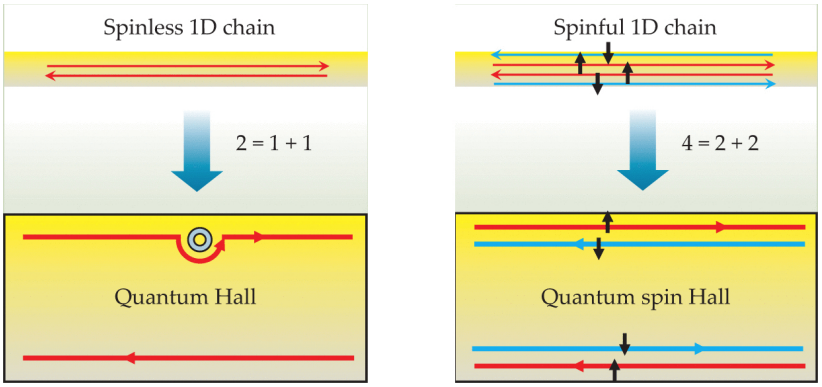

Figure 1.4: On the left the carriers on different edge channels in the QH insulator move in opposite directions. An impurity located in the edge channels doesn't change the direction of the carrier as there is nowhere the carrier can backscatter into. On the right in the QSH insulator the forward and backward moving carriers at a given edge in each channel have opposite spin. The edge channels are spatially separated and the edge states are protected against backscattering by TR symmetry. Figure by [10]

imental downside of the QH effect is that it appears at high magnetic fields and low temperatures.
The quantum spin Hall phase is a time-reversal symmetry protected electronic state with a bulk gap and metallic states on the edges. Those states support the transport of charge and spin. The quantum spin Hall effect (QSHE) occurs without an external magnetic field.
The first model for the QSHE was given by Kane and Mele [8] and it was realised for the first time in mercury telluride quantum wells.
Independent models for the intrinsic spin Hall effect were given by Murakami, Bernevig and Zhang [11] as well as Sinova et al.[12]. The last authors are not talking about a *quantum* spin Hall effect as there is no quantisation of the spin Hall current. The term quantum comes from a non-zero net spin accumulation on the sample edge when an electric field is applied. In an insulator this would be zero. For the QSH effect the net Hall conductance is the sum of the Hall conductances for electrons with spins pointing up and down . They are of the same value but with opposite signs. The sum of the Hall conductances is zero. The spin-Hall

conductance is given by:

$$\sigma_{xy} = 2\frac{e}{4\pi}, \tag{1.3}$$

with e the electron charge.
The QSH state is a non-trivial state unlike the insulating state. A Z_2 topological invariant was introduced by Kane and Mele [13] to distinguish those two states of matter topologically.
Compared to the QH state, the QSH state posses edge channels with forward and backward moving carriers which have opposite spin on each edge. Those states are protected against backscattering by time-reversal (TR) symmetry. Kane and Mele showed that backscattering in a QSH insulator would be odd under TR symmetry and only when TR is broken backscattering can appear in the QSH insulator.
QSH insulators have a charge excitation gap in the bulk, while the edge states are gapless and topologically protected and lie in the bulk insulation gap.
Those edge states underlie the Kramer-theorem which states that for every energy eigenstate of a time-reversal symmetric system with half-integer total spin, there is at least one more eigenstate with the same energy. In other words, every energy level is at least doubly degenerate if it has half-integer spin. The spin up and spin down states in each edge channel counter propagate which results in a filtering of the spins. Behaving like this the edge states in the QSH system are called helical [14]. For each energy in the QSH state there exists a single pair of time reversed eigenstates on each edge. TR symmetry prevents the mixing of the Kramer doublets and the edge states are robust against small perturbations. Backscattering of single particles is forbidden. In contrary in the insulating state the edge states do not cross the gap. If there should be states crossing the gap, there is an even number of Kramer pairs for each energy. This allows elastic backscattering and the edge states will be localised by weak disorder [13].
Instead of a Chern number as in the QH state, the topological properties of the QSH state are mathematically characterised by the Z_2 topological invariant [13].

$$P(\mathbf{k}) = Pf[\langle u_i(\mathbf{k})|\Theta|u_j(\mathbf{k})\rangle], \tag{1.4}$$

is the Pfaffian which describes the subspace where Kane et al. classified the Z_2 invariant for the QSH state. $\Theta|u_i(\mathbf{k})\rangle$ is orthogonal to the space spanned by $|u_i(\mathbf{k})\rangle$.The energy levels of the edge states cross at special points in the Brillouin zone due to time-reversal symmetry. This crossing protects the system from being adiabatically deformed into the same

topological class as a trivial insulator [13].
The QSH state has intrinsic topological order which means that it can be robust against any local perturbation which conserves TR symmetry.
Realising the QSH state would result in stable helical edge state channels without an applied magnetic field. It would allow direct manipulation of the spin degrees of freedom without a magnetic field so that the spin current can flow dissipationless. This kind of transport could have a great impact on improving the information processing in superconductor chips.
The QSH effect opens the field for spin based electronic devices based on the properties of the edge channels. These devices, which integrate information processing and storage units, could operate with low power consumption and perform reversible quantum calculations [15].

HgTe

To observe the QSH effect it is essential to have a material with the right structural properties. König *e*t al.[16] observed that samples made from narrow quantum wells with a non-inverted, normal, electronic structure show zero conductance when the Fermi level is inside the gap. Quantum wells with an inverted electronic structure like HgTe show a conductance near what is expected for the edge channel transport in a quantum spin Hall insulator.
HgTe has a negative band gap of -300meV as a result of the band inversion of the conductance and valence band. The quantum well used to experimentally observe the QSHE is HgTe/($Hg_{0.3}Cd_{0.7}$)Te. Both HgTe and CdTe have the important bands near the Fermi level close to the Γ-point in the Brillouin zone. In Fig.1.5 these bands were given the notation Γ_6 for the s-type band and Γ_7 and Γ_8 for the p-type bands, which are split by spin-orbit coupling [9].
In HgTe the Γ_8, which normally forms the valence band, lies above the Γ_6 band. At a critical thickness these three bands Γ_6, Γ_7 and Γ_8 are pushed into different positions and this kind of band structure is called inverted.
The effective Hamiltonian for a HgTe quantum well can be written as follows [16]:

$$H_{eff}(k_x, k_y) = \begin{pmatrix} H(\mathbf{k}) & 0 \\ 0 & H^*(-\mathbf{k}) \end{pmatrix}, \tag{1.5}$$

$$H(\mathbf{k}) = \epsilon(\mathbf{k}) + d_i(\mathbf{k})\sigma_i \tag{1.6}$$

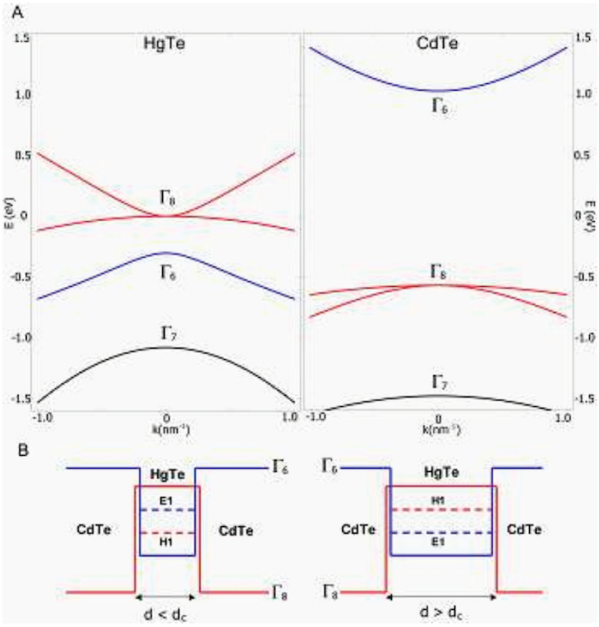

Figure 1.5: Bandstructure for the HgTe/($Hg_{0.3}Cd_{0.7}$)Te quantum wells. On the left the insulating state with non-inverted band structure for thicknesses $d < d_c$. On the right the inverted bandstructure of HgTe for thickness $d > d_c$. It is possible experimentally to change the width of the quantum well and go from an inverted band structure $(d > d_c)$ to a normal (insulating) band structure $(d < d_c)$. d_c is the critical thickness at which the semiconductor changes it's topological properties. Figure by [9].

where σ_i are the Pauli matrices and

$$d_1 + id_2 = A(k_x + ik_y) = Ak_+, \tag{1.7}$$

$$d_3 = M - B(k_x^2 + k_y^2), \tag{1.8}$$

$$\epsilon_k = C - D(k_x^2 + k_y^2), \tag{1.9}$$

where, k_x and k_y are momenta in the plane of the two-dimensional electron gas (2DEG), and A, B, C, D and M are material specific constants and M depends on the quantum well geometry. Depending on the signs of M and B the system is a topological insulator or in an insulating state. For $M/2B > 0$ the system is TI. **k**=(k_x,k_y) and $k_\pm$=$k_x \pm ik_-$.

The electronic structure of the semiconductor HgTe is inverted when

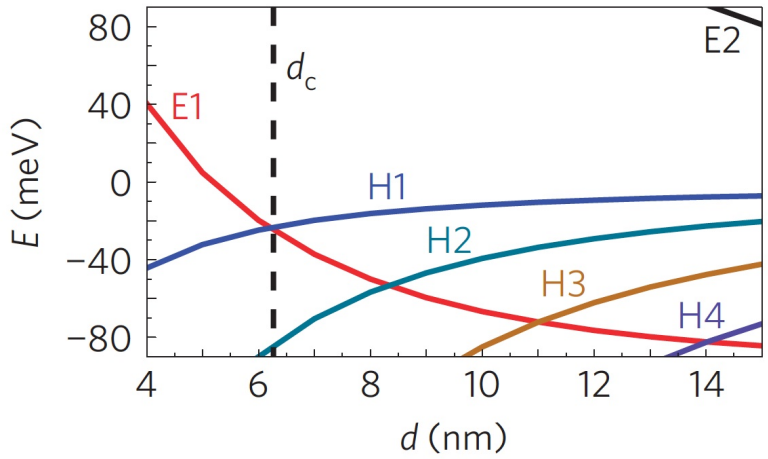

Figure 1.6: Subband energies of HgTe/($Hg_{0.3}Cd_{0.7}$)Te quantum wells as a function of well thickness d [17]. The inversion between the E1 and H1 subbands leads to the occurrence of the quantum spin Hall effect where dissipationless edge channel transport at zero external magnetic field occurs.
Reducing the thickness of the quantum well leads to an increase of the energy of the E1 sub band while the energy of the H1 sub band decreases. At critical thickness $d = d_c$ the inversion of the bands is lifted and the system turns into a normal insulator. In [17] this quantum phase transition appears at d_c=6.3nm. At this point the low-energy band structure of the system is close to that of a massless Dirac Hamiltonian.

the thickness is large enough and the s-like orbitals (E1 sub bands) lie below the p-like orbitals (H1 sub bands) (see Fig.1.6). Due to this the Dirac mass parameter M in the HgTe/(Hg,Cd)Te quantum wells can be continuously tuned from a positive value for thin quantum well with $d < d_c$ to a negative value for thick quantum wells with $d > d_c$. When doing so a topological quantum phase transition at $d = d_c$ occurs. At this point the system can be described by a massless Dirac theory.
The sample edge can be viewed as a domain wall of the mass parameter M which separates the topological non-trivial phase from the topological trivial phase at $M > 0$, which is adiabatically equivalent to the vacuum.
The edge states are protected against back-scattering by time-reversal symmetry. Therefore also the edge state conductance should be robust against local perturbations. If a magnetic field is present the time-reversal

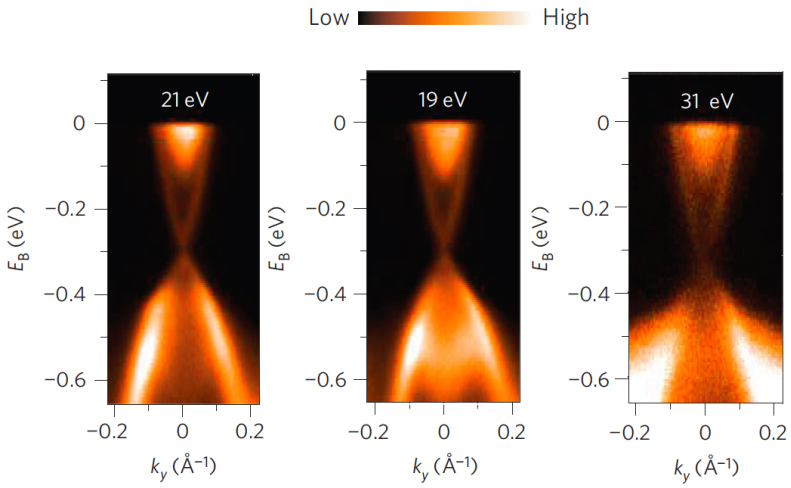

Figure 1.7: Experimental observation of a Dirac cone for different energies. Fig by [18].

symmetry breaks and a gap opens in the energy spectrum. The conductance disappears when a gap is opened.
Zero-gap HgTe quantum wells are unique because they realise a single-valley, spin-degenerate Dirac system. It is also possible to observe Dirac fermion physics to very high mobilities (up to 1.5 x 10^6 cm^{2}V$-$1s^{-1}) [17].

1.3 Bi_2Se_3 a topological insulator in three dimensions

To find topological insulators in three dimensions one searches for materials where the conductance and valence bands have opposite parities so that a parameter can be tuned to create a band inversion, this parameter is the spin-orbit coupling (SOC)[19].
The surface states of these three dimensional topological insulators consist of an odd number of massless Dirac cones. This is determined by the Z_2 topological invariant of the bulk.
Without breaking time-reversal symmetry it is not possible to open a gap in the system. Applying a magnetic field breaks TR symmetry and a gap opens at the surface.
The three dimensional topological insulator Bi_2Se_3 has a bulk band gap

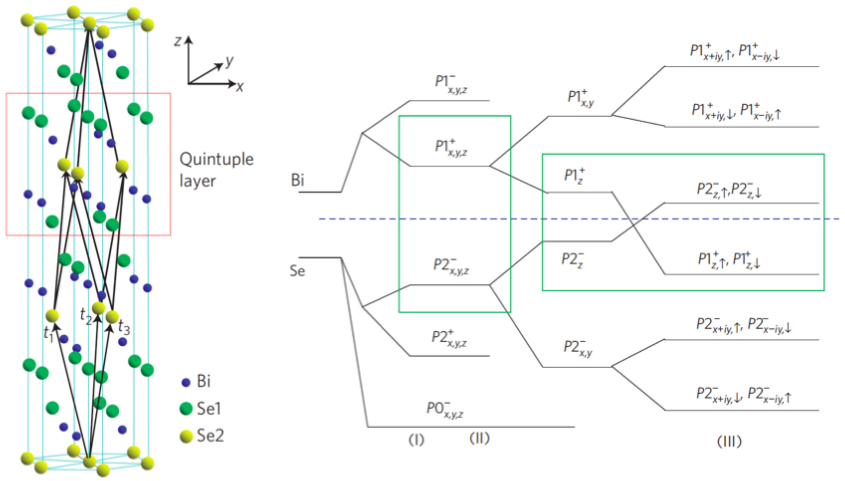

Figure 1.8: On the left the crystal structure of Bi_2Se_3 with three primitive lattice vectors denoted as $t_{1;2;3}$. The quintuple layer with is indicated by the red square. On the right the schematic picture for the band structure of Bi_2Se_3. I hybridisation of Bi and Se orbitals, II formation of the bonding and anti-bonding states due to the inversion symmetry, III the crystal field splitting, and IV SOC. Figure by [20]

of 0.3eV which is larger than the energy scale of room temperature. The surface states consist of a single Dirac cone at the k=0 Γ-point in the surface Brillouin zone.

Bi_2Se_3 has a rhombohedral crystal structure with the space group D^5_{3D} with five atoms per unit cell. In Fig.1.8 Bi_2Se_3 is shown. Its layered structure has a triangle lattice within one layer. The triangle axis with three-fold rotation symmetry is defined as z-axis, the binary axis with two-fold rotation symmetry is defined as x-axis and the bisectrix axis is defined as y-axis. Bi_2Se_3 is made up of five-atom layers arranged along the z-axis, the quintuple layers.

Each quintuple layer consists of two equivalent Se atoms, two equivalent Bi atoms and a third Se atom. Over all the system is very anisotropic. The

coupling within one quintuple layer is strong and much weaker between different quintuple layers.
The third Se atom serves as an inversion centre. The inversion symmetry makes it possible to construct eigenstates with definite parity for this system.
Looking at the right side of Fig.1.8 we find the band structure and the arrangement of the orbitals for Bi_2Se_3. The states near the Fermi surface mainly come from p orbitals. In the chemical bonding of Bi and Se the single orbitals are recombined by parity.
Hybridisation in (I) pushes the Se states down and lifts the Bi states up. In (II) the crystal field splitting effects the p orbitals. The p_z orbital is split from the $p_{x,y}$ orbitals. The p_z levels remain as the orbitals closest to the Fermi energy. At last the SOC in (III) leads to a level repulsion and the $|p1_z^+, \uparrow (\downarrow)\rangle$ state is pushed down while the $|p2_z^-, \uparrow (\downarrow)\rangle$ state is pushed up. For large SOC ($\lambda > \lambda_c$) this order is reversed.
The properties of the three dimensional topological insulator Bi_2Se_3 can be described by the four band Hamiltonian introduced by Zhang *et* al. [20]. They start from the four low-lying states given by $|p1_z^+, \uparrow (\downarrow)\rangle$ and $|p2_z^-, \uparrow (\downarrow)\rangle$ and consider the symmetries of the system as time-reversal symmetry T, inversion symmetry I and three-fold rotation symmetry C3 along the z axis. In the k.p approximation the low energy long wavelength properties of Bi_2Se_3 are determined by the Hamiltonian,

$$\begin{aligned} H^{3D} &= E(k) \\ &+ \begin{pmatrix} \mathcal{M}(k) & A_1 k_z & 0 & A_2 k_- \\ A_1 k_z & -\mathcal{M}(k) & A_2 k_- & 0 \\ 0 & A_2 k_+ & \mathcal{M}(k) & -A_1 k_z \\ A_2 k_+ & 0 & -A_1 k_z & -\mathcal{M}(k) \end{pmatrix}, \end{aligned} \tag{1.10}$$

where $\mathcal{M}(k)$=$M_0 - B_2(k_x^2 + k_y^2) - B_1 k_z^2$, $k_\pm$=$k_x \pm i k_y$ and $E(k)$=$C + D_1 k_z^2 + D_2(k_x^2 + k_y^2)$. The Hamiltonian is written in the basis $|1\rangle$=$|p1_z^+, \uparrow\rangle$, $|2\rangle$=$-i|p2_z^-, \uparrow\rangle$,$|3\rangle$=$|p1_z^+, \downarrow\rangle$, $|4\rangle$= $i|p2_z^-, \downarrow\rangle$, which are the hybridized states of the Se p orbital and the Bi p orbital with even $(+)$ and odd $(-)$ parities and spin up ($\uparrow$) and down ($\downarrow$). An important feature is that the two orbitals p_{1z}^+ and p_{2z}^- have opposite parities, so that the off-diagonal terms are linear in k_z and $k_\pm$.
The parameters are given as M_0=0.28eV, A_1=2.2$eV\mathring{A}$, A_2=4.1$eV\mathring{A}$, B_1=10$eV\mathring{A}^2$, B_2=56.6$eV\mathring{A}^2$, C=-0.0068eV,
D_1=1.3$eV\mathring{A}^2$ and D_2=19.6$eV\mathring{A}^2$. The surface states of Bi_2Se_3 can be de-

scribed by the following 2D Dirac Hamiltonian [20]:

$$H^{2D}_{Dirac} = E(\mathbf{k}) + v_f \begin{pmatrix} 0 & ik_x + k_y \\ -ik_x + k_y & 0 \end{pmatrix}. \tag{1.11}$$

with $v_f = A_2\sqrt{1 - \frac{D_1^2}{B_1^2}}$.
Depending on the sign of the parameters in the three dimensional model Hamiltonian (Eq. 1.10) the system is in a topological trivial or non-trivial state. A sign change in M flips the k-dependent spin configuration near the Γ point and results in a change of the Chern number and therefore in a topological quantum phase transition.
Since it's prediction as one of the first three dimensional topological insulators, many experiments on Bi_2Se_3 have confirmed it as one of the most promising TI materials. One of the more interesting recent experiments shows that the crossover of the three dimensional Bi_2Se_3 to two dimensions happens at a critical thickness of a few quantum layers.
Those experimental results by Zhang *e*t al. [21] show that Bi_2Se_3 grown by molecular beam epitaxy, behaves like a two dimensional topological insulator up to a layer thickness of 6 quantum layers (QLs). At the critical thickness of 6 QLs the system turns into a three dimensional TI. The reason that this crossover happens for a thin film of Bi_2Se_3 is because of quantum tunnelling between the boundary modes on opposite surfaces. As long as the thickness is thin enough the tunnelling opens a small gap between the surface states. Those surface states also exhibit Rashba-type spin-orbit splitting because of the induced potential difference on the opposite surfaces.
Such a combination of gap-opening and spin-orbit splitting makes this thin films great candidates for electronic and spintronic applications.

Topological surface states in three dimensions

Three dimensional topological insulators are a novel state of matter which are in a different topological class than the QH states and the conventional insulators.
The surface states are no longer defined by a single Z_2 invariant, the Chern number, as the Hall conductivity is zero. Instead there are four invariants distinguishing 16 phases with two general classes: weak (WTI) and strong (STI) topological insulators. Weak topological insulators can be seen as layered QSH states which can be easily destroyed by disorder. Strong topological insulators are those novel state of matters with topologically protected metallic surface states.

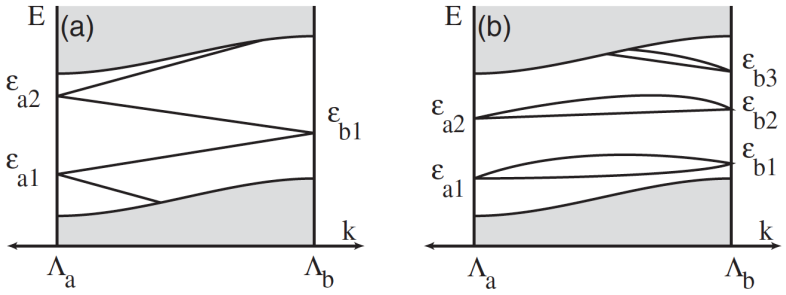

Figure 1.9: Schematic surface (or edge) state spectra as a function of momentum along a line connecting Λ_a to Λ_b. In (a) the Kramers pairs in the QSH phase cross the bulk energy gap an odd number of times. In the insulating phase (b), if the edge states cross the gap it happens an even number of times. They are not topologically protected [22].

Fu, Kane and Mele [22] have shown that in weak topological insulators, the bands cross the Fermi surface an even number of times while for strong topological insulators the crossing happens an odd number of time. Strong topological insulators cross the Fermi surface at the Γ-point (k=0).
Surface states of strong topological insulators have a π-Berry phase which is unusual for surface states of other materials than topological insulators. This π-Berry phase origins from a Dirac-like crossing at the centre of the Brillouin zone.
The surface states are protected by time-reversal symmetry and their topological invariant is given by the Kramer's degeneracy.

1.4 Thin films of topological insulators

One very important research field is to study the transport and optical properties of the metallic surface states of topological insulators. These surface states lie in the bulk energy gap of thin topological insulators.In thin topological insulator films tunnelling between top and bottom surface opens a finite gap in the Dirac cone at $\Gamma = 0$. This gap is a result of a spatial overlap of the wave functions of the top and bottom surface states when the thickness is comparable with the decay length of the surface states in the bulk.

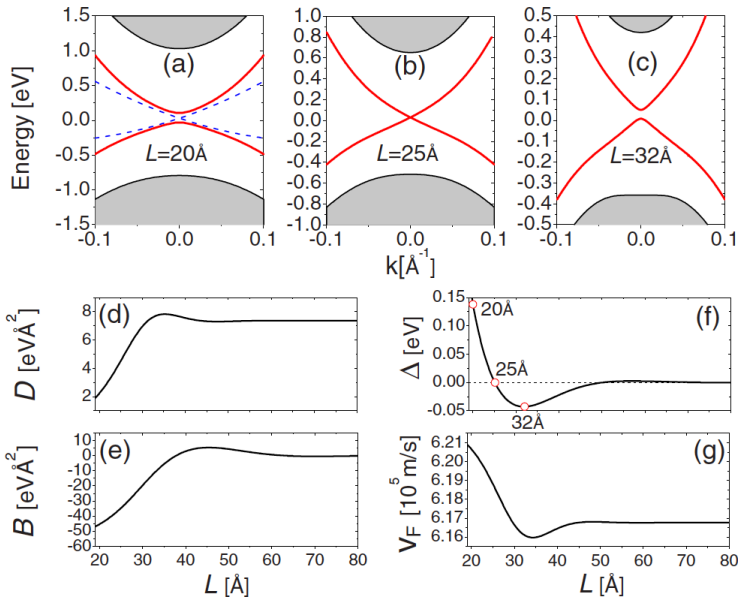

Figure 1.10: (a)-(c):Energy spectra of surface states as a function of momentum for length 2, 2.5 and 3.2 nm. It is two-fold degenerate and the bulk is represented by the grey area. Boundary conditions are given by $\Psi(x = \pm L/2) = 0$. (d)-(g): The different parameters of the bulk Hamiltonian and the Fermi velocity v_F as functions of the width of the TI. In (e) the mass parameter Δ reaches a minimum at 3.2nm where the gap is the largest [23].

The surface states of an ultra-thin film emerge in the entire film but always lie in the bulk energy gap.
Describing it would result in the ultra-thin film behaving like two degenerate, massive Dirac hyperbolas which form a time-reversal copy of each other. Each band has a k-dependent spin configuration: one near the Γ point and the other at k, determined by the spin-orbit coupling term.
Lu *e*t al.[23] studied the behaviour of the band gap depending on the thickness of the thin film in a range of length from 0 to 8 nm. They showed that the energy gap oscillates with the thin-film thickness, and changes sign at critical thickness (Fig. 1.10). Across the transition points, the k-dependent spin configuration flips near the Γ point while it stays unchanged for large k, which leads to a topological quantum phase transition where the Chern numbers of the surface bands change.

Looking at the two massive Dirac hyperbolas Lu et al. find that their opposite k-dependent spin configurations result in opposite physical properties including Berry curvature and orbital magnetic moments which makes manipulations of spin dynamics by electric and magnetic fields possible in thin films.
An in-plane electric field gives rise to the Hall effect. The electrons acquire a transverse velocity proportional to the Berry curvature. The Berry curvature is opposite in the valence band and conduction band. Both Dirac hyperbolas have opposite distributions of the Berry curvature. As a result the in-plane electric field can drive the spin up and spin down electrons towards the opposite transverse edges. The result is a net spin accumulation on the thin-film edges which is the surface spin Hall effect. For an ultra-thin film, which is described by a two-dimensional Hamiltonian, the Hall conductance is zero for $M > 0$ and $\sigma = n(e^2/h)$ for $M < 0$. When going from zero Hall conductance to finite Hall conductance gapless helical edge states appear in the system accompanying the transition. Another observation for small thickness is that the parameter B is smaller than zero and while the thickness of the thin film increases the parameter M changes sign which leads to a closing and re-opening of the band gap at critical thickness as seen in Figure 1.10.
The low-energy effective Hamiltonian for thin films can be described as follows:

$$H_{eff} = \begin{pmatrix} h_+(\mathbf{k}) & 0 \\ 0 & h_-(\mathbf{k}) \end{pmatrix}. \tag{1.12}$$

in which

$$h_{\tau_z} = E_0 - D\mathbf{k}^2 - \hbar v_F(k_x\sigma_y - k_y\sigma_x) + \tau_z\left(\frac{\Delta}{2} - B\mathbf{k}^2\right)\sigma_z, \tag{1.13}$$

and $\tau_z = \pm 1$ is the hyperbola index.

1.5 Magnetic impurities

Topological insulators are very interesting materials for studying the physics of robust Dirac points. The properties of Dirac points can be revealed by introducing a perturbation that breaks time-reversal symmetry and opens a gap on the surface of the topological insulator. Such perturbation can be realised by adding magnetic impurities on the surface of the TI.

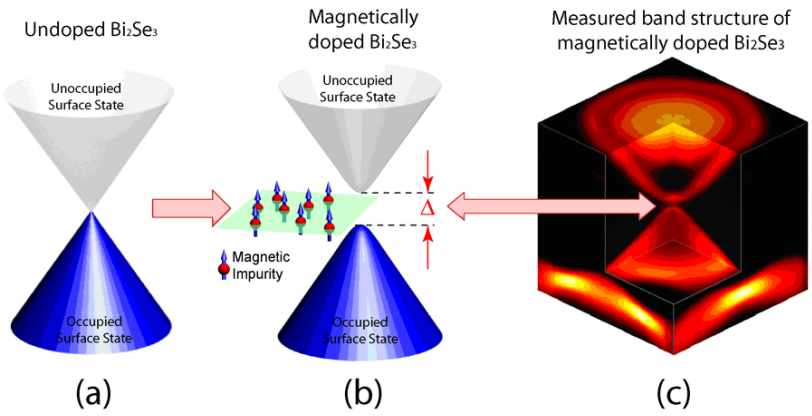

Figure 1.11: (a) Massless Dirac Fermion for unroped Bi_2Se_3. The surface states are separated into occupied and unoccupied. (b) Magnetic impurities open a gap by breaking TR symmetry, making the Dirac fermion massive. (c) Measurement of the electronic band structure for magnetically doped Bi_2Se_3. The arrow points at the band gap [25].

A topological insulator like Sb_2Te_3 can be doped with Vanadium as magnetic impurities.
In the paper of Liu *et* al. [24] they calculate the effect of magnetic impurities on the low-energy local density of states (LDOS) of a system with one single Dirac point. They show that the low-energy LDOS changes when magnetic impurities interact with the Dirac electrons on the surface and open a band gap which can be observed in STM experiments.
Furthermore they show that the effect of the magnetic impurities on the LDOS changes depending on the direction of the magnetisation. They find that the system can be described as an electron spin coupled to a momentum-dependent effective magnetic field. We will discuss the different behaviour related to the orientation of the magnetic field in the Appendix.
When the distribution of the magnetic impurities on the surface is random every magnetic impurity will open a local band gap in its vicinity. In the mean-field level they system is not gapped everywhere. Liu *et* al. [24] find that for a non-uniform magnetisation gapless chiral fermion modes appear along the domain wall. These modes cost the system more energy and they expect the magnetic impurities to couple ferromagnetically instead of gapless modes.
The coupling between two magnetic impurities can be described as me-

diated by an electron which is nothing else but the Ruderman-Kittel-Kasuya-Yosida (RKKY) interaction.
When the chemical potential is near the Dirac point two magnetic impurities become ferromagnetically coupled when λ_f (the Fermi wavelength) is much larger than the average distance between them. Therefore it is expected that the magnetic impurities couple ferromagnetically when the chemical potential lies near the Dirac point.
Such an ferromagnetically ordered surface state carries a half-quantized Hall conductance which is an indication of the non-trivial topology of the system, as discussed above.

1.6 Topological insulators as an important research field

Being a new state of matter, insulator in the bulk with metallic surface states on the edges, topological insulators have been an interesting research field already. Besides being new, many novel effects have been experimentally realised in the field of topological insulators.
The first effect related to TIs was the QHE which led to the discovery of the first TIs in two and three dimensions. After the QSH effect has been realised the latest experimental success has been the observation of the anomalous QHE (AQHE) [26] in magnetic TIs.
The AQHE arises from SOC, when spontaneous magnetic moments and SOC combine. They give rise to the QHE without an external magnetic field [27]. The first theoretical prediction was made by Yu et al.[27] in 2010 and the experimental realisation followed in 2013 by Chang *e*t al.[26] Chang *e*t al. reported the observation of the AQHE in thin films of Cr-doped (Bi,SB)$_2$Te$_3$. They predicted that the observation of the AQHE may lead to low-power-consumption electronics.
Besides the different Hall effects, TIs are a new state of matter which could host more exotic quantum matter like Majorana Fermions, Axions and magnetic monopoles.
Qi *e*t al. [28] released a paper on the possibility of observing magnetic monopoles in topological insulators while conserving Maxwell's law $div\mathbf{B} = 0$. The idea is to add an extra term to the Maxwell equation which is zero for weak, and $(n+1)\frac{1}{4\pi}\alpha\mathbf{BE}$ with $\alpha = e^2/\hbar c$, **B** the magnetic field, **E** the electric field, n integer, e the electron charge, $\hbar$=$h/2\pi$ with h the Planck constant and c the speed of light, for strong topological insulators. This extra term describes the magneto-electric effect where a magnetic

field induces a polarisation and an electric field induces a magnetisation. Putting an electric charge on top of a topological insulator would induce a magnetic monopole inside and outside the TI. As those monopoles cancel each other in total $div\mathbf{B} = 0$ is conserved. The monopole inside the TI causes a phase shift which can be measured experimentally.
The same term added to the Maxwell equation leads to the Axion in topological insulators.
Li *e*t al.[29] showed that magnetic fluctuations of topological insulators couple to the electromagnetic fields exactly like the axions in particle physics, and proposed several experiments to detect this dynamical axion field.
The dynamic axion field θ couples nonlinearly to the external electromagnetic field combination **EB**. When there is an externally applied static and uniform magnetic field B_0 parallel to the electric field **E** of the photon, it will couple linearly to **E**. In condensed-matter systems, when a collective mode is coupled linearly to photons, hybridized propagating modes called polaritons emerge. The polaritons can be coupled modes of optical phonons and light through the electric dipole interaction, or coupled modes of magnons and light through the magnetic dipole interaction.
They proposed a new type of polariton the axionic polariton, which is the coupled mode of light and the axionic mode of an antiferromagnet.
In condensed matter physics, Majorana fermions exist as quasiparticle excitations in superconductors and can be used to form Majorana bound states possessing non-abelian statistics.
In 2008 Fu and Kane[30] studied the proximity effect between an s-wave superconductor and the surface states of a strong topological insulator. The resulting state supported Majorana bound states at vortices. Fu and Kane showed that the linear junctions between superconductors mediated by the topological insulator form a nonchiral one-dimensional wire for Majorana fermions, and that circuits formed from these junctions provided a method for creating, manipulating, and fusing Majorana bound states.

1.7 Applications of Topological Insulators

After understanding the physics of topological insulators and the importance of this research field it is crucial to motivate interest in creating applications using TIs. In three dimensions several materials like Bi_2Se_3, Bi_2Te_3, $Bi_{1-x}Sb_x$, Sb_2Te_3 have been found to be topological insulators, so that there is no lack of candidate materials for new applications.

Each of these materials have edge state channels where the carriers go dissipationsless from A to B. This loss-free transport rises hopes for the creation of low-power electronics.
Besides dissipationless transport, we talked in previous chapters about the manipulation of the electron spin in TIs. Thin films of TIs are candidates for electronic and spintronic devices.
Another possible future for TIs, is in heterostructure with superconducting (SC) materials to improve their performance. This may create fast SC chips.
The existence of Majorana zero modes in TIs may find application in fault-tolerant quantum computing.
The field of topological insulators has been studied intensively over the last decade with many new findings made. The latest experiments have shown it's importance in confirming effects like the AQHE and the future of topological insulator applications may go even beyond that when it comes to it's importance.

1.8 Outline

This thesis is organized as follows: In the main part of the thesis I will present the publications and projects I have been doing on topological insulators and related topics in the last four years. First I will introduce our results on the magnetically doped topological insulator Bi_2Se_3. Our results show that depending on temperature the order of the magnetic impurities changes. At zero temperature the order is ferromagnetic but when the temperature rises the system undergoes two transitions. A first-order transition from the ferromagnetic phase to a spin-density wave phase and later at higher temperature a second-order transition into the paramagnetic phase.We find that the origin of this phase is the nontrivial dependence of the spin susceptibility on the momentum. We further analyse the coupling of the nonuniform magnetic phase with the Dirac electronic system that occurs at the surfaces of the topological insulator.
In the project I did during my stay at Nordita in Stockholm we worked on the isotropic magneto-electric effect that has been studied in topological insulators and applied a similar idea to multiferroic materials. The main aim is to measure the local monopole field induced by the charge outside the material of an interface multiferroic-vacuum. The existence of this local magnetic field would proof that an electric charge could induce a magnetic monopole in a system where the magneto-electric ef-

fect is present. This has been shown theoretically in topological insulators but we believe is also possible in multiferroics. We study the dynamic magneto-electric effect and the collective excitations in the magnetic structure called electromagnons. Therefore we calculated the magnetisation and polarisation of the system as functions of time and studied the behaviour of the frequency.
In our second publication on TIs we study the optical properties of ultra-thin topological insulator slabs for which the coupling between Dirac fermions on opposite surfaces results in two degenerated gapped hyperbolic bands. An exchange field applied perpendicular to the slab splits the degenerated hyperbolic bands and a double step structure comes out in the optical absorption, whereas a double peak structure appears in the imaginary part of the longitudinal optical conductivity. The exchange field breaks time-reversal symmetry and for exchange fields larger than the surfaces coupling gap, the zero frequency Hall conductivity is quantized to e^2/h. This result implies large values of the Kerr and Faraday rotation angles. In ultra-thin slabs, the absence of light multiple scattering and bulk conductivity, makes the Kerr and Faradays angles to remain rather large in a wide range of frequencies.

Part I

CHAPTER 2

Magnetically doped topological insulator Bi_2Se_3 at finite temperatures

Adapted from:
M. Lasia and L. Brey
"Temperature-induced spin density wave in a magnetically doped topological insulator Bi_2Se_3",
Phys. Rev. B **86**, 045317 (2012).

We study the magnetic properties of Bi_2Se_3 doped with isoelectronic magnetic impurities. We obtain that at zero temperature the impurities order ferromagnetically, but when raising the temperature the system undergoes a first-order phase transition to a spin density wave phase before the system reaches the paramagnetic phase. The origin of this phase is the nontrivial dependence of the spin susceptibility on the momentum. We analyse the coupling of the nonuniform magnetic phase with the Dirac electronic system that occurs at the surfaces of the topological insulator.

2.1 Introduction

Topological insulators (TIs) are a newly discovered type of systems which are insulating in the bulk and characterised by the existence of a robust

helical gapless Dirac two-dimensional electron system at their surface [1, 10, 31].

TIs are typically band insulators for which strong spin-orbit coupling produces an inversion of the bulk band gap. Therefore, in TIs the energy gap is related to the spin-orbit coupling and that limits its magnitude. The most studied and more promising topological insulator is Bi_2Se_3, which is a three-dimensional TI with relatively large bulk energy gap of 0.3eV and with the Dirac point of the surface located outside the bulk bands [18, 19]. Angle resolved spectroscopy [18, 32] and scanning tunnelling microscopy [33] experiments have shown the Dirac nature of the surface states of Bi_2Se_3 .

The spin and wave vector of the surface states of a TI are strongly coupled, and the occurrence of a half-quantised Hall effect when an energy gap opens at the surface has been predicted [34, 35]. Due to the protected character of the Dirac states, a gap at the surface should be opened with a perturbation that breaks time-reversal symmetry. This can be done by doping the system with magnetic impurities. At the surface of the TI, because of the large spin-orbit coupling, the interaction between the Dirac-like surface states and the impurities induces a large single ion magnetic anisotropy and polarises the spin of the impurities perpendicular to the surface. This spin-orbit coupling translates in the opening of an energy gap at the Dirac point of the surface states [24],[36]-[44].

From the experimental side, angle resolved photoemission spectroscopy (APRES) studies on the surface of Fe-doped Bi_2Se_3 single crystals have confirmed the opening of an energy gap at the Dirac point [45] and the creation of odd multiples of Dirac fermions [46]. Also recently, experiments in thin films of Cr-doped $Bi_xSb_{2-x}Te_3$ have shown a large anomalous Hall conductance in a magnetically doped topological insulator [47]. However, recent experiments [48] found that the spins of Fe ions deposited on Bi_2Se_3 orient in-plane. Also APRES experiments [49] and [50] found Dirac crossing even in the presence of magnetic impurities on contradiction with earlier experiments and existing theory. On the other hand, recently the suppression of the Dirac point spectral weight, both in magnetically doped and un-doped TI, suggesting that the observed gap at the Dirac point cannot be taken as the sole evidence of a magnetic gap [51]. In addition, density functional theory based calculations [52] fond that Co adaptors lying in the Bi_2Se_3 , surface exhibit an energetically stable magnetic moment perpendicular to the surface, whereas for Co atoms located on the interlayer van der Waals spacing the momentum is in the plane parallel to the surface. All these results indicate the complexity of the interpretation of the APRES experiments and the pos-

sible importance of other effects not included in the Dirac Hamiltonian, as crystalline anisotropy or surface reconstruction might play an important role on the orientation of the magnetic impurities.
In this work we use an effective Hamiltonian for describing Bi_2Se_3, which although it does not include microscopic details of the material, describes appropriately the basic properties of the Bi_2Se_3 related to its band structure topology.
In this work we study the phase diagram of magnetically doped Bi_2Se_3. Bi_2Se_3 is a layered material formed by five atom layers arranged along the z direction. We find that at low temperatures the magnetic impurities order ferromagnetically along the z direction. By raising the temperature, the TI undergoes two transitions. A first-order transition from the ferromagnetic to the spin-density wave phase and at higher temperatures a send-order transition from the spin density wave phase to the paramagnetic phase. The spin density wave phase has both the polarisation and the wave vector parallel to the z direction. We have also studied the effect of the surface states by calculating the magnetisation as a function of temperature of a slab of Bi_2Se_3 topological insulator. Here we find that the surface magnetisation survives to higher temperatures than the bulk spin density wave phase.

2.2 Hamiltonian

The low energy and long wavelength properties of Bi_2Se_3 topological insulators are described by the four bands $k.p$ hamiltonian [19] as seen in the introduction.

$$H = E(\mathbf{k}) + \mathcal{M}(\mathbf{k})\tau_z I + A_1 k_z \tau_x \sigma_z + A_2(k_x\tau_x + k_y\tau_y)\sigma_x. \qquad (2.1)$$

The hamiltonian contains the functions $\mathcal{M}(\mathbf{k})$=$M_0 - B_2(k_x^2 + k_y^2) - B_1 k_z^2$, $k_\pm$=$k_x \pm ik_y$ and $E(\mathbf{k})$=$C + D_1 k_z^2 + D_2(k_x^2 + k_y^2)$. The Hamiltonian is written in the basis$|1\rangle$=$|p1_z^+, \uparrow\rangle$, $|2\rangle$=$-i|p2_z^-, \uparrow\rangle$,$|3\rangle$=$|p1_z^+, \downarrow\rangle$, $4\rangle$= $i|p2_z^-, \downarrow\rangle$, which are the hybridized states of the Se p orbital and the Bi p orbital with even $(+)$ and odd $(-)$ parities and spin up ($\uparrow$) and down ($\downarrow$). The Hamiltonian parameters for Bi_2Se_3 [53] are, M_0=0.28eV, A_1=2.2$eV\,\AA$, A_2=4.1$eV\,\AA$, B_1=10$eV\,\AA^2$, B_2=56.6$eV\,\AA^2$, C=-0.0068eV, D_1=1.3$eV\,\AA^2$ and D_2=19.6$eV\,\AA^2$. In this basis the spin operators get the form [54] S_z=$I \times \sigma_z$, S_x=$\tau_z \times \sigma_x$, and S_y=$\tau_z \times \sigma_y$.

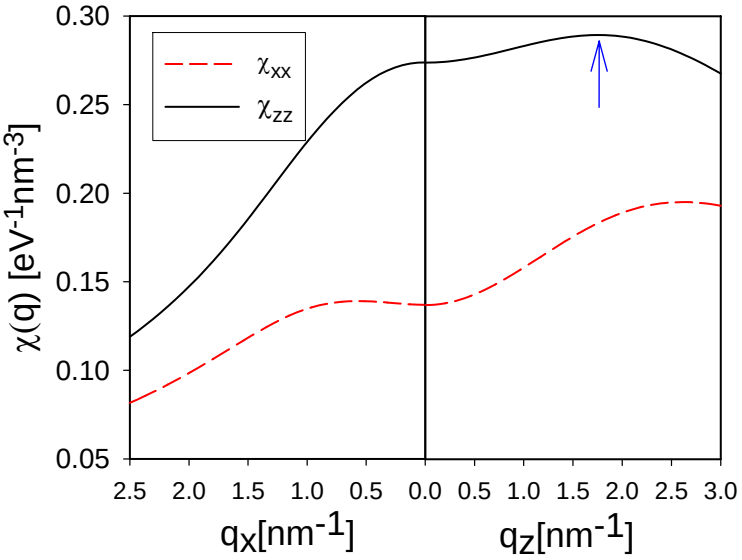

Figure 2.1: Spin susceptibility as function of the wave vector along the z and the x directions/ The arrow indicates the position of the maximum.

2.3 Bulk spin susceptibility

The paramagnetic susceptibility obtained from the Hamiltonian Eq.(2.1) has the form

$$\chi_{\mu\mu}(\mathbf{q}) = \frac{2}{\Omega} \sum_{n' occ. n empty} \sum_{\mathbf{k}} \frac{|\langle n', \mathbf{k}+\mathbf{q}|S_\mu|n, k\rangle|^2}{\epsilon_{n',\mathbf{k}+\mathbf{q}} - \epsilon_{n,\mathbf{k}}}. \tag{2.2}$$

Here $|n, \mathbf{k}\rangle$ and $\epsilon_{n,\mathbf{k}}$ are the eigenfunctions and eigenvalues of Hamiltonian Eq.(2.1) and Ω is the sample volume. In the case of an insulator, this spin susceptibility is caused by the coupling of the valence band and the conduction band induced by the spin operator [55]. The susceptibility is a smooth function of the wave vector and because the system is an insulator there are no anomalies associated with Fermi surfaces. The symmetry of the original Hamiltonian dictates that the non diagonal elements of the susceptibility tensor are zero and $\chi_{xx} = \chi_{yy} \neq \chi_{zz}$.
In Fig 2.1 we plot the χ_{xx} and χ_{zz} as a function of q_z andq_x. The direct coupling $A_2 k_\pm$, between atomic orbitals with opposite parities and opposite z component of the spin, makes that for $k_\pm \neq 0$, occupied and empty

states are coupled through S_z. Whereas those states are only connected through S_x when $k_z \neq 0$. This makes $\chi_{xx} > \chi_{zz}$.
The more important contribution to $\chi_{zz}(\mathbf{q})$ comes from regions in the reciprocal space where the matrix elements $|\langle n', \mathbf{k}+\mathbf{q}|S_\mu|n, k\rangle|$, with n occupied and n' empty, reaches the maximum value. This happens when $\mathcal{M}(\mathbf{k}) = 0$ or $\mathcal{M}(\mathbf{k}+q_z) = 0$. For a given k_z these conditions define two circular crowns of radius $\sqrt{\frac{M_0 - B_1 k_z^2}{B_2}}$ and $\sqrt{\frac{M_0 - B_1(k_z+q_z)^2}{B_2}}$ and thickness $A_2/(2B_2)$. Therefore, the area of the reciprocal space that contributes appreciably to $\chi_{zz}(\mathbf{q})$ increases with q_z. For larger values of q_z one of the circular crowns collapses to zero and the contributions to the integral decrease. This behaviour explains qualitatively the maximum that χ_{zz} presents at a wave vector $G \sim \sqrt{M_0/B_1}$.
The existence of a maximum in $\chi_{zz}(q_z)$at finite q_z is robust against small changes in the parameters of the four bands Hamiltonian. In Fig. 2.2 we plot $\chi_{zz}(q_z)$ for different values of the TI gap. The position of the maximum decreases continuously towards $\mathbf{q} = 0$ when M_0 decreases and only disappears for small values of M_0. In the normal insulator phase $M_0 < 0$, the maximum always occurs at $\mathbf{q} = 0$.

Coupling between diluted magnetic impurities

Consider now a TI doped with magnetic impurities of spin S. We assume that the number of electrons in the system does not change in the presence of the magnetic impurities. That can be achieved by doping with isoelectronic magnetic dopants [56] or by adding compensating nonmagnetic dopants. In this work we consider the dilute limit, that is, concentration of impurities smaller than 5%, for which the direct and indirect interaction between the spin of the magnetic impurities can be neglected. However the electrons spins have a strong exchange coupling $\frac{S}{2}J(|r|)$with the magnetic impurities spins, which, in turn, are equally affected by the exchange field of the electrons. In this form the magnetic impurities in the system interact mediated by electronic states. We treat this interaction in second-order perturbation theory [57, 58] that has proved to be a reliable approximation in diluted magnetic semiconductors [58, 59].
In this approach the effective exchange parameter between two magnetic impurities separated by a vector $\mathbf{R}$ and spins pointing in the ν direction is

$$J_\nu(\mathbf{R}) = -\frac{S^2}{4} J_{eff}^2 \Omega \sum_{\mathbf{q}} \chi_{\nu\nu}(\mathbf{q}) e^{i\mathbf{q}\mathbf{R}}, \tag{2.3}$$

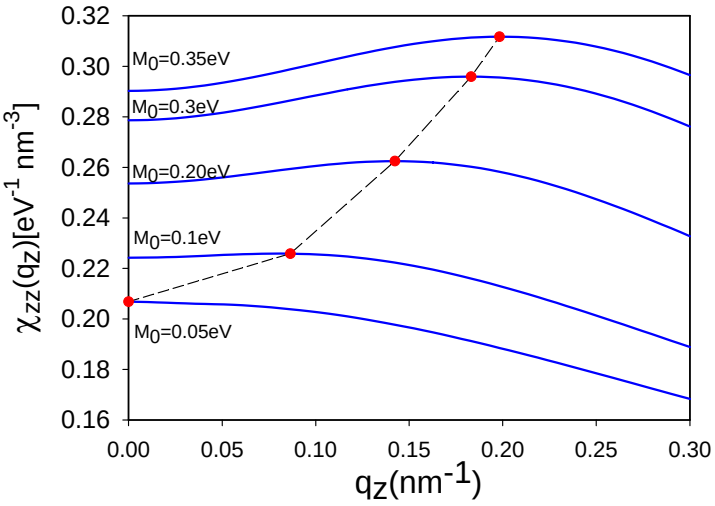

Figure 2.2: Spin magnetic susceptibility χ_{zz} for different values of M_0 as a function of the momentum in the z direction. All other parameters of the band structure correspond to those of Bi_2Se_3. As the values of the mass M_0 decreases the position of the maximum of the susceptibility moves towards small values of q_z. At small values of M_0 the maximum occurs at $q_z = 0$. In the normal insulator phase $M_0 < 0$, the maximum of χ_{zz} occurs at $q_z = 0$ for all values of the mass parameter. The dots indicate the position of the maximum.

where $J_{eff} = \int J(|\mathbf{r}|)d\mathbf{r}$ is the effective exchange coupling between the magnetic impurity and the electron spin.
Because $\chi_{xx} > \chi_{zz}$ in all range of wave vectors, the system has an easy axis of magnetisation along the z direction and therefore isoelectronic magnetic impurities in Bi_2Se_3 will tend to polarise in the z direction. The maximum that the spin susceptibility presents at finite wave vector in the z direction will determine the existence of nonuniform polarisation in the magnetically doped TI. We treat the magnetically ordered state in the virtual crystal approximation [58, 59, 60, 61], and we consider that the system is invariant in the (x, y) plane, and the polarisation only depends on the z direction.

2.4 Landau free energy functional

We assume that the system is invariant in the (x, y) plane, and allow the polarisation to oscillate with period $2\pi/G$ along the z direction. In consequence we define the normalised magnetic polarisation $-1 \leq m(z,T) \leq 1$ as

$$m(z,T) = m_0(T) + m_G(T)cos(Gz) \tag{2.4}$$

where m_0 and m_G are the order parameters of the uniform ferromagnetic (FM) phase and the spin density wave phase (SDW), respectively.
The internal energy per unit volume corresponding to this magnetisation is

$$E = -\frac{J}{2}m_0^2\chi_{zz}(0) - \frac{J}{4}m_G^2\chi_{zz}(G) \tag{2.5}$$

where $J = \frac{S^2}{4}J_{eff}^2 c$, c being the density of magnetic impurities. In our case, the value of $\chi_{zz}(G)$ is less than 10% larger than $\chi_{zz}(0)$ and the zero temperature ground state is a uniform FM phase, $m(z, T = 0) = 1$. However the maximum if the spin susceptibility at G will modify the spin density at larger temperatures.
Knowing that for small values of the polarisation the entropy of a classical spin at given T is

$$-TS = -k_BTln(2) + \frac{3}{2}k_BTm^2 + \frac{9}{20}k_BTm^4. \tag{2.6}$$

We get that in the mean-field approximation and for small values of the magnetic polarisation the Landau free energy per unit volume takes the form

$$F = -\tfrac{J}{2}m_0^2\chi_{zz}(0) - \tfrac{J}{4}m_G^2\chi_{zz}(G) - \tfrac{1}{\beta}\tfrac{1}{L}\int dz\left[ln2 - \tfrac{3}{2}k_BTm^2 - \tfrac{9}{20}k_BTm^4...\right], \tag{2.7}$$

where $\beta = 1/k_BT$ and L is the sample dimension in the z direction. Using expression (2.4), and in the limit of $L \to \infty$, we get

$$F = \tfrac{3}{2}m_0^2k_B(T - T_0) + \tfrac{3}{4}m_G^2k_B(T - T_G) + k_BT\tfrac{27}{20}m_0^2m_G^2 + k_BT\tfrac{9}{20}m_0^4 + k_BT\tfrac{27}{160}m_G^4, \tag{2.8}$$

where T_0 and T_G are the critical temperature of the pure FM and SDW phases, respectively,

$$k_BT_0 = \frac{J}{3}\chi_{zz}(0), \tag{2.9}$$

and

$$k_BT_G = \frac{J}{3}\chi_{zz}(G). \tag{2.10}$$

The phase diagram of a system described by a free energy as that of Eq.(2.8) depends on the relative magnitudes of the fourth order potentials [62]. In our case the product of the pre factors of m_0^4 and m_G^4 is smaller than the square of the $m_0^2 m_G^2$ pre factor and there is no phase coexistence in the phase diagram. By increasing the temperature, there is a first order transition from the FM phase to the SDW phase at

$$T* = \frac{\sqrt{3}T_0 - \sqrt{2}T_G}{\sqrt{3} - \sqrt{2}}. \tag{2.11}$$

This is the main result of this paper: By heating, a magnetically doped TI undergoes two phase transitions, a FM to SDW first-order transition at $T*$ and a SDW to paramagnetic second-order transition at T_G. Although at $T = 0$ the FM phase has lower energy than the SDW phase, the FM to SDW transition at finite T occurs because the entropy of the SDW increases faster with T than the entropy of the FM phase.

Mean-field expression for the entropy

We calculate an expression for the entropy of a system of classical spins of magnetisation m that are coupled with the topological insulator through a general term $E[m]$.
The free energy of a system of classical spins of magnitude unity in an external magnetic field h is

$$F = -\frac{1}{\beta} ln \left[2 \frac{sinh(\beta h}{\beta h} \right] \tag{2.12}$$

from where the magnetisation can be calculated as

$$m \equiv \langle m \rangle = -\frac{\partial F}{\partial h} = \frac{1}{tanh(\beta h)} - \frac{1}{\beta h} \tag{2.13}$$

The entropy of the spin system is then

$$-TS = F - mh = -\frac{1}{\beta} \{ ln \left[2 \frac{sinh(\beta h}{\beta h} \right] + m\beta h \} \tag{2.14}$$

The total energy of the system is

$$F^{total} = E[m] - TS = E[m] - \frac{1}{\beta} \{ ln \left[2 \frac{sinh(\beta h}{\beta h} \right] + m\beta h \} \tag{2.15}$$

where $E[m]$ is the change in the electronic energy of the system because of the polarisation of the magnetic impurities. To obtain h we minimise the total free energy with respect to h, $\partial F^{total}/\partial h = 0$. In the limit of small h,

$$n\left[2\frac{sinh(\beta h}{\beta h}\right] \simeq ln(2) + \frac{(\beta h)^2}{6} - \frac{(\beta h)^4}{180} + ... \tag{2.16}$$

In this limit the minimisation condition gives $\beta h = -3m - \frac{3}{5}m^3 + ...$, and the entropy gets the form

$$-TS = -k_B T n(2) + \frac{3}{2}k_B T m^2 + \frac{9}{20}k_B T m^4. \tag{2.17}$$

2.5 Spin polarisation of magnetically doped TI slabs

At the surface of a TI there exist a two-dimensional Dirac electron gas. Because of the chirality of the electron gas, an exchange field perpendicular to the surface opens a gap in the spectra. Then, in order to minimise the energy, a magnetic impurity will polarise perpendicular to the surface. In the diluted limit, surface states mediate a Ruderman-Kittel-Kasuya-Yosida (RKKY) interaction among the impurities which is always ferromagnetic, whenever the chemical potential resides near the Dirac point. [24, 37, 43, 63]
Therefore magnetic impurities at the surface of a TI will order ferromagnetic ally perpendicular to the surface.
We are going to study numerically the spin polarisation as a function of temperature and position of a magnetically doped TI slab. The objective here is to first confirm the results we obtained with the Landau free energy functional where we consider a unique Fourier component of $\chi_{zz}(q_z)$ and second to analyse the coupling between the surface and the bulk magnetisation.
We analyse a TI slab of thickness L perpendicular to the z direction. We expect the electron affinity of Bi_2Se_3 to be much larger than the band gap. Therefore, at the surface of the TI we will neglect the penetration of the electron wave function into the vacuum. The eigenvalues $\epsilon_{n,\mathbf{k}}$ and wave functions $\Psi_{n,\mathbf{k}}(z)$ are obtained by solving Eq.(2.1) with $k_z = -i\partial_z$ and forcing the wave function to vanish at $z = 0$ and $z = L$. This is satisfied expanding $\Psi_{n,\mathbf{k}}$ in harmonics,

$$\Psi_{n,k} = \frac{e^{i\mathbf{kr}}}{\sqrt{a}}\sqrt{\frac{2}{L}}\sum_{l=1}^{N_{max}}\sum_{j=1,4} a^l_{n,j}(\mathbf{k})sin\left(\frac{l}{L}\pi z\right), \tag{2.18}$$

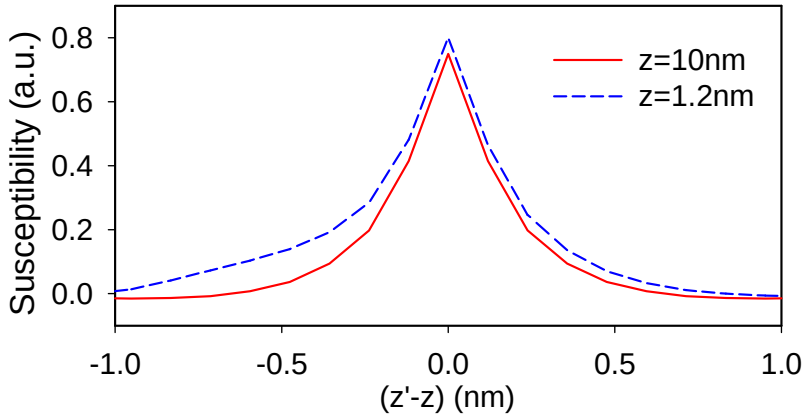

Figure 2.3: $\chi(z, z')$ evaluated at the maximum of the surface wave function, z =1.2nm, and at the centre of a 20nm thick slab, as a function of z'. The first case corresponds to a region near the surface, where the two-dimensional Dirac electron system contributes to the response functions. In the latter case the response function is not affected by the surface and it is the bulk response function. In both cases the functions are very peaked at $z = z'$. The negative values of the coupling in the bulk response function is a consequence of the maximum that the response function presents at $q_z = G$ in the reciprocal space. Near the surfaces, and because of their metallic character, the magnetic coupling is stronger. This is reflected in the asymmetry of the dashed line, the interaction between planes is larger the closer the planes are to the surface.

here A is the sample area and we choose N_{max} large enough so that the results do not depend on it.
For $L > 10nm$ the surfaces of the slab are decoupled and the band structure is independent of L. In the bulk energy gap region, some surface states appear which are the benchmark of the TI. In Fig. (2.3) we plot the band dispersion and the shape of the wave function of these states. The results we obtain agree completely with previous results [31, 54].
In the slab geometry the momentum in the z direction is not a good quantum number and the paramagnetic susceptibility depends on two position indices z and z'. Therefore, in the virtual crystal approximation and in second-order perturbation theory, the internal energy of the magnetically doped TI slab is

$$E = \frac{J}{2L} \int_0^L \int_0^L dz dz' \chi(z, z') m(z) m(z'), \tag{2.19}$$

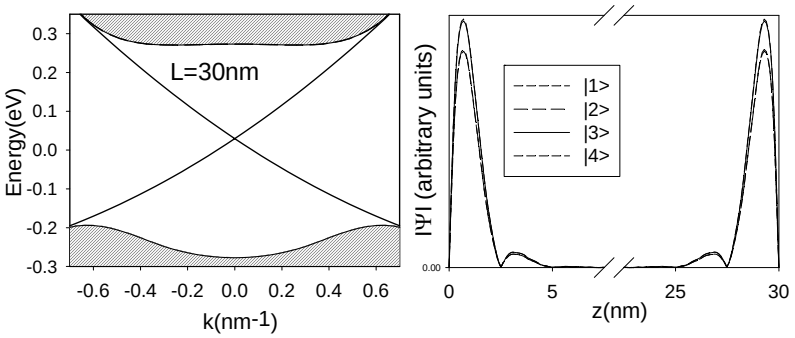

Figure 2.4: This figure shows the band structure of a topological insulator film 30nm thick. For this thickness there is no coupling between localised states on opposite surfaces and surface states are degenerated. Dashed areas denote the bulk band structure. In the right panel we plot the absolute value of the four components of the wave function of a surface state with momentum close to zero.

with

$$\chi(z,z') = \frac{1}{A}\sum_{n,n',\mathbf{k}} \frac{n_F(\epsilon_{n,,\mathbf{k}}) - n_F(\epsilon_{n',,\mathbf{k}})}{\epsilon_{n',,\mathbf{k}} - \epsilon_{n,,\mathbf{k}}} \tag{2.20}$$

where $n_F(\epsilon)$ is the Fermi distribution function. $\chi(z,z')$ indicates the coupling between uniform polarised (x,y) planes, located at positions z and z'. The interaction between magnetic impurities is mediated by electrons in the system, and because the bulk system is an insulator, the interaction is very short ranged in the z direction see Fig. (2.4).
We compute the temperature dependence of the magnetisation profile in the mean-field approximation. At given position z, the magnetisation $m(z,T)$ feels a magnetic field,

$$B(z) = J\int_0^L dz'\chi(z,z')m(z'), \tag{2.21}$$

and the magnetisation of an isolated impurity in the presence of the molecular field is

$$m(z,T) = coth\left[\frac{B(z)}{k_BT}\right] - \frac{k_BT}{B}. \tag{2.22}$$

Solving self-consistently Eqs. (2.14) and (2.15), we obtain the magnetisa-

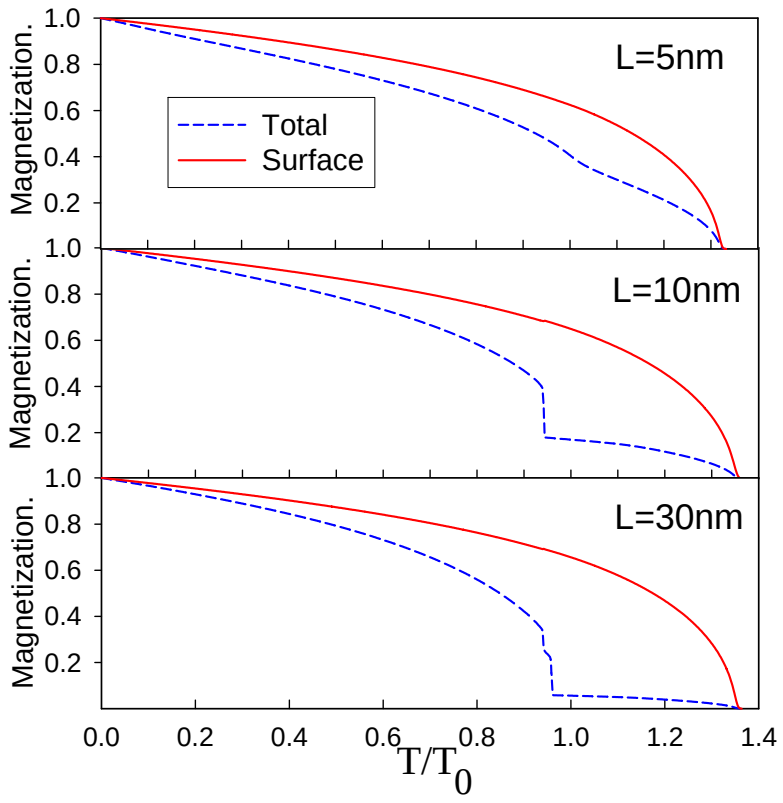

Figure 2.5: Magnetisation as a function of temperature for TI slabs of thickness (a) L = 5nm, (b) L = 10nm, and (c) L = 30nm. T_0 is the bulk FM critical temperature of the topological insuator. The small "step" in the middle of the first-order transition that occurs at L = 30nm is a consequence of an interference effect between the surface magnetisation and the bulk SDW phase.

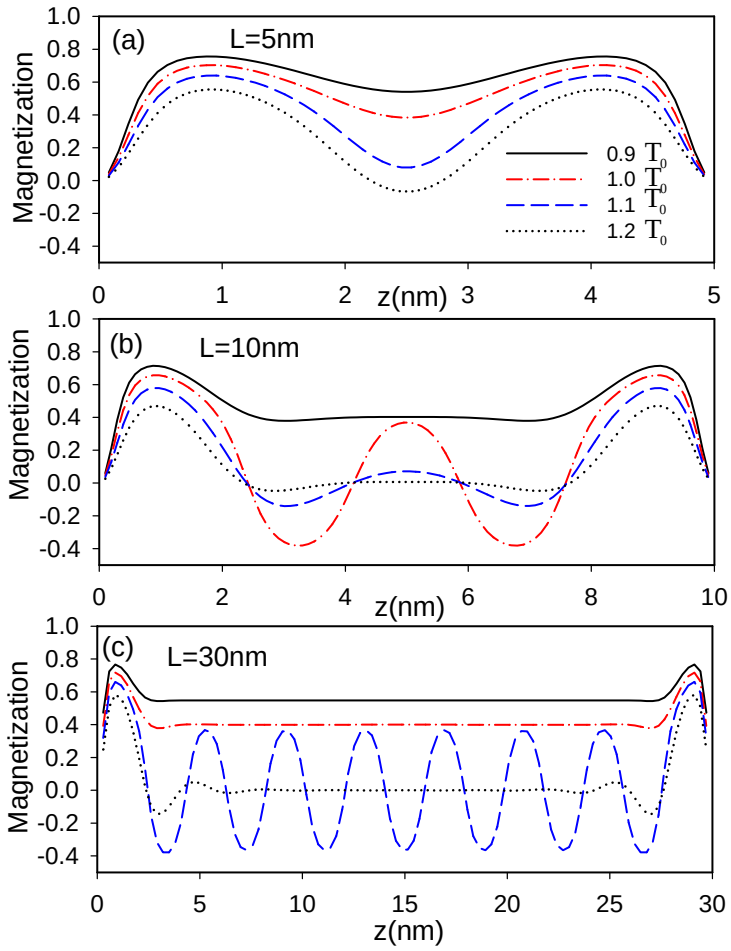

Figure 2.6: Magnetisation as a function of the position across the topological insulator slab z for different layer thickness and temperatures.

tion profiles as a function of T.
Because the metallic surface states intermediate a RKKY coupling [24, 63] at the surface, the response function $\chi(z, z')$ is larger near the surface than in the bulk, see Fig. 2.4. Therefore, as a function of T, the absolute value of the magnetisation decreases faster in the bulk region than in the surface. However, it is important to note that the surface and the bulk are part of a unique system and therefore there is only a unique critical temperature corresponding to the transition of the paramagnetic phase.
In Fig. 2.5 we show the magnetisation as a function of temperature for TI slabs of thickness $L = 5nm$, $= 10nm$ and $L = 30nm$. We plot the average value of $m(z, T)$, and the value of the magnetisation on top of the surface states. In Fig. 2.6 we plot the magnetisation profiles for different temperatures for $L = 5nm$, $L = 10nm$ and $L = 30nm$.
For $L = 10nm$ and $L = 30nm$ the surfaces are practically decoupled and the central part of the slab behaves as bulk. There is a strong jump in the magnetisation at T^* that indicates the first-order FM to SDW transition. In the SDW phase the oscillating magnetisation does not contribute to the total magnetisation and the magnetisation for $T > T^*$ is due to surface states. In Fig 2.6(b) and 2.6(c) the abrupt transition from a uniform magnetisation phase to a SDW phase is apparent at the centre of the slab. For smaller thickness of the slab Fig.6.a the surface states are coupled and there is no well-defined bulk region that reflects in the absence of FM to SDW transition.
The magnetisation at the surface is practically not affected by the FM to SDW transition, and decays with T continuously to zero. The ferromagnetism at the surface is more robust than in the central part. For temperatures where m_0 and m_G are near zero, the surface of the system can be more than 30% polarised. These results indicate the possibility that the magnetisation at the surfaces of Tis could be finite at temperatures larger than the bulk critical temperaturs T_G and T^* [64]. Because of the metallic character of the TI surface states, there is a range o temperatures for which the Dirac-like electron system at the surface of the TI is gapped, although the bulk part of the system is practically unpolarised.
A similar SDW phase has been also obtained numerically by Rosenberg and Franz in a slab geometry of Bi_2Se_3 [64]. However these authors interpret the oscillation of the polarisation as spatial fluctuations of the bulk magnetisation coupled with the surface magnetisation. From our calculation we attribute the oscillations in the magnetisation reported in [64] as a signature of the bulk SDW phase.

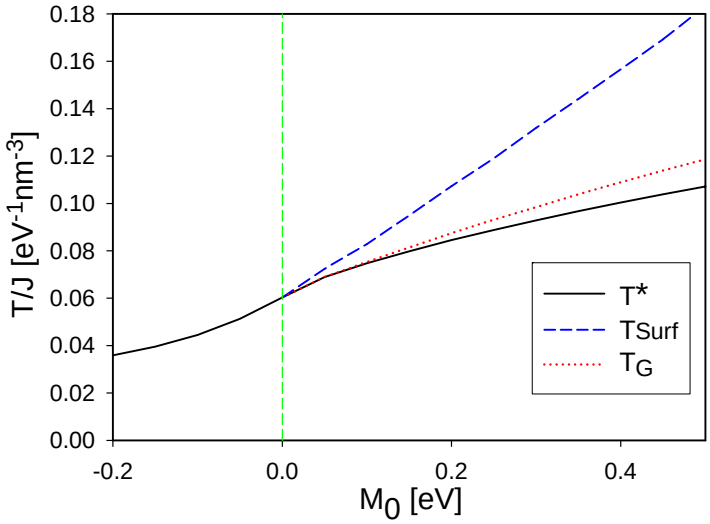

Figure 2.7: Phase diagram of a thick magnetic doped TI as a function of the mass parameter M_0.

2.6 Conclusions

In this publication we studied the phase diagram of magnetically doped Bi_2Se_3. At low temperatures the magnetic impurities order ferromagnetic ally along the z direction. By raising the temperature, the TI undergoes two transitions. A first-order transition from the ferromagnetic to the spin density wave phase and at higher temperatures a send-order transition from the spin density wave phase to the paramagnetic phase. This result could explain recent experimental results [65] that suggest the existence, as function of temperature, of two different magnetic phases in Fe doped Bi_2Se_3.
We have also studied the effect of the surface states by calculating the magnetisation as a function of temperature of a slab of Bi_2Se_3 topological insulator. Here we find that the surface magnetisation survives to higher temperatures than the bulk spin density wave phase. The existence of a range of temperatures for which the bulk magnetisation practically vanishes, whereas a finite magnetisation exists at the surface, could explain some experimental results that observe a gap at the surface of Bi_2Se_3 but no bulk magnetisation [45, 47].

It is important to analyse the behaviour of the phase diagram as a function of the gap parameter M_0. In Fig. 2.7 we show the phase diagram of a magnetically doped thick TI slab as a function of M_0. For $M_0 < 0$ the system is a normal insulator and there are no surface states. Also the spin-orbit coupling is small and the SDW phase does not exist. For $M_0 > 0$ the system is a TI and the gap increases with M_0. TI with larger gaps have more metallic surface states and the FM order at the surface is therefore more robust. Also the effective spin-orbit coupling is stronger and both $T*$ and T_G increase with M_0. The results in Fig. 2.7 show that the range of temperatures where the SDW phase exists increases with M_0.

Finally we make an estimation of the critical temperature. From the band structure parameters of Bi_2Se_3, choosing the density of the magnetic impurities to be $5\text{x}10^{20}cm^{-3}$, the total angular momentum of a single magnetic ion to be $S = 3/2$, and the effective exchange coupling $J_{eff} = 250meVnm^3$ we obtain $T_G^{bulk} \approx 18K$. These values can change by factors of 2 by changing the magnetic ions or the density of impurities. It is well known that the mean-field approximations tend to overestimate the transition temperature due to the neglect of the fluctuations. In diluted magnetic semiconductors thermal fluctuations reduce the value of the Curie temperature in near 30% [58], and we expect a similar reduction in topological insulators.

Part II

CHAPTER 3

Isotropic magnetoelectric effect in topological insulators and multiferroic materials

In collaboration with:
A. V. Balatsky
Nordic Institute of Technology, Stockholm.

We study the possibility of magnetic monopoles in multiferroic materials. An electric charge in the centre of a spherical vacuum surrounded by a multiferroic material would induce an image magnetic monopole charge due to the magneto-electric effect. The monopoles magnetic field could be measured experimentally. We study the time-evolution of the magnetisation and polarisation for this setup and calculate angular frequency in case of a dynamic system.

3.1 Introduction

In 2009 Qi *e*t al. [28] proposed to use topological insulators to observe magnetic monopoles. They showed how to induce an image magnetic monopole using the topological magneto-electric effect. The field created by this magnetic monopole should be measurable. The setup is the following: A point charge is brought into a vacuum of an interface Vacuum-TI system. The charge is positioned at a distance d from the origin along

the z-axis. The charge induces an image charge in the TI as well as two image magnetic monopoles on both sides of the interface.The physical origin of this image magnetic monopole can be understood as a surface current density which is induced by the in-plane component of the electric field. This is the quantum Hall current which induces a magnetic field on both sides of the interface. The important condition which has to be satisfied to have a magnetic monopole without breaking the laws of physics, is $\nabla B = 0$. Qi *e*t al. satisfy this condition by considering a closed surface, in their case a sphere, that encloses a topological insulator (TI). Within this spherical TI the image magnetic monopole gets canceled by a line of magnetic charge density. To measure the local monopole field in the presence of the line of magnetic charge density, the distance of the electric charge from the surface must be much smaller than the radius of curvature of the topological surface. Than the local magnetic field is completely determined by a single image magnetic monopole. In case of impurities Qi *e*t al. found that the magnetic field contribution of the monopole surpasses the contribution of the impurities and stays the dominant contribution. Experimentally this can be realised by deposit-

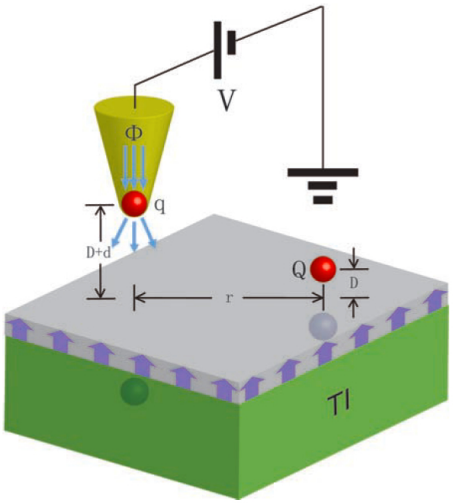

Figure 3.1: Illustration of the experimental setup to measure the image monopole. A magnetic layer is deposit on the surface of the TI, a syndicated by the layer with blue arrows. A scanning MFM tip carries magnetic flux Φ and a charge q. A charged impurity is confined on the surface with charge Q and distance D out of the surface. By scanning over the voltage V and the distance r to the impurity, the effect of the image monopole magnetic field can be measured. Taken from Qi *e*t al. [28].

ing a magnetic layer on the surface of a topological insulator. A scanning MFM tip carries a magnetic flux ϕ and a charge q. A charge impurity is confined on the surface. By scanning over the voltage V and the distance r of the impurity, the effect of the image magnetic monopole can be measured.
In the case of moving electrons on the topological surface, Qi *e*t al. found that the magnetic monopole becomes a dynamical object and bound together with the electron charge it gives a dyon. An interaction between two dyons leads to a Aharonov-Bohm phase. This phase can be interpreted as a statistical angle of the dyon and measured experimentally.
More detailed calculations on topological field theory of time-reversal invariant insulators can be found here[34].
In this abstract we present a similar model for multiferroic (MF) materials. Multiferroics are materials which exhibit more than one primary ferroic order parameter simultaneously. The more common combination is ferromagnetism and ferroelectricity but it is also possible to have a mix with ferroelasticity or ferrotoroidicity. Besides having more than one ferroic parameter, multiferroics are interesting materials due to the fact that it is possible to observe the magneto-electric effect.
The magneto-electric (ME) effect is the phenomenon of inducing magnetic (electric) polarisation by applying an external electric (magnetic) field.
Using the constituent equations we calculate the time dependencies of the magnetisation $\vec{M}$ and the polarisation $\vec{P}$ and present solutions for them.

3.2 Axion Electrodynamics

Constituent Equations for Topological Insulators

The problem can be described similar to the one discussed for topological insulators [28]. With $\kappa = \theta e^2/2\pi^2$ the time-independent constituent equations for TIs are:

$$\mathbf{D} = \mathbf{E} + 4\pi\mathbf{P} - 2\alpha P_3\mathbf{B}, \tag{3.1}$$

$$\mathbf{H} = \mathbf{B} - 4\pi\mathbf{M} + 2\alpha P_3\mathbf{E}, \tag{3.2}$$

with $P_3(x) = \theta(x)/2\pi$ the magneto-electric polarisation.

3.3 Multiferroics

Multiferroics are materials with more than one ferro- property. The most common combination is ferromagnetism and ferroelectricity. Even though several multiferroic (MF) materials have been found it is not trivial to have magnetism and ferroelectricity coexist in one material.
The electric dipole moment arises from a displacement between positive and negative charges. Ferroelectricity is characterised by polarisation when non-magnetic cations shift away from their surrounding anions.
In magnetic materials no dipole moment is formed as the cations here don't shift away from their positions.
Those two behaviours seem to exclude each other and prevent ferroelectricity and magnetism to appear in the same material. But as theories only exist until they are replaced by a better and more accurate theory, the idea of a coexistence of magnetism and ferroelectricity made its way into the text books.
The first discussions of the coupling of magnetic and electric degrees of freedom in insulators was already given by P. Curie in 1894. The magneto-electric effect was what really rose interest in the field of multiferroics. In 1959 Landau and Lifshitz described it as an effect that could exist. E. Dzyaloshinskii was the first to predict the material Cr_2O_3 to exhibit the magneto-electric (ME) effect. Shortly afterwards the relations $M \propto \alpha E$ and $P \propto \beta H$ have been shown experimentally by D. N. Astrov and V. J. Folen respectively.
Since then the publications on the magneto-electric effect have increased largely and many more research group started studying new materials which exhibit this effect.
One of the more promising fields is that of multiferroics (MFs), where a mixture of magnetism and ferroelectricity, creates spontaneous magnetic and dielectric ordering in the absence of an external magnetic or electric field.
$BiFeO_3$ is one of the more popular multiferroics where ferromagnetism and ferroelectricity coexist. In $TbMnO_3$ and $TbMn_2O_3$ magnetism causes ferroelectricity.
These two materials belong to two different classes of MF materials which are distinguished depending on the origin of ferroelectricity and magnetism.
Type I multiferroics are solids where magnetism and ferroelectricity have different sources and appear independently of each other, but not necessarily without coupling to each other. The temperature at which ferroelectricity appears is normally higher here than for magnetism and the

polarisation is large. In type II MFs magnetism causes ferroelectricity and the coupling between them is rather large. The polarisation is much smaller than in type I MFs. Another possibility to find MFs is to create composite materials made of magnets and ferroelectrics put into multilayers and nano structures.
The different sources of type I MFs are multiferroics perovskites, ferroelectricity due to lone pairs, FE due to charge ordering and geometric FE which is explained in details in Ref. [66]. For type II MFs two groups are distinguished by the kind of magnetism which causes ferroelectricity. First come the spiral type-II MFs where magnetic frustration creates spiral magnetic ordering in an insulator. The first to propose this idea was R. Newnham and his coworkers in the 1970's. They realised that the ground state of Cr_2BeO_4, which is centrosymmetric and spiral antiferromagnetic, resulted in a small ferroelectric polarisation [67].
The other group are collinear magnetic structures, where all magnetic moments are aligned along a specific axis. Polarisation here is a consequence of exchange striction when the magnetic coupling varies with the atomic positions. One example is Ca_3CoMnO_6.
Multiferroics are an interesting research object due to its possible values in future applications. Some examples given by D. Khomskii [66] are the possibility to address magnetic memory electrically, new type of 4 stage logic and magneto-electric sensors are just a few possibilities in this field.
In our calculation we use a multiferroic-vacuum interface to realise the magnetic monopoles. As seen in Fig.3.2 a spherical vacuum is surrounded by a MF material with (ϵ_2, μ_2). A charge q is sitting in the centre of the spherical vacuum.
First let's write down the electromagnetic action and derive the constituent equations.

3.4 Electrodynamic Action

The linear response of a conventional insulator is described by S_0:

$$S_0 = \frac{1}{8\pi} \int d^3x dt \left(\epsilon \mathbf{E}^2 - \frac{1}{\mu} \mathbf{B}^2 \right), \tag{3.3}$$

with E and B the electric and magnetic fields and ϵ the relative permittivity and μ the permeability. The additional therm for the coupling of the electric and magnetic fields comes from axion electrodynamics and is given by S_1 [68]:

$$S_1 = \frac{\kappa}{4\pi} \int d^3x dt \mathbf{EB}, \tag{3.4}$$

with κ a phenomenological parameter in the sense of an effective Ginzburg-Landau theory. If κ is constant in space-time the equations of motions are unaffected. For a typical oxide $2 \leq \epsilon \leq 10$ and $\mu > 1$ for paramagnets and $\mu < 1$ for diamagnets with $|\mu - 1| \approx 10^{-4}$. In a magnetoelectric oxide like Cr_2O_3, $\kappa \approx 10^{-4}$.

3.5 Relation between E and P, B and M

In multiferroics the fields are represented by the polarisation **P** and the magnetisation **M** rather than the electric field **E** and the magnetic field **B**. Therefore we have to change the action S_1(**E**,**B**) into S_1(**P**,**M**).

$$P_i = \sum_j \chi^e_{ij} E_j, \tag{3.5}$$

We assume an isotropic MF material with

$$\chi^{e,m}_{ij} = \delta_{ij} \chi^{e,m}, \tag{3.6}$$

where e and m stand for electric and magnetic and χ is the susceptibility. This gives the following relations:

$$\mathbf{P} = \chi^e \mathbf{E}, \tag{3.7}$$

$$\mathbf{D} = \mathbf{E} + 4\pi\mathbf{P} = \epsilon\mathbf{E}, \tag{3.8}$$

$$\mathbf{M} = \chi^m \mathbf{H}, \tag{3.9}$$

$$\mathbf{B} = \mathbf{H} + 4\pi\mathbf{M} = \mu\mathbf{H}. \tag{3.10}$$

3.6 Constituent Equations

Together with Eq. 3.4 and Eqs.3.7-3.10 we can write down the constituent equations for a multiferroic material:

$$\mathbf{D} = \epsilon\mathbf{E} - \kappa\mathbf{B} = \frac{\epsilon}{\chi^e}\mathbf{P} - \frac{\kappa}{\chi^m}\mu\mathbf{M}, \tag{3.11}$$

$$\mathbf{H} = \frac{1}{\mu}\mathbf{B} + \kappa\mathbf{E} = \frac{1}{\chi^m}\mathbf{M} + \frac{\kappa}{\chi^e}\mathbf{P}. \tag{3.12}$$

Isotropic Multiferroics

Examples for isotropic multiferroic materials are given by Hehl *e*t al. [69]. They studied the anti-ferromagnet Cr_2O_3 and mention three different materials where the diagonal terms of the magento-electric tensor α_{11}, α_{22} and α_{33} are equal. These are the isotropic MFs $Cr_3B_7O_13Br$, $Cr_3B_7O_13I$, $Cu_3B_7O_13I$.

3.7 Relation to the Electromagnon

The dynamic properties of several multiferroic materials are governed by the magento-electric modes called electromagnons. Electromagnons are collective excitations of the magnetic structure which are coupled to the electric dipole moment [70]. The first experimental observation of electromagnons was made in 2006 when Pimenov *e*t al.[71] were able to excite spin waves using terahertz light in the multiferroic $TbMnO_3$. They showed that these new excitations can be suppressed using a magnetic field. They used $TbMnO_3$ because it is one of the MF materials with strong magneto-electric coupling where different spin excitations exist.
Electromagnons have also been found in multiferroics of Type I where ferroelectricity does not arise from magnetism.
They do not only exist in multiferroic materials but also exist in a variety of non-collinear spin magnets [72]. Mochizuki and Nagaosa showed theoretically in 2010 [73], that by exciting the electromagnons in the MF Mn pervoskite it is possible to switch the spin chirality. Changing the spin chirality is an important progress for the field of spintronics which aims to electrically control spins. Electromagnons could lead to interesting applications where it would be possible to store the magnetic information via electric fields and manipulate domain walls in ferroelectrics. One example would be when electromagnons could enable ultrafast switching behaviour in materials allowing the manipulation of electronic properties using short-pulsed lasers instead of ultrafast switching magnetic fields.
In the following chapters we while derive the equations for the magnetisation **M** and polarisation **P** including their time dependencies . We will solve these equations for the case that they reduce to the diffusion equation.

3.8 Time dependencies for M and P

To calculate the dynamic magneto-electric effect we need to add time dependencies to the previous equations 3.3 and 3.4. To get the time-dependencies of **M** and **P** we use the formula for the Free Energy:

$$F = \chi_m \mathbf{M}^2 + \chi_p \mathbf{P}^2 + \tfrac{\kappa}{4\pi}\mathbf{MP} + \rho_m(\nabla \mathbf{M})^2 + \rho_p(\nabla \mathbf{P})^2 + \pi_m\left(\tfrac{d\mathbf{M}}{dt}\right)^2 + \pi_p\left(\tfrac{d\mathbf{P}}{dt}\right)^2. \quad (3.13)$$

$$\frac{\delta F}{\delta M} = \chi_m \mathbf{M} + \kappa \mathbf{P} - \rho_m \nabla^2 \mathbf{M} - \pi_m \partial_t^2 \mathbf{M} = 0. \quad (3.14)$$

$$\frac{\delta F}{\delta P} = \chi_p \mathbf{P} + \kappa \mathbf{M} - \rho_p \nabla^2 \mathbf{P} - \pi_p \partial_t^2 \mathbf{P} = 0. \quad (3.15)$$

Where χ_m, χ_p, ρ_m and ρ_p are phenomenological parameters taken from the Ginzburg-Landau theory,

3.9 Solutions for M and P

We start with the following plane wave ansatz for **M** and **P** and insert it in the previous equations 3.14 and 3.15:

$$\begin{aligned} \mathbf{M}(\mathbf{r}, t) &= \vec{M}_0 e^{i\mathbf{kr}} e^{-i\omega t}, \\ \mathbf{P}(\mathbf{r}, t) &= \vec{P}_0 e^{i\mathbf{kr}} e^{-i\omega t}. \end{aligned} \quad (3.16)$$

To have a solution the determinant of the following matrix has to be zero.

$$\begin{pmatrix} \chi_m + \rho_m|\mathbf{k}|^2 + \pi_m\omega^2 & \kappa \\ \kappa & \chi_p + \rho_p|\mathbf{k}|^2 + \pi_p\omega^2 \end{pmatrix} \begin{pmatrix} \tilde{M}_0 \\ \tilde{P}_0 \end{pmatrix} = 0, \quad (3.17)$$

with $\tilde{M}_0$= $\mathbf{M}_0 e^{i\mathbf{kr}} e^{-i\omega t}$ and $\tilde{P}_0$=$\mathbf{P}_0 e^{i\mathbf{kr}} e^{-i\omega t}$. From which we can write an equation for ω_m:

$$\omega_\pm^2 = \frac{-\pi_m(\rho_p|\mathbf{k}|^2+\chi_p)-\pi_p(\chi_m+\rho_m|\mathbf{k}|^2)}{2\pi_m\pi_p} \pm \frac{\sqrt{(\pi_m(\chi_p+\rho_p|\mathbf{k}|^2)+\pi_p(\chi_m+\rho_m|\mathbf{k}|^2))^2+4\pi_m\pi_p(\kappa^2-(\chi_m+\rho_m|\mathbf{k}|^2)(\chi_p+\rho_p|\mathbf{k}|^2))}}{2\pi_m\pi_p}. \quad (3.18)$$

Special case: π_m and $\pi_p = -1$ and $\rho_m = -\rho_p$:

$$\omega_\pm^2 = \tfrac{1}{2}(\chi_p + \chi_m) \pm \tfrac{1}{2}\sqrt{(\chi_p + \chi_m)^2 + 4(\kappa^2 - (\chi_m - |\mathbf{k}|^2)(\chi_p + |\mathbf{k}|^2))}. \quad (3.19)$$

We find that for $\kappa^2 > (\chi_m - |\mathbf{k}|^2)(\chi_p + |\mathbf{k}|^2)$ ω_+^2 is positive. For small $|\mathbf{k}|$ and $\chi_m > \chi_p$ in a range where $|\mathbf{k}|^2 > \kappa^2 + |\mathbf{k}|^4$ and $(\chi_p + \chi_m)^2 > 4(\kappa^2 - (\chi_m - |\mathbf{k}|^2)(\chi_p + |\mathbf{k}|^2))$ also ω_-^2 is positive.
For π_m and $\pi_p = -1$ and small χ_m, $\chi_p \approx 0$ we can rewrite 3.18 into:

$$\omega_\pm^2 = \tfrac{1}{2}(\rho_p + \rho_m)|\mathbf{k}|^2 \pm \tfrac{1}{2}\sqrt{(\rho_p + \rho_m)^2|\mathbf{k}|^4 + 4(\kappa^2 + \rho_m\rho_p|\mathbf{k}|^4)}. \quad (3.20)$$

If we assume the values for $|k|$ to be larger than the phenomenological parameters χ_m, χ_p, ρ_m, ρ_p and κ we find that ω behaves like $|\mathbf{k}|^2$.

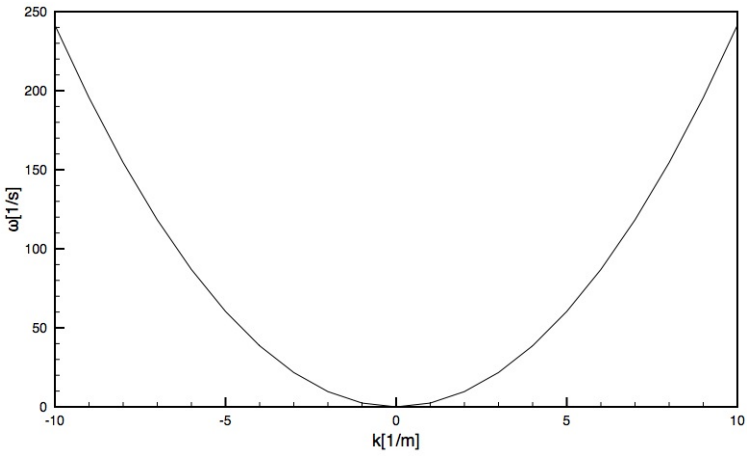

Figure 3.2: Calculation of ω as a function of $|\mathbf{k}|$. The parameters χ_m=χ_p are set to -1 ρ_m=ρ_p =1 and κ=0.

3.10 Conclusion

By adding time-dependencies to the constituent equations we looked at the dynamic magneto-electric effect. In relation to the electromagnon theory we calculated the dynamic equations for the magnetisation and polarisation.

Part III

CHAPTER 4

Optical Properties of Ultra thin Topological Insulators Slabs

Adapted from:
M. Lasia and L. Brey
"Optical properties of magnetically doped ultra-thin topological insulator slabs",
Phys. Rev. B **90**, 075417 (2014).

Starting from a three dimensional Hamiltonian, we study the optical properties of ultra-thin topological insulator slabs for which the coupling between Dirac fermions on opposite surfaces results in two degenerated gapped hyperbolic bands. The gap is a threshold for the optical absorption and translates in a peak in the imaginary part of the optical conductivity. An exchange field applied perpendicular to the slab splits the degenerated hyperbolic bands and a double step structure come out in the optical absorption, whereas a double peak structure appears in the imaginary part of the longitudinal optical conductivity. The exchange field breaks time-reversal symmetry and for exchange fields larger than the surfaces coupling gap, the zero frequency Hall conductivity is quantized to e^2/h. This result implies large values of the Kerr rotation angle and a quantization of the Faraday angle. In ultra-thin slabs, the absence of light multiple scattering and bulk conductivity, makes the Kerr angle to remain rather large in a wide range of frequencies.

4.1 Introduction

Three dimensional (3D) topological insulators (TI's) are materials that possess conducting metallic surface states in the bulk energy gap [1, 31, 74]. These systems typically are band insulators where strong spin orbit coupling alters the natural order in energies of the band structure. At the surface of the TI, in contact with the vacuum, the bands turn back to their natural order, and a two-dimensional metallic state merges at the surface. These surface states have an helical linear dispersion and the quasiparticles are governed by a two-dimensional (2D) massless Dirac equation. The Dirac cone is centered at a time reversal invariant point in the two dimensional Brillouin zone, and the degeneracy at the Dirac point is preserved by time reversal symmetry.

At zero temperature the optical conductivity of a system described by the two-dimensional Dirac Hamiltonian, with the chemical potential located at the Dirac point, gets a universal value $\sigma_0=\frac{\pi}{2}\frac{e^2}{h}$. Light transmittance experiments have confirmed this universal value for the optical absorption in graphene [75, 76]. The optical properties of TI surface states has been theoretically studied recently [77, 78, 79, 80], and the same universal value for the optical conductivity, σ_0, have been obtained [79, 80]. However, hexagonal warping terms in the surface states band structure modify the interband optical transition and deviations from the universal background as seen in graphene[75, 76] have been predicted [77, 78]. The optical conductivity of Bismuth based topological insulators has been experimentally studied[81, 82, 83, 84], and the main result is that the exotic properties of the TI surface states are masked by high carrier densities and impurity band conduction.

The magnetoelectric coupling that occurs at the surfaces of topological insulators [1, 31, 74] is the origin of new and exotic phenomena such as the possibility of inducing magnetic monopoles[28], the tunable Casimir effect [85] and the giant magneto-optical Kerr and Faraday effects [34, 35, 86, 87, 88, 89]. The Kerr and Faraday effects describe the rotation of the light polarization when it is reflected or transmitted respectively by a magnetic material. When time reversal symmetry is broken at the surface of a TI, a gap is induced in the Dirac band structure and the surface shows an anomalous Hall effect, $\sigma_{xy}=\frac{1}{2}e^2/\hbar$. In this situation TI surfaces [34, 35] or clean thin slabs [86, 87] will have a strong magnetoelectric effect that manifest, in ideal systems, in a universal Faraday rotation and a giant Kerr rotation. At the surfaces of TI's the time reversal symmetry can be broken without applying external magnetic fields. Doping the system with magnetic impurities induces an exchange field acting on the TI

surface state [26]. Experiments in Bi_2Se_3 thin films indicate the existence of colossal Kerr [91] and Faraday [92] rotations in the THz regime when time reversal symmetry is broken by a strong magnetic field perpendicular to the slab. The measured Kerr angle is an order of magnitude larger than the observed in high mobility GaAs heterostructres[**?**]. In the quantum Hall regime Faraday and Kerr rotations have been also observed in graphene[93].
Topological insulators as Bi_2Te_3, Bi_2Se_3 and (BiSb)Te, have a layered structure consisting of stacked quintuple layers with relatively weak coupling between them. Therefore, it is possible to prepare these crystals in the form of thin films. In thin films the bulk contribution to electrical conductivity and optical absorption can be reduced considerably, and these systems can be the appropriated geometry to observe surface properties of TI's[26, 94, 95]. When the thickness of the thin film is of the order of the surface-state decay length into the bulk (~ 10nm), the tunnelling between the top and bottom surfaces opens an energy gap and two degenerate massive Dirac bands appear[96, 21, 23, 53]. By increasing the layer thickness the gap decreases and oscillates and the system alternates between a trivial topological phase and a 2D quantum spin Hall topological phase. The existence of this gap indicates that the ultra-thin film behaves as a quasi 2D system, and not as a couple of 2D electron gases separated by a dielectric.
In this work we study the electrical and optical properties of ultra-thin TI slabs in the presence of an exchange field. Starting form a realistic 4×4 $\mathbf{k}\cdot\mathbf{p}$ Hamiltonian we compute the band structure and optical conductivity of TI slabs. The utilization of a realistic bulk Hamiltonian as the starting point releases the use of a momentum or energy cutoff in the calculations. Also, by starting from the 3D Hamiltonian, the surface states dispersion contains automatically quadratic momentum terms and electron hole asymmetry. We study the competition between the confining gap due to the coupling between states on opposite surfaces and the gap induced by the exchange field. Using the Kubo formula we calculate the optical conductivity of the TI slab. The longitudinal conductivity gives information of the optical absorption of the slab, whereas the zero frequency Hall conductivity indicates the topological character of the system. From the optical conductivity we obtain the Kerr and Faraday angles of a ultra thin TI slab. We obtain a giant Kerr angle and a quantized Faraday angle. Both angles get large values in a wide window of low frequencies and because the ultra thin slab behaves as a 2D system they are not affected by TI bulk conductivity or by multiple reflection inside the TI slab.

4.2 Bulk Hamiltonian

The low energy band structure of three dimensional topological insulators in the Bi_2Se_3 family of materials can be described by a four band Hamiltonian proposed by Zhang *e*t al.[100, 53]. In the $\mathbf{k}\cdot\mathbf{p}$ formalism, states near zero energy and long wavelength are governed by a Hamiltonian of the form

$$H^{3D} = E(\mathbf{k}) + \begin{pmatrix} \mathcal{M}(\mathbf{k}) & A_1 k_z & 0 & A_2 k_- \\ A_1 k_z & -\mathcal{M}(\mathbf{k}) & A_2 k_- & 0 \\ 0 & A_2 k_+ & \mathcal{M}(\mathbf{k}) & -A_1 k_z \\ A_2 k_+ & 0 & -A_1 k_z & -\mathcal{M}(\mathbf{k}) \end{pmatrix}, \qquad (4.1)$$

where $\mathcal{M}(\mathbf{k})$=$M_0 - B_2(k_x^2+k_y^2) - B_1 k_z^2$, $k_\pm$=$k_x \pm i k_y$ and $E(\mathbf{k})$=$C + D_1 k_z^2 + D_2(k_x^2+k_y^2)$. The four basis states for which this Hamiltonian is written are $|1\rangle$=$|p1_z^+,\uparrow\rangle$, $|2\rangle$=$-i|p2_z^-,\uparrow\rangle$,$|3\rangle$=$|p1_z^+,\downarrow\rangle$, and $|4\rangle$= $i|p2_z^-,\downarrow\rangle$, which are hybridized states of the Se p orbitals and the Bi p orbitals, with the superscripts $(\pm)$ standing for even and odd parity, and $\uparrow$ and $\downarrow$ for spin up and down respectively. The Hamiltonian parameters for a particular material can be obtained by fitting to density functional band structure calculations [53]. In the case of Bi_2Se_3 the relevant parameters are M_0=0.28eV, A_1=2.2$eV\AA$, A_2=4.1$eV\AA$, B_1=10$eV\AA^2$, B_2=56.6$eV\AA^2$, C=-0.0068eV, D_1=1.3$eV\AA^2$ and D_2=19.6$eV\AA^2$.

Electronic Structure of Topological Insulator Slabs

We analyze a TI slab perpendicular to the z-direction and thickness L. The system is invariant in the (x,y)-plane so that k_x and k_y are good quantum numbers. The eigenvalues, $\varepsilon_{n,\mathbf{k}}$, and wavefunctions, $\Psi_{n,\mathbf{k}}(z)$, are obtained by solving Eq.4.1 with $k_z = -i\partial_z$ and forcing the wavefunction to vanish at the surfaces of the slab, $z=0$ and $z=L$. This is satisfied expanding $\Psi_{n,\mathbf{k}}(z)$ in harmonics, of the form $\sin(\frac{l}{L}\pi z)$, being l a positive integer[53]. For a given two-dimensional wavevector, $\mathbf{k}$ =(k_x,k_y), we diagonalize the Hamiltonian in this basis and we obtain a discrete number of eigenvalues, $\varepsilon_{n,\mathbf{k}}$ and the corresponding wavefunctions,

$$\Psi_{n,\mathbf{k}}(z) = \frac{e^{i\mathbf{k}\mathbf{r}}}{\sqrt{A}}\sqrt{\frac{2}{L}}\sum_{l=1}^{N_{\max}}\sum_{j=1,4} a_{n,j}^{l}(\mathbf{k})\sin(l\pi\frac{z}{L})\,|j\rangle\ , \qquad (4.2)$$

here A is the sample area. The number of harmonics used in the expansion, N_{max}, depends on the thickness of the slab, and it is chosen large enough so that the results do not depend on its value. In Fig.4.1 we

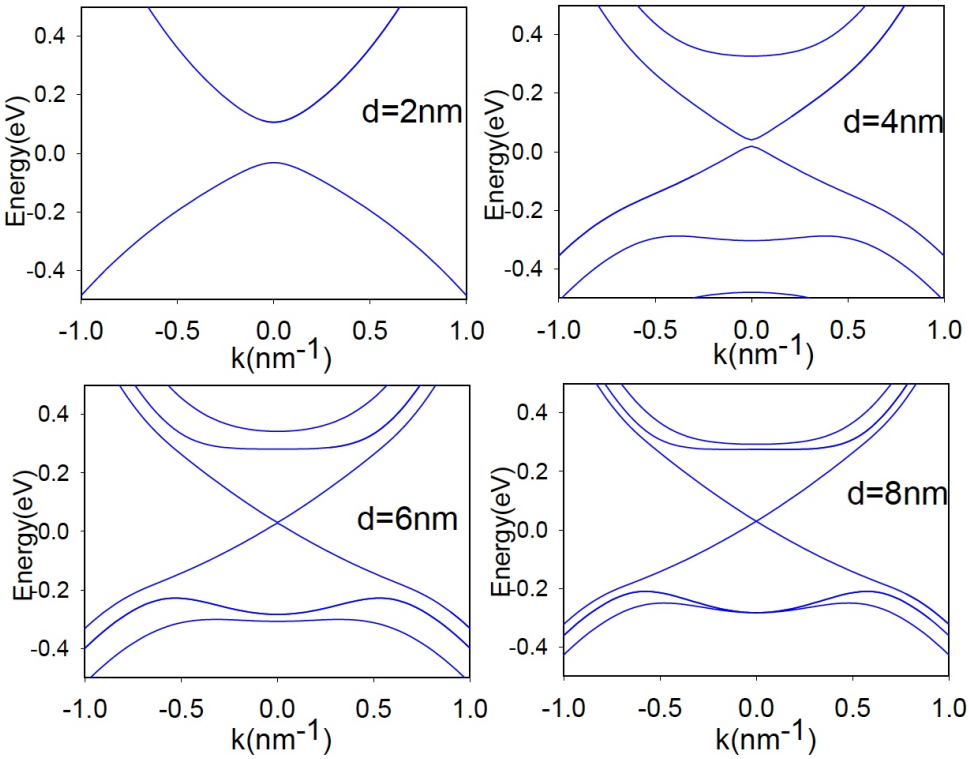

Figure 4.1: (Color online) Band structure of TI slabs of different thickness d. The slabs are perpendicular to the $\hat{z}$ direction. The electronic sates are obtained by diagonalizing Hamiltonian Eq. 4.1 with the appropriated boundary conditions. At the Brillouin zone center, Γ, the bulk gap has a value $2M_0$=0.56eV. Energies inside the bulk energy gap correspond to surface states. For thick slabs low energy surface states dispersion has the form of a Dirac-cone. For thin slabs, coupling between surface states located on opposite surfaces opens an energy gap in the Dirac spectrum. The system has circular symmetry and we plot the bands as function of the absolute value of the in-plane wavevector **k**.

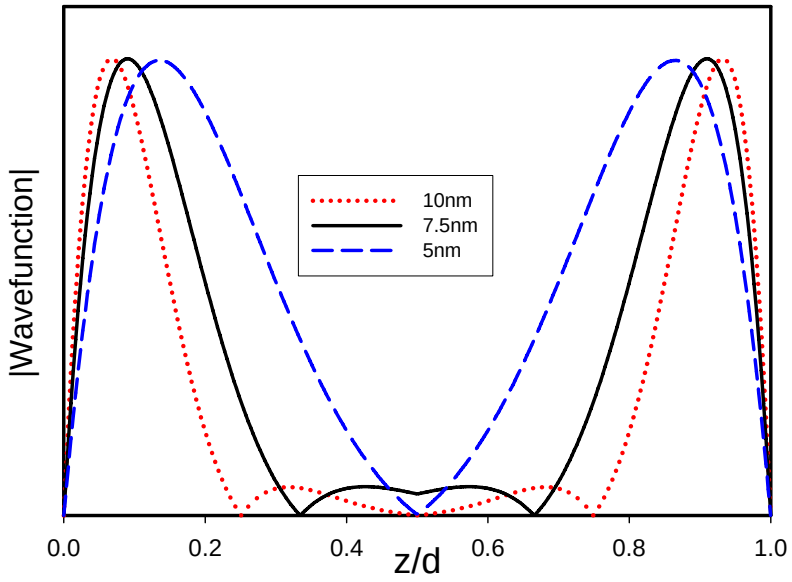

Figure 4.2: (Color online) Absolute value of the wavefunction, as function of the position along the slab, of a surface state with momentum close to zero, for different TI slab thickness. In the inset we plot the variation of the TI slab energy gap as a function of the thickness.

plot the band structure of thin TI slabs for different values of the thickness d. For thick TI slabs ($d > 6nm$) the surfaces are decoupled and two degenerated gapless Dirac-like bands, one for each surface, appear in the bulk energy gap region. This is the benchmark of the TI. As the thickness of the slab decreases the electronic states localized on opposite surfaces couple and the Dirac cones transform in two degenerated hyperbolic Dirac bands with gap E_g at the centre of the Brillouin zone Γ. In agreement with previous works[96, 21, 23, 99] the values of this gap oscillates as function of the thickness d. For each set of gapped Dirac bands, the expectation value of the spin in the valence and conduction bands, gets a **k**-dependent configuration near the centre of the Brillouin zone[99, 23]. Because of time reversal symmetry, the other pair of Dirac hyperbolas is a degenerated copy with the opposite **k**-dependent spin configuration[99, 23].
The energy gap for the Dirac fermions occurs when the thickness of the TI slab is comparable with the decay length of the surface state wave function into the film. In that case opposite surface wave functions overlap

leading to the appearance of the energy gap at the center of the Brillouin zone. In Fig.4.2 we plot the absolute value of the wave function of a surface state with momentum close to zero for different values of the layer thickness. If we turn the parameters D_1 and D_2 to zero, it is possible to obtain analytically that the four components of the surface wavefunction have the same dependence on the position across the TI slab,

$$f(z) = e^{\lambda_1 z} \sin \lambda_2 z \tag{4.3}$$

with

$$\lambda_1 + i\lambda_2 = \frac{A_1 + i\sqrt{|A_1^2 - 4M_0 B_1|}}{2B_1} \ . \tag{4.4}$$

From the Bi_2Se_3 band structure parameters we get $\lambda_1 \sim 1.1nm^{-1}$ and $\lambda_2 \sim 1.26nm^{-1}$ in rather good agreement with the decays length and zeros of the wavefunction in Fig.4.2. From this values of the decay length, we conclude that in TI slabs thinner than 6nm, there is coupling between top and bottom surfaces and the system can not be described as a couple of two dimensional gases separated by a dielectric. It is more appropriated describe the TI slab as a 2D system.

Spectrum of a TI slabs in presence of a Exchange field

An exchange field directed along the z-direction affects strongly the electronic properties of TI surfaces. The Dirac Hamiltonian describing electrons moving on a surface perpendicular to the z-direction has the form H=$\hbar v_F(\sigma_x k_y - \sigma_y k_x)$[53, 54]. Here the Pauli matrices σ_x and σ_y correspond to the electron spin operators and v_F is the Fermi velocity. An exchange field Δ_z pointing in the z-direction opens a gap in the surface bands and the system becomes a topological insulator showing a Hall conductivity σ_{xy}=$1/2e^2/h$. The presence of different oriented surfaces in real crystals, makes that measured Hall conductances become always integrally quantized[102, 103, 104].
We study the effect of a exchange field on the properties of a TI thin film, by adding to the bulk Hamiltonian Eq.4.1 an exchange term of the form $\Delta_Z I \otimes \sigma_z$. The slab geometry is introduced by means forcing the wavefunctions to satisfy the boundary conditions Eq.4.2. In Fig.4.3 we plot the band structure of thin TI slabs for different values of the thickness d and a typical exchange field Δ_z=50meV. For thick slabs where opposite surfaces are decoupled, the exchange field polarizes, near **k**=0, the spin of the conduction(valence) band in the $+(-)$ z-direction. Then a gap of magnitude $2\Delta_z$ appears and the bands get a quadratic dispersion. Away

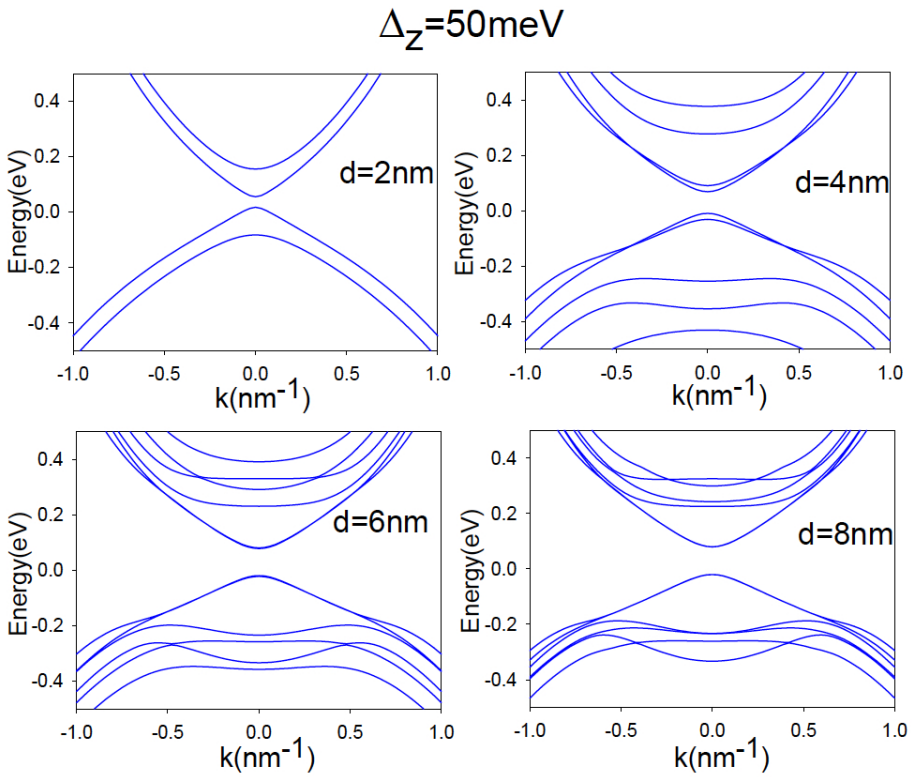

Figure 4.3: (Color online) Band structure of TI slabs of different thickness d, in presence of an exchange field, Δ_z=50meV, applied in the z-direction. The slabs are perpendicular to the $\hat{z}$ direction. The electronic sates are obtained by diagonalizing Hamiltonian Eq. 4.1 with the appropriated boundary conditions. The system has circular symmetry and we plot the bands as function of the absolute value of the in-plane wavevector **k**.

from the center of the Brillouin zone, the bands recover the linear dispersion and the spin texture dictated by the Dirac equation is restored. At Δ_z=0, ultra thin TI slabs have two degenerated hyperbolic Dirac bands with opposite spin texture. The exchange field breaks the time reversal symmetry, and near **k**=0 the bands split in two states with spin up and energies $\pm E_g/2+\Delta_z$ and two spin down states with energies $\pm E_g/2-\Delta_z$.

4.3 Optical conductivity

The optical conductivity $\sigma_{\alpha,\beta}$ relates, in the linear response, the electrical current in a direction α to an external transverse electric field applied in

the β-direction. The optical conductivity consists of two pieces, the diamagnetic term and the paramagnetic term[105]. The paramagnetic term can be obtained from the current-current correlation function using the Kubo formalism. However the diamagnetic term is not always well described in continuos effective models. In particular, in the Dirac Hamiltonian the diamagnetic term vanishes because $\partial^2 H/\partial k^2$=0 [106, 107].
Both the diamagnetic and paramagnetic contributions contains a delta singularity at frequency ω=0. The total weight of the delta is the Drude weight or charge stiffness and indicates the ability of the carriers to move freely when an electric field is applied. In this work we are considering undoped systems with no carriers at the Fermi energy and therefore the delta function should have null weight. To achieve this, we use the following expression[108] for the optical conductivity that cancel the delta singularity at ω=0, and guarantees a zero charge stiffness in the systems,

$$\sigma_{\alpha,\beta} = i\frac{e^2\hbar}{V}\int \frac{d^2\mathbf{k}}{(2\pi)^2}\sum_{m,n}\frac{n_F(\varepsilon_{n,\mathbf{k}})-n_F(\varepsilon_{m,\mathbf{k}})}{\varepsilon_{m,\mathbf{k}}-\varepsilon_{n,\mathbf{k}}}\frac{<n,\mathbf{k}|j_\alpha|m,\mathbf{k}><m,\mathbf{k}|j_\beta|n,\mathbf{k}>}{\hbar(\omega+i\eta)-(\varepsilon_{m,\mathbf{k}}-\varepsilon_{n,\mathbf{k}})} \quad (4.5)$$

In this expression $|m,\mathbf{k}>$ and $\varepsilon_{m,\mathbf{k}}$ are the eigenfunction and eigenvalues respectively of the system with sub-band m and wavevector $\mathbf{k}$, n_F is the fermi occupation, and $\hbar\eta$ represents the quasiparticle lifetime broadening. The current operators are obtained from the Hamiltonian through j_α=-$\partial H/\partial k_\alpha$.
Note that we do not need to include and energy cutoff in the calculation of the optical conductivity. The number of surface states is naturally limited by the bulk bands of the TI.

Zero exchange field

For zero exchange field the system has time reversal symmetry and the non-diagonal components of the conductivity tensor are zero. Also because of the circular symmetry of the Hamiltonian the system is isotropic and σ_{xx}=σ_{yy}. In Fig.4.4 we show the optical conductivity as a function of frequency for TI slabs of different thickness. We first discuss the optical conductivity of uncoupled surfaces. In the insets of Fig.4.4 we plot the conductivity for a layer thickness d=20nm. For this thickness electronic states of both surfaces are decoupled and the dispersion near the centre of the Brillouin zone is linear. Then at small ω, the imaginary part of the optical absorption is zero and the real part get the value σ_0=$\frac{\pi}{4}\frac{e^2}{h}$. The value of σ_0 is half the value of the optical conductivity of graphene monolayer[109, 110], because although there is a Dirac cone at each surface, they are not spin degenerated. At frequencies near 0.35eV the dis-

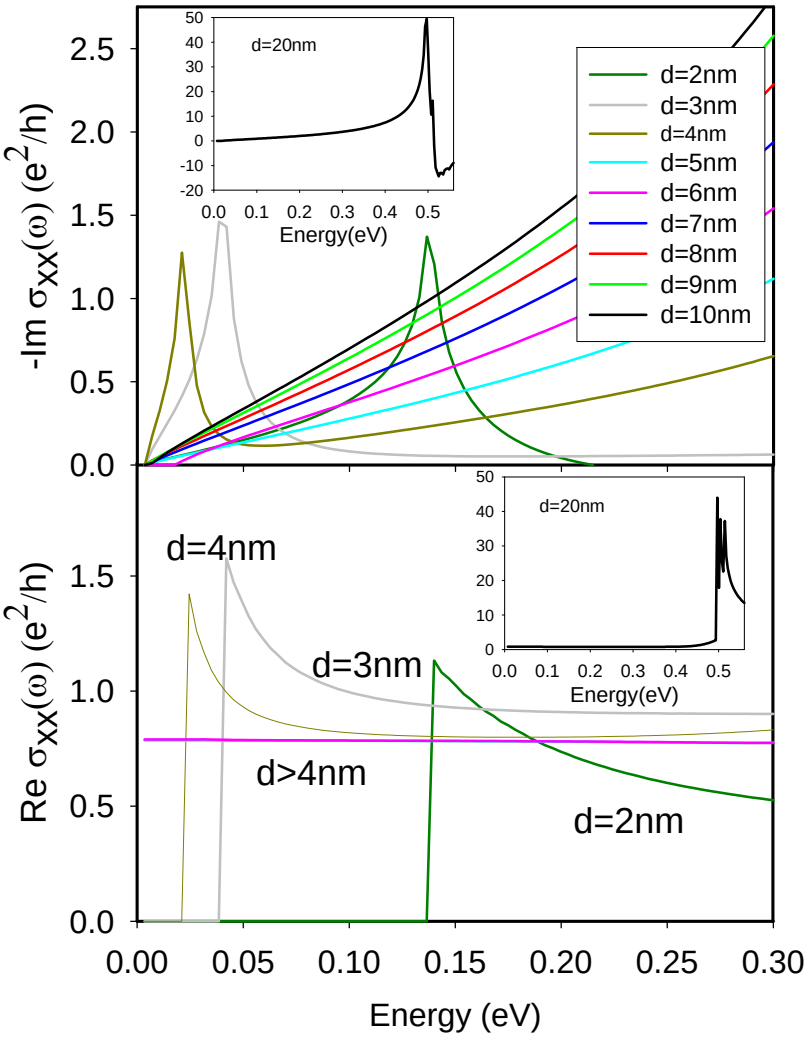

Figure 4.4: (Color online) Imaginarty (top) and real (bottom) part of the optical conductivity as a function of frequency, for a TI slab of different thicknesses. In the insets we show the optical conductivity for a thick slab, d=20nm with states in opposite surfaces practically decoupled

persion relation deviates from the linear behaviour and the real part of the conductivity increases continuously with ω and presents a strong peak at the TI energy gap. The imaginary part increases continuously from zero and present a peak valley structure at the bulk energy gap.
At smaller layer thickness the coupling between opposite surface states opens a gap that suppress the optical absorption at frequencies smaller than the gap. At $\hbar\omega$=E_g, the hyperbolic dispersion and the modification of the spin texture near Γ increases the number of $\mathbf{k}$ states that participate in the transition and this produces a peak superposed to a step in the real part of σ_{xx}. As the gap reduces the step in $Re(\sigma_{xx})$ tends to σ_0 and the peak disappears. The gap, also induces a peak in the imaginary part of σ_{xx} which indicates the existence of an interband charge collective excitation.

Finite exchange field

The exchange field breaks time reversal symmetry and the non-diagonal part of the optical conductivity gets a finite value. For thin gapped TI slabs, the exchange field polarizes the spin in the extremes of the bands, and the dissipative parts of the response functions $Re(\sigma_{xx})$ and $Im(\sigma_{xy})$ show two absorption edges at energies $2\Delta_z \pm E_g$. The splitting of the bands also reflects in the appearance of two peaks in Imσ_{xx} and $Re(\sigma_{xx})$. At large separation between the bands only an absorption edge and a peak occur at energy $2\Delta_z$.
A TI slab in presence of an exchange field has always an insulator character. The band insulator or topological insulators nature of this phase may be known by computing the Chern number, which in this system[1, 111] coincides with the value of the dc Hall conductivity. In Fig.4.7 we plot the Hall conductivity as function of d and Δ_z. For values of the exchange field smaller than twice the tunneling gap, the slab is a normal insulator, however for larger values of Δ_Z, the TI slab acquires an integer anomalous Hall conductivity, σ_{xy}=e^2/h. Then as a function of the exchange field or the slab thickness, TI slabs undergo quantum phase transitions from band to topological insulator. The system only presents an anomalous quantum Hall effect when the surface bands are inverted by the exchange field, independently of the sign of the tunneling gap between the surfaces. For very large values of d, the integer quantized Hall conductivity may be understood as the sum of two half quantized Hall conductivities, one for each uncoupled surface.

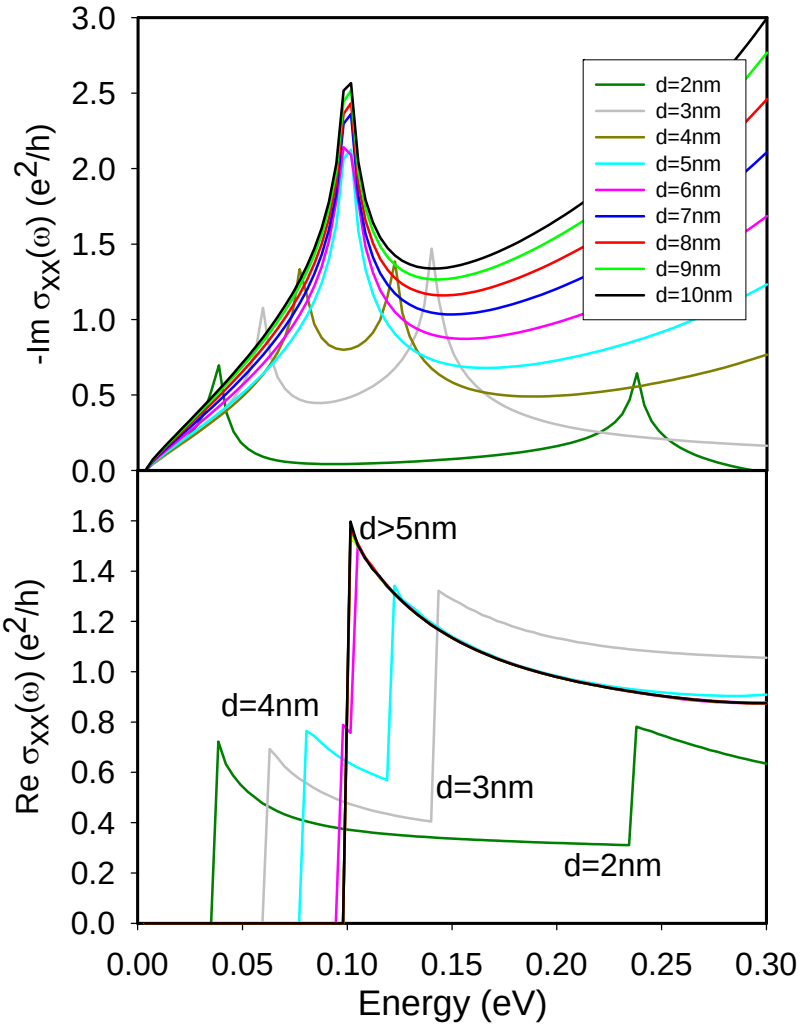

Figure 4.5: (Color online) Imaginary (top) and real (bottom) part of the longitudinal optical conductivity as a function of frequency, for a TI slab of different thicknesses, in presence of an exchange field Δ_z=50meV.

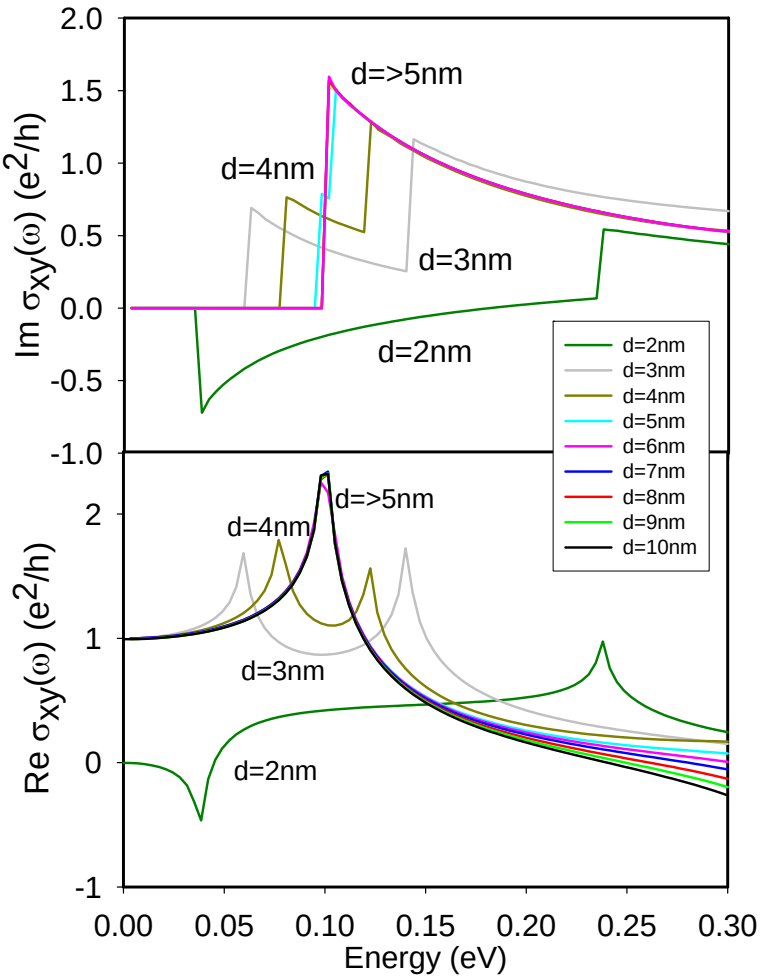

Figure 4.6: (Color online) Imaginary (top) and real (bottom) part of the Hall optical conductivity as a function of frequency, for a TI slab of different thicknesses, in presence of an exchange field Δ_z=50meV.

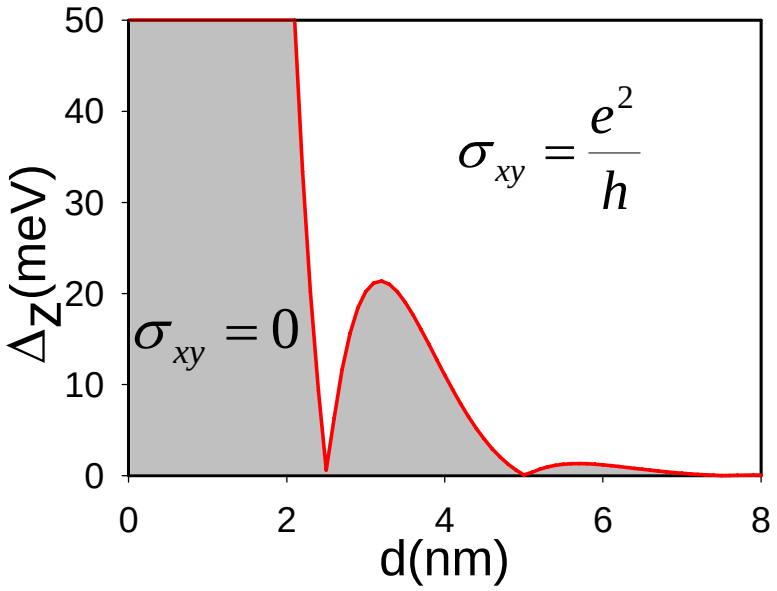

Figure 4.7: (Color online) Phase diagram, as function of d and Δ_z, for the anomalous quantum Hall effect of a TI slab perpendicular to the z-direction.

4.4 Kerr and Faraday angles

Finite values of the Hall conductivity in magnetically gapped TI surfaces imply interesting properties in their optical properties. When $\sigma_{xy} \neq 0$, left and right handed circularly polarized light, propagating perpendicular to the TI slab, have different refraction and transmission indices. As a consequence, linear polarized light rotates its polarization direction when transmitted or reflected by a TI slab in the anomalous quantum Hall regime. The transmitted and reflected rotation angles of linear polarized light are called Kerr (θ_K) and Faraday (θ_F) respectively.
Because of the overlap between electronic states localized on opposite surfaces, ultra thin TI slabs should be considered as a single two dimensional electron system. Furthermore, the light wavelength is much larger than the slab thickness and the light electromagnetic fields are practically constants across the slab. In this situation, the electromagnetic properties of the thin TI slab are described just by the two dimensional conductivity tensor. Transmission and reflection of light are obtained by considering two dielectric materials separated by an interface character-

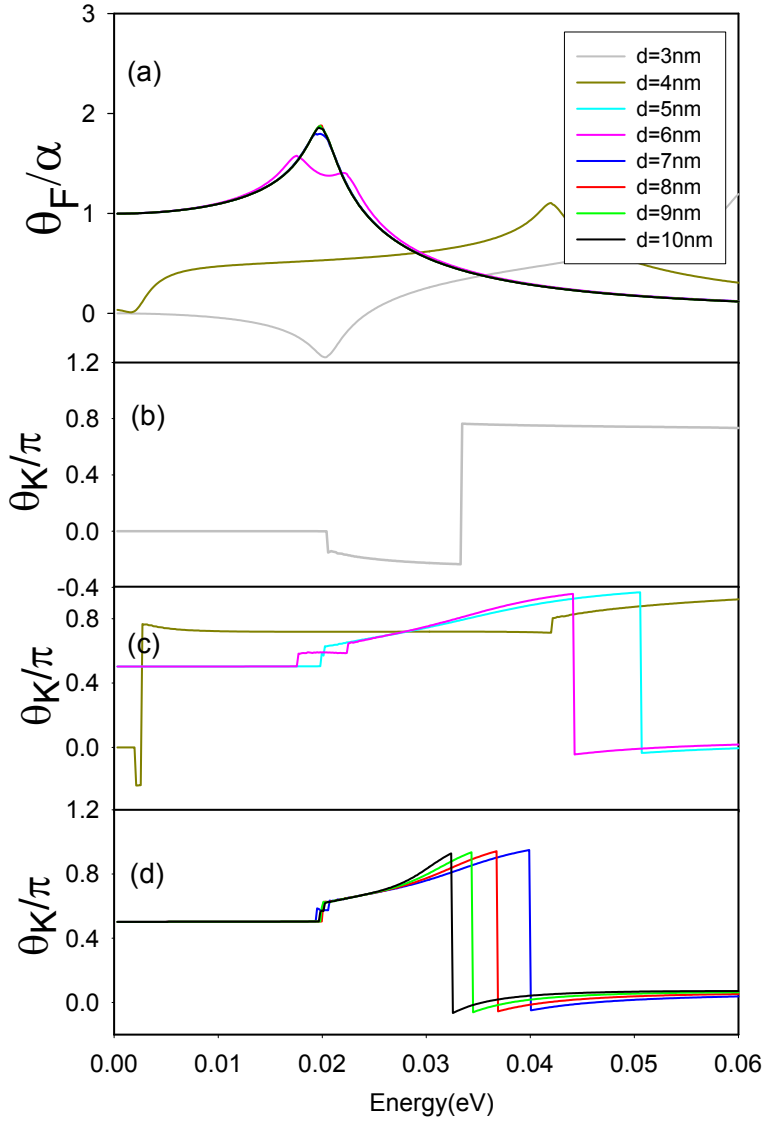

Figure 4.8: (Color online) Faraday and Kerr angles for TI slabs of different thicknesses in presence of an exchange field Δ_z=10meV.

ized by a conductivity tensor. The Maxwell equations dictate the boundary conditions for the electromagnetic fields. For a free standing slab and normal incidence, the reflection, $\bar{r}$=$\begin{pmatrix} r_{xx} & r_{xy} \\ -r_{xy} & r_{xx} \end{pmatrix}$ and transmission, $\bar{t}$=$\begin{pmatrix} t_{xx} & t_{xy} \\ -t_{xy} & t_{xx} \end{pmatrix}$ tensors for the electric field have the form[87],

$$\begin{aligned} r_{xx} &= \frac{1-(1+\frac{4\pi}{c}\sigma_{xx})^2-(\frac{4\pi}{c}\sigma_{xy})^2}{(2+\frac{4\pi}{c}\sigma_{xx})^2+(\frac{4\pi}{c}\sigma_{xy})^2} \\ r_{xy} &= \frac{-\frac{8\pi}{c}\sigma_{xy}}{(2+\frac{4\pi}{c}\sigma_{xx})^2+(\frac{4\pi}{c}\sigma_{xy})^2} \\ t_{xx} &= \frac{4+\frac{8\pi}{c}\sigma_{xx}}{(2+\frac{4\pi}{c}\sigma_{xx})^2+(\frac{4\pi}{c}\sigma_{xy})^2} \\ t_{xy} &= \frac{-\frac{8\pi}{c}\sigma_{xy}}{(2+\frac{4\pi}{c}\sigma_{xx})^2+(\frac{4\pi}{c}\sigma_{xy})^2}\,. \end{aligned} \tag{4.6}$$

and the Kerr and Faraday angles are given by,

$$\begin{aligned} \theta_F &= arg(t_{xx}+it_{xy}) \\ \theta_K &= arg(r_{xx}+ir_{xy}) \end{aligned} \tag{4.7}$$

In Fig.4.9 we plot the Kerr and Faraday angles for TI slabs with thickness ranging from d=2nm to d=10nm, in presence of an exchange field Δ_z=50meV.

For $\Delta_z \neq$0, TI slabs exhibit anomalous quantum Hall effect characterized by $\sigma_{xx}(\omega=0)$=0, $Re(\sigma_{xy}(\omega=0))$=0 and$Im(\sigma_{xy}(\omega=0))$=$e^2/h$, then the Kerr angle, Eq.4.6, gets a large (giant) values θ_K=-$\pi/2$ and the Faraday gets a quantized value θ_F=α, being α=$e^2/\hbar c$=1/137 the vacuum fine structure constant[86, 87]. Absolute values of both angles decay with frequency and present peaks at the optical absorption edges ω=$2\Delta_z \pm E_g$. The results indicate that in a wide range of frequencies, linear polarized light gets a large rotation in its polarization when reflected or transmitted by an ultra thin TI slab. The small value of the slab thickness makes this result rather robust. For ultrathin TI slabs the bulk contribution to the electronic conductivity is totally suppressed and the values of θ_K and θ_F are not affected by bulk free carriers supply by bulk defects. Also because the thickness of the slab is much smaller than the light wavelength, the optical path of the light inside the TI slab is zero and there is not suppression of θ_K and θ_F by multiple reflections in side the TI slab. We then conclude that in ultrathin TI slabs there is a wide range of frequencies where the Kerr and Farady angles get large values.

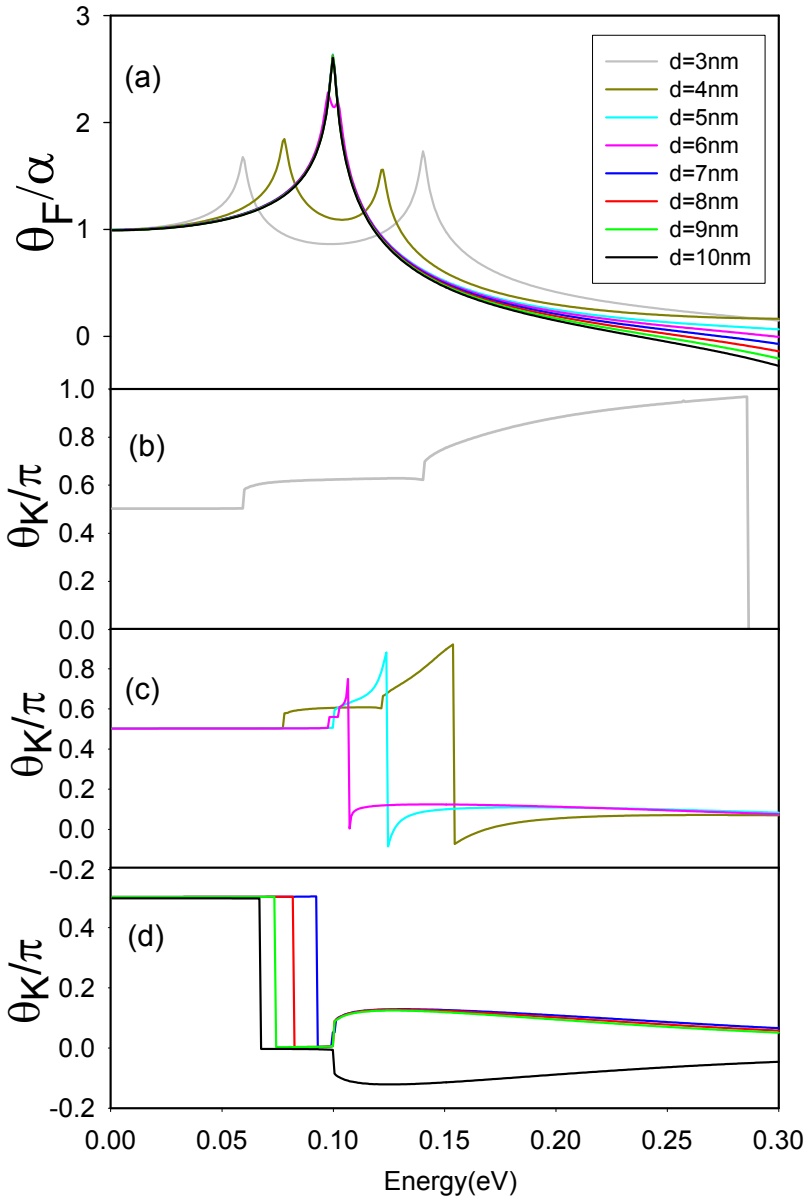

Figure 4.9: (Color online) Faraday and Kerr angles for TI slabs of different thicknesses in presence of an exchange field Δ_z=50meV.

4.5 Conclusions

We have studied the band structure and optical properties of ultra-thin topological insulator slabs. The electronic properties are obtained starting from a three-dimensional $\mathbf{k} \cdot \mathbf{p}$ Hamiltonian, so that our calculations do not depend on energy or momentum cutoff. For the optical conductivity we use an expression (Eq.4.5) that describes correctly both the diamagnetic and the paramagnetic contributions, and therefore we obtain the real and imaginary part of the conductivity directly from it.
In thin TI slabs, the coupling between opposite surface states opens a gap in the electronic spectrum that inhibits optical absorption for frequencies smaller than the gap E_g. The gap also reflects in a peak at $\hbar\omega$=E_g in the imaginary part of $\sigma_{xx}(\omega)$. This peak indicates the existence of an interband charge excitation.
An exchange field Δ_z applied perpendicularly to the TI slab, breaks time-reversal symmetry and splits the gapped bands of ultra-thin TI slabs. The real part of the longitudinal optical conductivity shows absorption edges at energies $2\Delta_z \pm E_g$, whereas the imaginary part presents peaks at the same energies. For values of the exchange field $2\Delta_z > E_g$, the zero frequency Hall conductivity is quantized to the value $\sigma_x y$=e^2/h. This large value of the Hall conductivity produces a strong rotation of the polarization of light when transmitted through or reflected in the TI slab. At zero frequency the Faraday angle gets the value θ_F=$e^2/\hbar c$=$1/137$ and presents peaks at frequencies $2\Delta_z \pm E_g$. The Kerr rotation gets a value θ_K=$-\pi/2$ at zero frequency and gets rather large absolute values at finite frequencies. These values of the Faraday and Kerr rotation angles are rather robust because they are not affected by bulk carriers or by light multiple scattering in the topological insulator ultra-thin slab.

Appendix

APPENDIX A

Effective continuous model

In this chapter, an effective continuous model for the surface states and ultra thin film of TIs is presented. Starting with a 3D effective low-energy model based on first-principles calculations [19], the solutions for the surface states and the corresponding spectra for a semi-infinite boundary condition of gapless Dirac fermions and for the thin film of TIs are given. We use the Hamiltonian 1.10, and confirm the calculations done for an anisotropic description of the surface states of the topological insulator Bi_2Se_3 in the work of Shan *e*t al. [112].

A.1 Dirac Hamiltonian for the surface states

The surface states of a topological insulator have a conical energy spectrum, characteristic of Eigenmodes of the massless Dirac equation.
The surface states for the (111) orientation can be described by the two-dimensional Dirac Hamiltonian:

$$H^{2D}_{Dirac} = v_f(\sigma_x p_y - \sigma_y p_x). \tag{A.1}$$

The operator $\sigma = (\sigma_x, \sigma_y, \sigma_z)$ is usually identified with the true electron spin. The spin polarisation is then perpendicular to the electrons momentum, which leads to the surface states being referred to as helical.

A.2 Bulk properties

Hamiltonian

To investigate the relation between σ and the true spin of the system we start from the low-energy Hamiltonian for Bi_2Se_3.
The properties of three dimensional topological insulators can be described by the four band Hamiltonian introduced by Zhang *e*t al.[19]. In the $\mathbf{k}\cdot\mathbf{p}$ approximation the low energy long wavelength properties of Bi_2Se_3 are determined by the Hamiltonian,

$$\begin{aligned} H^{3D} &= E(\mathbf{k}) \\ &+ \begin{pmatrix} \mathcal{M}(\mathbf{k}) & A_1k_z & 0 & A_2k_- \\ A_1k_z & -\mathcal{M}(\mathbf{k}) & A_2k_- & 0 \\ 0 & A_2k_+ & \mathcal{M}(\mathbf{k}) & -A_1k_z \\ A_2k_+ & 0 & -A_1k_z & -\mathcal{M}(\mathbf{k}) \end{pmatrix}, \end{aligned} \tag{A.2}$$

where $\mathcal{M}(\mathbf{k})=M_0-B_2(k_x^2+k_y^2)-B_1k_z^2$, $k_\pm=k_x\pm ik_y$ and $E(\mathbf{k})=C+D_1k_z^2+D_2(k_x^2+k_y^2)$.
The Hamiltonian is written in the basis $|1\rangle=|p1_z^+,\uparrow\rangle$, $|2\rangle=-i|p2_z^-,\uparrow\rangle$, $|3\rangle=|p1_z^+,\downarrow\rangle$, $|4\rangle=i|p2_z^-,\downarrow\rangle$, which are the hybridized states of the Se p orbital and the Bi p orbital with even $(+)$ and odd $(-)$ parities and spin up ($\uparrow$) and down ($\downarrow$). The Hamiltonian parameters for Bi_2Se_3 are taken from reference [19] , M_0=0.28eV, A_1=2.2$eV\AA$, A_2=4.1$eV\AA$, B_1=10$eV\AA^2$, B_2=56.6$eV\AA^2$, C=-0.0068eV, D_1=1.3$eV\AA^2$ and D_2=19.6$eV\AA^2$. For a given eigenvalue $\varepsilon_{n,\mathbf{k}}$, the eigenvector has the form

$$\Psi_{n,\mathbf{k}}=\frac{e^{i\mathbf{kr}}}{\Omega}\sum_l \alpha_l^{n,\mathbf{k}}|l\rangle \ , \tag{A.3}$$

where Ω is the sample volume. In this basis the spin operators get the form,

$$\begin{aligned} S_z &= \begin{pmatrix} 1 & 0 & 0 & 0 \\ 0 & 1 & 0 & 0 \\ 0 & 0 & -1 & 0 \\ 0 & 0 & 0 & -1 \end{pmatrix}, S_x = \begin{pmatrix} 0 & 0 & 1 & 0 \\ 0 & 0 & 0 & -1 \\ 1 & 0 & 0 & 0 \\ 0 & -1 & 0 & 0 \end{pmatrix} \\ &\text{and } S_y = \begin{pmatrix} 0 & 0 & -i & 0 \\ 0 & 0 & 0 & i \\ i & 0 & 0 & 0 \\ 0 & -i & 0 & 0 \end{pmatrix}. \end{aligned} \tag{A.4}$$

The localized states at the surface $x = 0$, the basis of this Hamiltonian are the states $(i, 1, 0, 0)e^{i\mathbf{kr}}$ and $(0, 0, 1, i)e^{i\mathbf{kr}}$. For the surface $x = L$ the states $(-i, 1, 0, 0)e^{i\mathbf{kr}}$ and $(0, 0, -1, i)e^{i\mathbf{kr}}$ form the basis.
The low-energy Hamiltonian A.2 contains both the true electron spin and a pseudospin as its primary degrees of freedom, where the pseudospin refers to states with support on the Bi and Se sublattices.
In the following we derive the general solutions for three different surface orientations (x, y), (y, z) and (x, z). We present the different Dirac Hamiltonians and plot the band structure for each orientation when the surface is doped with magnetic impurities.

General Solution of the surface states for the (x,y) surface

Analog to the work of Shan et al. [112] we use the four-component trivial solution

$$\psi = \psi_\lambda e^{\lambda z}, \tag{A.5}$$

in the Schrödinger equation (E is the Eigenvalue of Energy)

$$\tilde{H}(k, -i\partial_z)\psi = E\psi. \tag{A.6}$$

The secular equation

$$\det|\tilde{H}(k, -i\lambda) - E| = 0, \tag{A.7}$$

gives four solutions of $\lambda(E)$, denoted as $\beta\lambda_\alpha(E)$, with $\alpha \in \{1, 2\}, \beta \in \{+, -\}$ and

$$\lambda_\alpha(E) = \left[-\frac{F}{2D_+D_-} + (-1)^{\alpha-1}\frac{\sqrt{R}}{2D_+D_-} \right]^{\frac{1}{2}}. \tag{A.8}$$

where for convenience we have defined

$$\begin{gathered} F = A_1^2 + (E - L_1)D_+ - (E - L_2)D_-, \\ R = F^2 - 4D_-D_+ \left[(E - L_1)(E - L_2) - A_2^2k_y^2 - A_2^2k_+k_- \right], \\ D_\pm = D_1 \pm B_1, \\ L_1 = C + M_0 + (D_2 - B_2)k^2, \\ L_2 = C - M_0 + (D_2 + B_2)k^2. \end{gathered} \tag{A.9}$$

We use these definitions to transform the Hamiltonian A.2 into the following version:

$$\tilde{H}^{3D} = \begin{pmatrix} L_1 - D_-\lambda^2 & -iA_1\lambda & 0 & A_2k_- \\ -iA_1\lambda & L_2 - D_+\lambda^2 & A_2k_- & 0 \\ 0 & A_2k_+ & L_1 - D_-\lambda^2 & iA_1\lambda \\ A_2k_+ & 0 & iA_1\lambda & L_2 - D_+\lambda^2 \end{pmatrix} \tag{A.10}$$

The Eigenvalues are doubly degenerated and given by

$$E_{\pm} = \frac{1}{2}(L_1 + L_2 - (D_+ + D_-)\lambda^2) \pm \sqrt{4A_2k_+k_- - 4A_1^2\lambda^2 + (L_1 + L_2 - (D_+ + D_-)\lambda^2)^2 + 4(D_+L_1\lambda^2 + D_-L_2\lambda^2 - D_+D_-\lambda^4)}. \quad \text{(A.11)}$$

Because of double degeneracy, each of the four $\beta\lambda_\alpha(E)$ corresponds to two linearly independent four-component vectors, found to be

$$\Psi_{\alpha\beta 1} = \begin{pmatrix} E_{\pm} - L_2 + D_+\lambda_\alpha^2 \\ -iA_2\lambda_\alpha^2 \\ 0 \\ A_2k_+ \end{pmatrix}, \quad \text{(A.12)}$$

$$\Psi_{\alpha\beta 2} = \begin{pmatrix} -iA_2\lambda_\alpha^2 \\ E_{\pm} - L_1 + D_-\lambda_\alpha^2 \\ A_2k_+ \\ 0 \end{pmatrix}. \quad \text{(A.13)}$$

Finite Boundary Conditions for the (x,y) surface

The surface states have a finite distribution near the boundary. For a film thick enough that the states at opposite surfaces barely couple to each other, we can focus on just one surface. Without loss of generality, we study a system from $x = 0$ to $x = L$. The boundary condition is given by:

$$\Psi(z = 0) = 0 \text{ and } \Psi(z = L) = 0. \quad \text{(A.14)}$$

Applying the boundary conditions of equation A.14 to the general solution, the secular equation of the nontrivial solution of the coefficients $C_{\alpha\beta\gamma}$ leads to

$$(\lambda_1 + \lambda_2)^2 = -\frac{A_1^2}{D_+D_-}, \quad \text{(A.15)}$$

which along with equation A.15 gives the dispersion of the surface states

$$E_{\pm} = C + \frac{D_1M_0}{B_1} \pm A_2\sqrt{1 - \frac{D_1^2}{B_1^2}}k + (D_2 - B_2\frac{D_1}{B_1})k^2. \quad \text{(A.16)}$$

Near the Γ point, the dispersion shows a massless Dirac cone in k space, with the Fermi velocity $v_f = A_2/\hbar\sqrt{1 - \frac{D_1^2}{B_1^2}}$. We use Eq.A.16 and put $C = 0$, $k_z = 0$ and $k_y = 0$ to get the energy $E(k = 0, \lambda)$.

$$E(k = 0, \lambda) = \epsilon_0(\lambda) + \frac{D_1}{B_1}M_0 = \epsilon_0(\lambda) - D_1\lambda^2 + \sqrt{(M_0 + B_1\lambda^2)^2 - A_1^2\lambda^2}, \quad \text{(A.17)}$$

and with $Re(\lambda > 0)$ we get

$$A_1\lambda = (M_0 + B_1\lambda^2)\sqrt{1 - \frac{D_1^2}{B_1^2}}. \tag{A.18}$$

We now use Eq.A.17 to calculate the wave function components (u_1, u_2) and (u_3, u_4).

$$\epsilon_0(\lambda) + \begin{pmatrix} M(k) & A_1k_z \\ A_1k_z & -M(k) \end{pmatrix} \begin{pmatrix} u_1 \\ u_2 \end{pmatrix} = \frac{D_1}{B_1} M_0 \begin{pmatrix} u_1 \\ u_2 \end{pmatrix}, \tag{A.19}$$

$$\begin{pmatrix} M_0 + B_1\lambda^2 & -iA_1\lambda \\ -iA_1\lambda & -(M_0 + B_1\lambda^2) \end{pmatrix} \begin{pmatrix} u_1 \\ u_2 \end{pmatrix} = (\tfrac{D_1}{B_1} M_0 + D_1\lambda^2) \begin{pmatrix} u_1 \\ u_2 \end{pmatrix}, \tag{A.20}$$

$$\begin{pmatrix} u_1 \\ u_2 \end{pmatrix} = \frac{1}{\sqrt{2}} \begin{pmatrix} i\sqrt{1 + \frac{D_1}{B_1}} \\ -\sqrt{1 - \frac{D_1}{B_1}} \end{pmatrix}, \tag{A.21}$$

$$\epsilon_0(\lambda) + \begin{pmatrix} M(k) & -A_1k_z \\ -A_1k_z & -M(k) \end{pmatrix} \begin{pmatrix} u_3 \\ u_4 \end{pmatrix} = \frac{D_1}{B_1} M_0 \begin{pmatrix} u_3 \\ u_4 \end{pmatrix}, \tag{A.22}$$

$$\begin{pmatrix} u_3 \\ u_4 \end{pmatrix} = \frac{1}{\sqrt{2}} \begin{pmatrix} \sqrt{1 + \frac{D_1}{B_1}} \\ i\sqrt{1 - \frac{D_1}{B_1}} \end{pmatrix}. \tag{A.23}$$

. Using this vectors we now calculate the expectation values for the Spin matrices from A.4

$$\langle S_z \rangle = \begin{pmatrix} 1 & 0 \\ 0 & -1 \end{pmatrix}, \tag{A.24}$$

$$\langle S_x \rangle = \begin{pmatrix} 0 & 1 \\ 1 & 0 \end{pmatrix}, \tag{A.25}$$

$$\langle S_y \rangle = \begin{pmatrix} 0 & -i \\ i & 0 \end{pmatrix}. \tag{A.26}$$

Using the same basis we obtain the Dirac Hamiltonian for the surface states:

$$H^{2D}_{Dirac} = E(\mathbf{k}) + A_2\sqrt{1 - \frac{D_1^2}{B_1^2}} \begin{pmatrix} 0 & ik_x + k_y \\ -ik_x + k_y & 0 \end{pmatrix}. \tag{A.27}$$

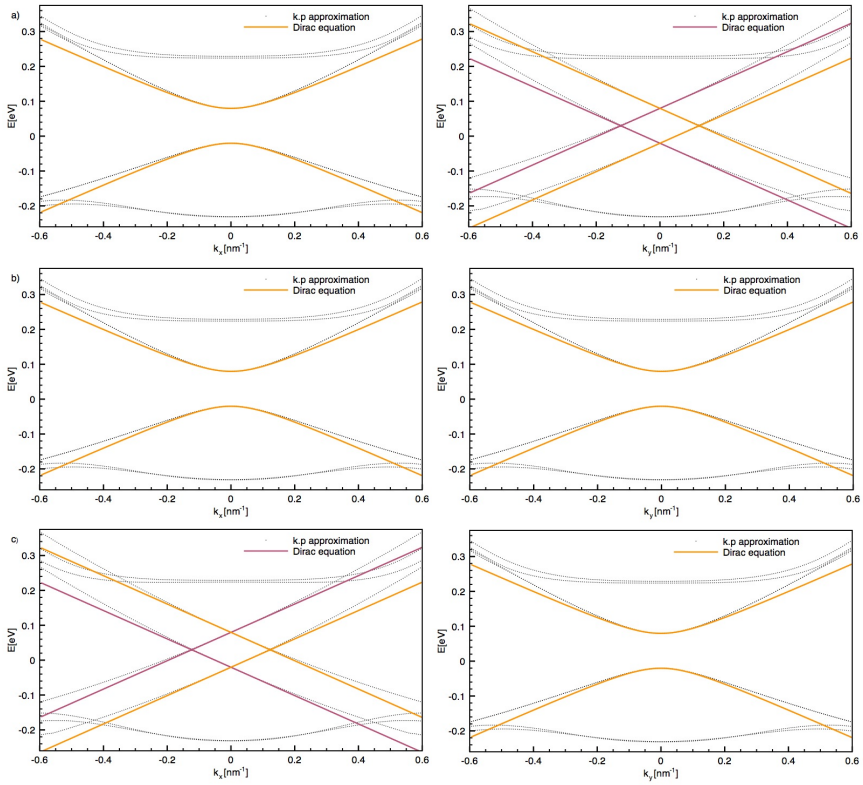

Figure A.1: (Colour online) Bandstructure for the (x, y)-surface for a) a field pointing in the x-direction, b) a field pointing in z-direction and c) a field pointing in y-direction. The doted lines describe our approximation while the coloured lines are the Dirac equation as in Eq.A.27. At the length of 10.7nm where the gap should close (see Fig. 5.5) we find that by applying an external magnetic field $\Delta \mathrm{H}_{x,y,z}$ a gap of $2\Delta \mathrm{H}_{x,y,z}$ opens at **k**=0. We also find that in a) and c) this gap closes at $\mathrm{k}_{x,y}=\pm\Delta \mathrm{H}_{y,x}$.

The difference between the (111) orientation given by Eq.(5.1) and the surface Hamiltonian Eq.A.27 can be seen in different changes.
(i)The expectation value of the σ operator is no longer perpendicular to the momentum as $p_x \rightarrow A_2 p_x$ and $p_y \rightarrow A_2 p_y$.
(ii) A particle-hole asymmetric term appears in $E(\mathbf{k})$. In the bulk states this term causes a trivial bending of both the conduction and valence bands. Including it into the Hamiltonian leads to a non-zero value for the Dirac crossing energy. Using Eq.A.24-Eq.A.27 we calculate the band structure in case of doping with magnetic impurities.

$$E^2 = (A_2\sqrt{1-\frac{D_1^2}{B_1^2}}k_y + H_x)^2 + (A_2\sqrt{1-\frac{D_1^2}{B_1^2}}k_x + H_y)^2 + H_z^2. \quad \text{(A.28)}$$

We have to shift this energy by the term $C + \frac{D_1}{B_1}M_0$=0.09 to get the same results as in Eq.A.16. According to A.28 we expect a gap to open for a field pointing in z-direction and a shift for a field in x- and y-direction. These is in agreement with the results from our calculations. The size of the gap is $2\Delta H_{x,z}$ = 1.0eV for $H_{x,z}$=0.05eV. In our calculation we get a gap of 1.0eV. The shift of the gap in the k_y-direction occurred at ± 0.12nm^{-1}. The plots with the magnetisation in y direction are also in agreement with our theoretical prediction. We obtain a gap 1.0eV as expected for $2\Delta H_y$=1eV and a shift of $\pm 0.12 nm^{-1}$ in x-direction as expected from the Dirac equation A.27.

General Solution of the surface states for the (y,z) surface

We use the four-component trial solution

$$\psi = \psi_\lambda e^{\lambda x}, \quad \text{(A.29)}$$

in the Schrödinger equation (E is the Eigenvalue of Energy)

$$\tilde{H}(k, -i\partial_x)\psi = E\psi, \quad \text{(A.30)}$$

the secular equation

$$\det|\tilde{H}(k, -i\lambda) - E| = 0, \quad \text{(A.31)}$$

gives four solutions of $\lambda(E)$, denotes as $\beta\lambda_\alpha(E)$, with $\alpha \in \{1,2\}, \beta \in \{+,-\}$ and

$$\lambda_\alpha(E) = \left[-\frac{F}{2D_+D_-} + (-1)^{\alpha-1}\frac{\sqrt{R}}{2D_+D_-}\right]^{\frac{1}{2}}. \quad \text{(A.32)}$$

where for convinience we have defined

$$\begin{gathered} F = A_2^2 + (E-L_1)D_+ + (E-L_2)D_-, \\ R = F^2 - 4D_-D_+\left[(E-L_1)(E-L_2) - A_2^2k_y^2 - A_1^2k_z^2\right] \\ D_\pm = D_2 \pm B_2 \\ L_1 = C + M_0 + (D_1 - B_1)k_z^2 + (D_2 - B_2)k_y^2 \\ L_2 = C - M_0 + (D_1 + B_1)k_z^2 + (D_2 + B_2)k_y^2. \end{gathered} \quad \text{(A.33)}$$

We use these definitions to transform the Hamiltonian in A.2 into the following version:

$$\tilde{H}^{3D} = \begin{pmatrix} L_1 - D_-\lambda^2 & A_1 k_z & 0 & -iA_2(\lambda + k_y) \\ A_1 k_z & L_2 - D_+\lambda^2 & -iA_2(\lambda + k_y) & 0 \\ 0 & -iA_2(\lambda - k_y) & L_1 - D_-\lambda^2 & -A_1 k_z \\ -iA_2(\lambda - k_y) & 0 & -A_1 k_z & L_2 - D_+\lambda^2 \end{pmatrix}. \quad \text{(A.34)}$$

The Eigenvalues are doubly degenerated and given by

$$E_\pm = \tfrac{1}{2}(L_1 + L_2 - (D_+ + D_-)\lambda^2) \pm \sqrt{4A_1^2k_z^2 + 4A_2(k_y^2 - \lambda^2) + (L_1 + L_2 - (D_+ + D_-)\lambda^2)^2 + 4(D_+L_1\lambda^2 + D_-L_2\lambda^2 - D_+D_-\lambda^4)}. \quad \text{(A.35)}$$

Because of double degeneracy, each of the four $\beta\lambda_\alpha(E)$ corresponds to two linearly independent four-component vectors, found to be

$$\Psi_{\alpha\beta 1} = \begin{pmatrix} E_\pm - L_2 + D_+\lambda_\alpha^2 \\ A_1 k_z \\ 0 \\ iA_2(\lambda_\alpha - k_y) \end{pmatrix}, \quad \text{(A.36)}$$

$$\Psi_{\alpha\beta 2} = \begin{pmatrix} A_1 k_z \\ E_\pm - L_1 + D_-\lambda_\alpha^2 \\ iA_2(\lambda_\alpha - k_y) \\ 0 \end{pmatrix}. \quad \text{(A.37)}$$

Finite Boundary Conditions

The surface states have a finite distribution near the boundary. For a film thick enough that the states at opposite surfaces barely couple to each other, we can focus just one surface. Without loss of generality, we study a system from x=0 to x=L. The boundary conditions is given by:

$$\Psi(x = 0) = 0 \text{ and } \Psi(x = L) = 0. \quad \text{(A.38)}$$

Applying the boundary conditions of equation A.38 to the general solution, the secular equation of the nontrivial solution to the coefficients $C_{\alpha\beta\gamma}$ leads to

$$(\lambda_1 + \lambda_2)^2 = -\frac{A_2^2}{D_+D_-}, \quad \text{(A.39)}$$

which along with equation A.35 gives the dispersion of the surface states

$$E_\pm = C + \frac{D_2M_0}{B_2} \pm A_1\sqrt{\frac{A_2^2}{A_1^2}k_y^2 + k_z^2}\sqrt{1 - \frac{D_2^2}{B_2^2}} + (D_1 - B_1\frac{D_2}{B_2})k_z^2. \quad \text{(A.40)}$$

Near the Γ point, the dispersion shows a massless Dirac cone in k space, with the Fermi velocity $v_f = A_1/\hbar\sqrt{1-\frac{D_2^2}{B_2^2}}$. We use and put $C = 0$, $k_z = 0$ and $k_y = 0$ to get the energy $E(k = 0, \lambda)$.

$$E(k=0,\lambda) = \epsilon_0(\lambda) + \tfrac{D_2}{B_2}M_0 = \epsilon_0(\lambda) - D_2\lambda^2 + \sqrt{(M_0 + B_2\lambda^2)^2 - A_2^2\lambda^2}. \quad \text{(A.41)}$$

$Re(\lambda > 0)$

$$A_2\lambda = (M_0 + B_2\lambda^2)\sqrt{1-\frac{D_2^2}{B_2^2}}. \quad \text{(A.42)}$$

We now use Eq.A.41 to calculate the wave function components (u_1, u_4) and (u_2, u_3).

$$\epsilon_0(\lambda) + \begin{pmatrix} M(k) & A_2k_x \\ A_2k_x & -M(k) \end{pmatrix}\begin{pmatrix} u_1 \\ u_4 \end{pmatrix} = \frac{D_2}{B_2}M_0\begin{pmatrix} u_1 \\ u_4 \end{pmatrix}, \quad \text{(A.43)}$$

$$\begin{pmatrix} M_0 + B_2\lambda^2 & -iA_2\lambda \\ -iA_2\lambda & -(M_0 + B_2\lambda^2) \end{pmatrix}\begin{pmatrix} u_1 \\ u_4 \end{pmatrix} = (\tfrac{D_2}{B_2}M_0 + D_2\lambda^2)\begin{pmatrix} u_1 \\ u_4 \end{pmatrix}, \quad \text{(A.44)}$$

$$\begin{pmatrix} u_1 \\ u_4 \end{pmatrix} = \frac{1}{\sqrt{2}}\begin{pmatrix} \sqrt{1+\frac{D_2}{B_2}} \\ i\sqrt{1-\frac{D_2}{B_2}} \end{pmatrix}, \quad \text{(A.45)}$$

$$\epsilon_0(\lambda) + \begin{pmatrix} -M(k) & A_2k_x \\ A_2k_x & M(k) \end{pmatrix}\begin{pmatrix} u_2 \\ u_3 \end{pmatrix} = \frac{D_2}{B_2}M_0\begin{pmatrix} u_2 \\ u_3 \end{pmatrix}, \quad \text{(A.46)}$$

$$\begin{pmatrix} u_2 \\ u_3 \end{pmatrix} = \frac{1}{\sqrt{2}}\begin{pmatrix} i\sqrt{1-\frac{D_2}{B_2}} \\ \sqrt{1+\frac{D_2}{B_2}} \end{pmatrix}. \quad \text{(A.47)}$$

Using this vectors we now calculate the expectation values for the Spin matrices from A.4

$$\langle S_z\rangle = \begin{pmatrix} \frac{D_2}{B_2} & 0 \\ 0 & -\frac{D_2}{B_2} \end{pmatrix}, \quad \text{(A.48)}$$

$$\langle S_x\rangle = \begin{pmatrix} 0 & \frac{D_2}{B_2} \\ \frac{D_2}{B_2} & 0 \end{pmatrix}, \quad \text{(A.49)}$$

$$\langle S_y\rangle = \begin{pmatrix} 0 & -i \\ i & 0 \end{pmatrix}. \quad \text{(A.50)}$$

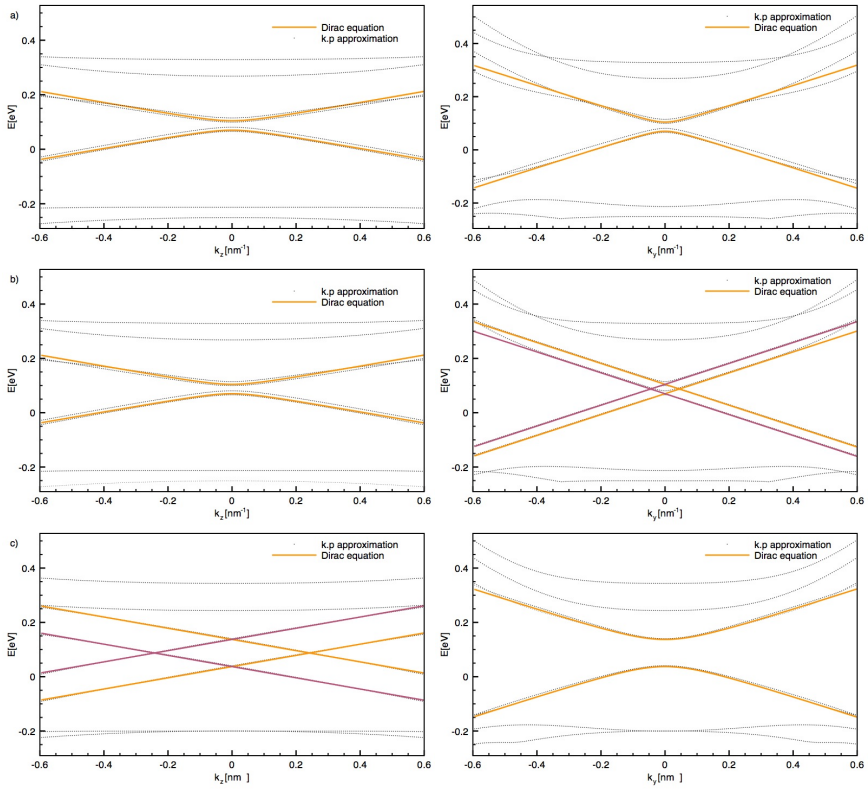

Figure A.2: (Colour online) Band structure for the (z, y)-surface for a system of L=10.7nm and a) a field pointing in the x-direction, b) a field pointing in z-direction and c) a field pointing in y-direction. The doted lines describe our approximation while the solid lines are the Dirac equation as in Eq.A.52.

Using the same basis we obtain the Dirac Hamiltonian for the surface states:

$$H^{2D}_{Dirac} = E(\mathbf{k}) + \sqrt{1 - \frac{D_2^2}{B_2^2}} \begin{pmatrix} A_2 k_y & iA_1 k_z \\ -iA_1 k_z & -A_2 k_y \end{pmatrix}. \tag{A.51}$$

Using (Eqs. A.48-A.51) we calculate the band structure in case of doping with magnetic impurities.

$$E^2 = (\sqrt{1 - \frac{D_2^2}{B_2^2}} A_2 k_y - \frac{D_2}{B_2} H_z)^2 + (\sqrt{1 - \frac{D_2^2}{B_2^2}} A_1 k_z - H_y)^2 - \frac{D_2^2}{B_2^2} H_x^2. \tag{A.52}$$

We have to shift this energy by the term $C + \frac{D_2}{B_2} M_0$=0.09 to get the same results as in Eq.A.40 for $\mathbf{k}$=0.According to Eq.A.52 we expect a gap to

open for a field pointing in x-direction and a shift for a field in y- and z-direction. These is in agreement with the results from our calculations. The size of the gap is reduced by the quantity $\frac{D_2}{B_2}$ and is now $2\frac{D_2}{B_2}\Delta H_{x,z}$ = 0.03463eV for $H_{x,z}$=0.05. The shift occurred at k_y=$\pm$0.048nm^{-1}. In z-direction the shift happens at $\pm 0.24nm^{-1}$ for a field in y-direction. Here the gap size is not reduced as the expectation value for the Spin Matrix in y-direction doesn't change from the value for the (x, y)-surface.
Comparing the case of the (111) orientation of the surface with those of the anisotropic case we find that a few things have changed.
(i) For the anisotropic Hamiltonian the expectation value of the σ operator is no longer perpendicular to the momentum. $p_x \rightarrow A_2 p_x$ and $p_z \rightarrow A_1 p_z$.
(ii) The appearance of a particle-hole asymmetric term in $E(k)$. In the bulk states this term causes a trivial bending of both the valence and conduction bands. Including it into the Hamiltonian leads to a non-zero value for the Dirac crossing energy.
(iii)At the length of 10.7nm where the gap should close (see Fig. 5.5) we find that by applying an external magnetic field $\Delta H_{x,y,z}$ a gap of $2\frac{D_2}{B_2}\Delta H_{x,z}$ and $2\Delta H_y$ opens at **k**=0. We also find a shift in the band structure so that in b) this gap closes at k_y=$\pm\frac{D_2}{B_2}\Delta H_z$ and in c) it closes at k_z=$\pm\Delta H_y$.
Dirac crossing for Bi_2Se_3 can vary by:

$$\Delta_{E_{Dirac}} = \left(\frac{D_2}{B_2} - \frac{D_1}{B_1}\right) M_0 = 0.6eV. \tag{A.53}$$

In conclusion it can be said that the inequivalence of the spin variables on the Bi and Se sublattices leads to a nontrivial spin structure of the surface states at surfaces other than the (111) surface. The energy of the Dirac crossing in the surface state dispersion depends on the surface state orientation.
These results may change with different boundary conditions.

General Solution of the surface states for the (x,z) surface

We use the four-component trial solution

$$\psi = \psi_\lambda e^{\lambda y}, \tag{A.54}$$

in the Schrödinger equation (E is the Eigenvalue of Energy)

$$\tilde{H}(k, -i\partial_y)\psi = E\psi, \tag{A.55}$$

the secular equation

$$\det|\tilde{H}(k,-i\lambda)-E|=0, \tag{A.56}$$

gives four solutions of $\lambda(E)$, denotes as $\beta\lambda_\alpha(E)$, with $\alpha\in\{1,2\},\beta\in\{+,-\}$ and

$$\lambda_\alpha(E)=\left[-\frac{F}{2D_+D_-}+(-1)^{\alpha-1}\frac{\sqrt{R}}{2D_+D_-}\right]^{\frac{1}{2}}. \tag{A.57}$$

where for convinience we have defined

$$\begin{gathered}F=A_2^2+(E-L_1)D_++(E-L_2)D_-,\\ R=F^2-4D_-D_+\left[(E-L_1)(E-L_2)-A_2^2k_x^2-A_1^2k_z^2\right]\\ D_\pm=D_2\pm B_2\\ L_1=C+M_0+(D_1-B_1)k_z^2+(D_2-B_2)k_x^2\\ L_2=C-M_0+(D_1+B_1)k_z^2+(D_2+B_2)k_x^2.\end{gathered} \tag{A.58}$$

We use these definitions to transform the Hamiltonian in A.2 into the following version:

$$\tilde{H}^{3D}=\begin{pmatrix}L_1-D_-\lambda^2 & A_1k_z & 0 & A_2(k_x-\lambda)\\ A_1k_z & L_2-D_+\lambda^2 & A_2(k_x-\lambda) & 0\\ 0 & A_2(k_x+\lambda) & L_1-D_-\lambda^2 & -A_1k_z\\ A_2(k_x-\lambda) & 0 & -A_1k_z & L_2-D_+\lambda^2\end{pmatrix}. \tag{A.59}$$

The Eigenvalues are doubly degenerated and given by

$$E_\pm=\tfrac{1}{2}(L_1+L_2-(D_++D_-)\lambda^2)\pm \sqrt{4A_1^2k_z^2+4A_2(k_x^2+\lambda^2)+(L_1+L_2-(D_++D_-)\lambda^2)^2+4((D_+L_1+D_-L_2)\lambda^2-D_+D_-\lambda^4)}. \tag{A.60}$$

Because of double degeneracy, each of the four $\beta\lambda_\alpha(E)$ corresponds to two linearly independent four-component vectors, found to be

$$\Psi_{\alpha\beta1}=\begin{pmatrix}E_\pm-L_2+D_+\lambda_\alpha^2\\ A_1k_z\\ 0\\ A_2(\lambda_\alpha+k_x)\end{pmatrix}, \tag{A.61}$$

$$\Psi_{\alpha\beta2}=\begin{pmatrix}A_1k_z\\ E_\pm-L_1+D_-\lambda_\alpha^2\\ A_2(\lambda_\alpha+k_x)\\ 0\end{pmatrix}. \tag{A.62}$$

Finite Boundary Conditions

The surface states have a finite distribution near the boundary. For a film thick enough that the states at opposite surfaces barely couple to each other, we can focus just one surface. Without loss of generality, we study a system from x=0 to x=L. The boundary conditions is given by:

$$\Psi(x=0)=0 \text{ and } \Psi(x=L)=0. \tag{A.63}$$

Applying the boundary conditions of equation A.63 to the general solution, the secular equation of the nontrivial solution to the coefficients $C_{\alpha\beta\gamma}$ leads to

$$(\lambda_1+\lambda_2)^2=-\frac{A_2^2}{D_+D_-}, \tag{A.64}$$

which along with equation A.60 gives the dispersion of the surface states

$$E_\pm=C+\frac{D_2M_0}{B_2}\pm A_1\sqrt{\frac{A_2^2}{A_1^2}k_x^2+k_z^2}\sqrt{1-\frac{D_2^2}{B_2^2}}+(D_1-B_1\frac{D_2}{B_2})k_z^2. \tag{A.65}$$

Near the Γ point, the dispersion shows a massless Dirac cone in k space, with the Fermi velocity $v_f=A_1/\hbar\sqrt{1-\frac{D_2^2}{B_2^2}}$. We use Eq.A.65 and put $C=0$, $k_z=0$ and $k_y=0$ to get the energy $E(k=0,\lambda)$.

$$E(k=0,\lambda)=\epsilon_0(\lambda)+\tfrac{D_2}{B_2}M_0=\epsilon_0(\lambda)-D_2\lambda^2+\sqrt{(M_0+B_2\lambda^2)^2-A_2^2\lambda^2}, \tag{A.66}$$

$Re(\lambda>0)$

$$A_2\lambda=(M_0+B_2\lambda^2)\sqrt{1-\frac{D_2^2}{B_2^2}}. \tag{A.67}$$

We now use Eq.A.66 to calculate the wave function components (u_1,u_4) and (u_2,u_3).

$$\epsilon_0(\lambda)+\begin{pmatrix} M(k) & -A_2k_y \\ A_2k_y & -M(k)\end{pmatrix}\begin{pmatrix}u_1\\u_4\end{pmatrix}=\frac{D_2}{B_2}M_0\begin{pmatrix}u_1\\u_4\end{pmatrix}, \tag{A.68}$$

$$\begin{pmatrix} M_0+B_2\lambda^2 & iA_2\lambda \\ -iA_2\lambda & -(M_0+B_2\lambda^2)\end{pmatrix}\begin{pmatrix}u_1\\u_4\end{pmatrix}=(\tfrac{D_2}{B_2}M_0+D_2\lambda^2)\begin{pmatrix}u_1\\u_4\end{pmatrix}, \tag{A.69}$$

$$\begin{pmatrix}u_1\\u_4\end{pmatrix}=\frac{1}{\sqrt{2}}\begin{pmatrix}-\sqrt{1+\frac{D_2}{B_2}}\\ \sqrt{1-\frac{D_2}{B_2}}\end{pmatrix}, \tag{A.70}$$

$$\epsilon_0(\lambda) + \begin{pmatrix} -M(k) & -A_2 k_y \\ A_2 k_y & M(k) \end{pmatrix} \begin{pmatrix} u_2 \\ u_3 \end{pmatrix} = \frac{D_2}{B_2} M_0 \begin{pmatrix} u_2 \\ u_3 \end{pmatrix}, \tag{A.71}$$

$$\begin{pmatrix} u_2 \\ u_3 \end{pmatrix} = \frac{1}{\sqrt{2}} \begin{pmatrix} \sqrt{1 - \frac{D_2}{B_2}} \\ \sqrt{1 + \frac{D_2}{B_2}} \end{pmatrix}. \tag{A.72}$$

Using this vectors we now calculate the expectation values for the Spin matrices from Eq.A.4

$$\langle S_z \rangle = \begin{pmatrix} \frac{D_2}{B_2} & 0 \\ 0 & -\frac{D_2}{B_2} \end{pmatrix}, \tag{A.73}$$

$$\langle S_x \rangle = \begin{pmatrix} 0 & \frac{D_2}{B_2} \\ \frac{D_2}{B_2} & 0 \end{pmatrix}, \tag{A.74}$$

$$\langle S_y \rangle = \begin{pmatrix} 0 & -i \\ i & 0 \end{pmatrix}. \tag{A.75}$$

Using the same basis we obtain the Dirac Hamiltonian for the surface states:

$$H^{2D}_{Dirac} = E(\mathbf{k}) + \sqrt{1 - \frac{D_2^2}{B_2^2}} \begin{pmatrix} -A_2 k_x & -iA_1 k_z \\ -iA_1 k_z & A_2 k_x \end{pmatrix}. \tag{A.76}$$

Using (Eqs. A.73-A.76) we calculate the band structure in case of doping with magnetic impurities.

$$E^2 = (\sqrt{1 - \frac{D_2^2}{B_2^2}} A_2 k_y - \frac{D_2}{B_2} H_z)^2 + (\sqrt{1 - \frac{D_2^2}{B_2^2}} A_1 k_z - H_x)^2 - \frac{D_2^2}{B_2^2} H_y^2. \tag{A.77}$$

We have to shift this energy by the term $C + \frac{D_2}{B_2} M_0$=0.09 to get the same results as in Eq. A.65. According to Eq. A.77 we expect a gap to open for a field pointing in x-direction and a shift for a field in y- and z-direction. These is in agreement with the results from our calculations. The size of the gap is reduced by the quantity $\frac{D_2}{B_2}$ and is now $2\frac{D_2}{B_2}\Delta H_{x,z}$ = 0.03463eV for $H_{x,z}$=0.05. In our calculation we get a gap of 0.03427eV. The shift occurred at k_x=$\pm$0.048nm^{-1} for a field pointing in z-direction. In z-direction the shift happens at $\pm 0.24 nm^{-1}$ for a field in x-direction. Here the gap size is not reduced as the expectation value for the Spin Matrix in x-direction doesn't change from the value for the (x, y)-surface.
Comparing the case of the (111) orientation of the surface with those of

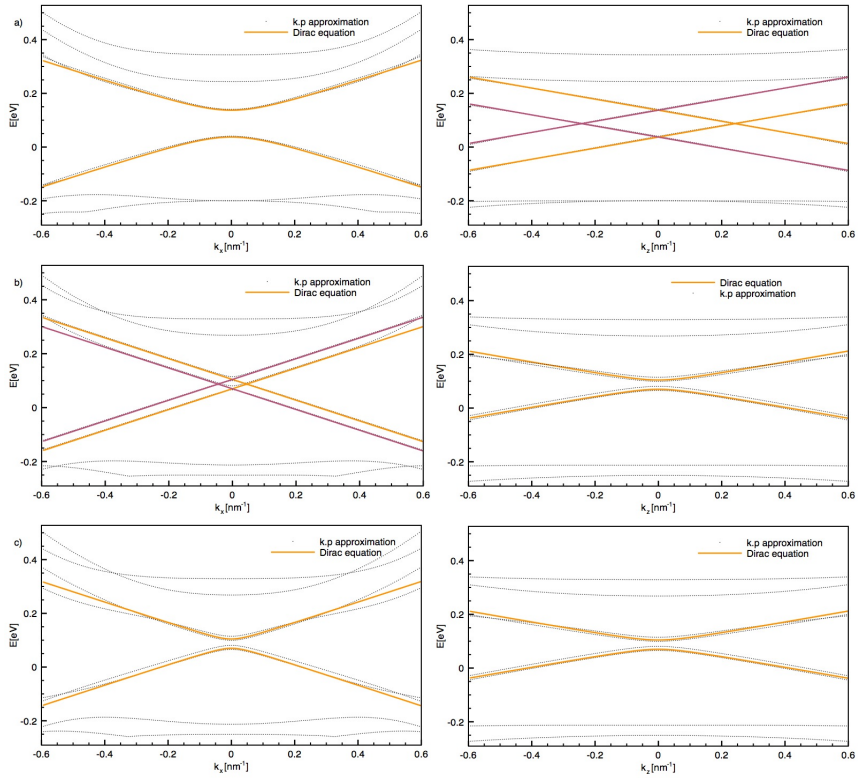

Figure A.3: (Colour online) Bandstructure for the (x, z)-surface for a) a field pointing in the x-direction, b) a field pointing in z-direction and c) a field pointing in y-direction. The doted lines describe our approximation while the coloured lines are the Dirac equation as in Eq. A.77.

the anisotropic case we find that a few things have changed.
(i) For the anisotropic Hamiltonian the expectation value of the σ operator is no longer perpendicular to the momentum. $p_y \rightarrow A_2 p_y$ and $p_z \rightarrow A_1 p_z$.
(ii) The appearance of a particle-hole asymmetric term in $E(k)$. In the bulk states this term causes a trivial bending of both the valence and conduction bands. Including it into the Hamiltonian leads to a non-zero value for the Dirac crossing energy.
(iii)At the length of 10.7nm where the gap should close (see Fig. B.2) we find that by applying an external magnetic field $\Delta \mathrm{H}_{x,y,z}$ a gap of $2\Delta \mathrm{H}_{x,y,z}$ opens at $\mathbf{k}$=0. We also find that in a) this gap closes at $\mathrm{k}_z = \pm \Delta \mathrm{H}_x$ and in c) at $\mathrm{k}_x = \pm \Delta \mathrm{H}_z$.

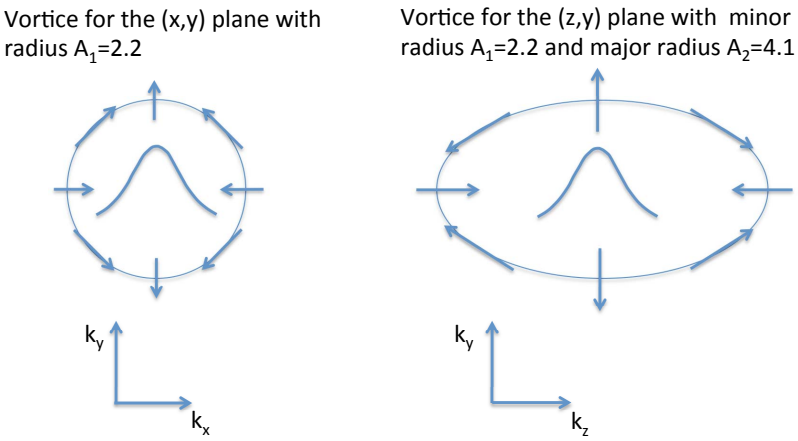

Figure A.4: (Colour online) These are vortices for the (x,y) plane on the left side and for the (z,y) plane on the right side. The first one is symmetric and in the form of a circle of radius A_1 and the second one is an ellipse with the semi-axes given by A_1 and A_2. By replacing y with x in the right figure it would give the vortex for the (x,z)-surface.

The Dirac crossing for Bi_2Se_3 can vary by:

$$\Delta_{E_{Dirac}} = \left(\frac{D_2}{B_2} - \frac{D_1}{B_1}\right) M_0 = 0.6eV. \tag{A.78}$$

In conclusion it can be said that the inequivalence of the spin variables on the Bi and Se sublattices leads to a nontrivial spin structure of the surface states at surfaces other than the (111) surface. The energy of the Dirac crossing in the surface state dispersion depends on the surface state orientation.
These results may change with different boundary conditions.

APPENDIX B

Oscillatory crossover from two-dimensional to three-dimensional topological insulators

In this chapter we study the crossover from three-dimensional TI Bi_2Se_3 to two-dimensional TI by reducing the layer thickness. This work is similar to the work of Liu *e*t al.[53] where they investigate the crossover regime from three-dimensional topological insulators Bi_2Te_3 and Bi_2Se_3 to two-dimensional topological insulators with quantum spin Hall effect when the layer thickness is reduced. Their and our results show that the crossover happens in an oscillatory fashion, changing between topological trivial and non-trivial state.

Comparing the Hamiltonian in Eq.A.2 but with $A_1 = 0$ we see that it is identical to the two-dimensional Hamiltonian given by Zhou et al. Therefore we expect to be able to go from three dimensions to two dimension by reducing the thickness of the TI in Eq.A.2.
Starting from the three-dimensional low-energy effective Hamiltonian for Bi_2Se_3 given by Eq.A.2 we want to solve the Eigenvalue problem. We can write an Ansatz for the wave functions in the following way:

$$\Psi_{nk}(z) = \frac{e^{ikr}}{\sqrt{A}}\sqrt{\frac{2}{L}}\sum_{l=1}^{N_{max}}\sum_{j=1,4} a^l_{n,j}(k) sin\left(l\pi\frac{z}{L}\right), \tag{B.1}$$

where A is the sample volume and N_{max} is the number of harmonics

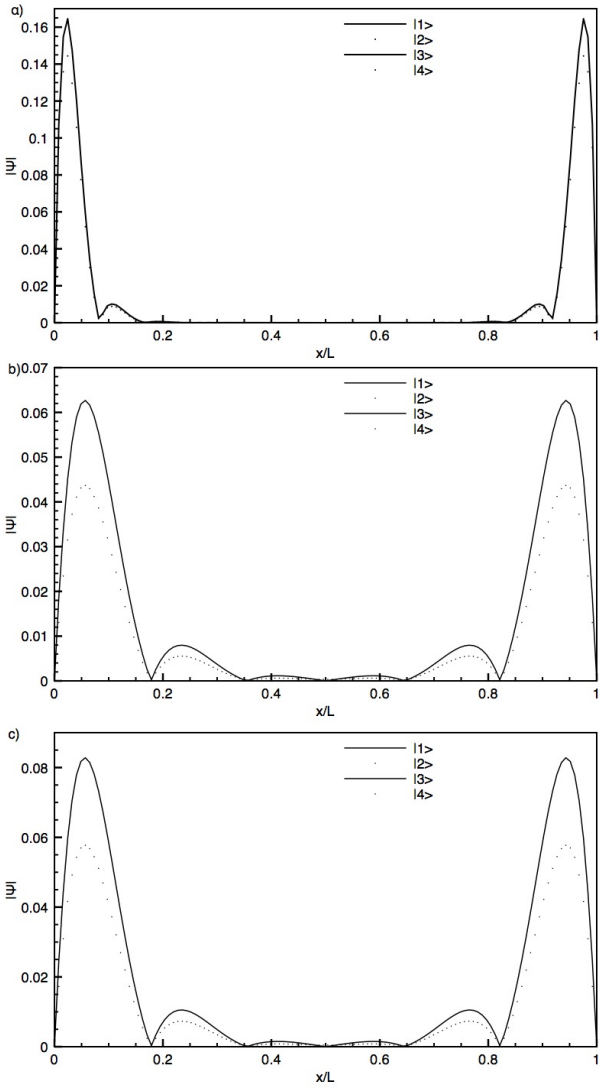

Figure B.1: Absolute value of the wave function, as a function of the position along the slab. The slab thickness is 30nm and the momentum is close to zero. In a) we plot it for the case of a surface oriented in the (x, y)-plane, in b) it is for the (y, z)-plane and in c) for the (x, z)-plane.

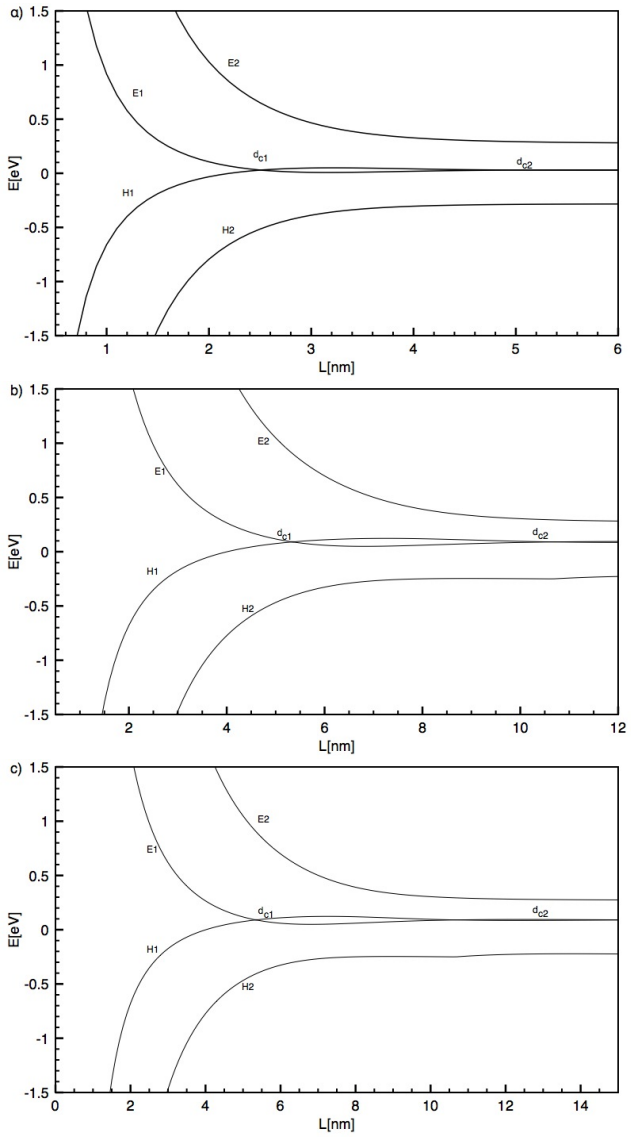

Figure B.2: Energy levels versus layer thickness for a slab of length 10nm. At critical thickness there is a crossing from the trivial to the non-trivial insulator regime. This crossing happens in an oscillatory fashion and repeats itself at integer multitudes of the critical thickness d_{cn}.

used in the expansion.
Next we calculate the Eigenvalues numerically as a function of the layer thickness for the last two valence-bands and the first two conduction bands. We find that the material is in a trivial insulator state but has crossing points at critical thickness d_{cn} where it goes over into a non-trivial insulator state. This crossing happens in an oscillatory fashion at critical thickness. We find that the crossing points appear whenever $\frac{l}{L}$ is an integer. Our results are in agreement with those of Liu *e*t al. [53].

APPENDIX C

Supplementary material for the interface Vacuum-Multiferroic.

Ansatz for an interface Vacuum - Multiferroic

In this supplementary material we describe in detail how we solved the constituent equations for an interface vacuum-MF. To solve these equations for a point charge in vacuum inside of a mutliferroic we match the fields at the surface ($r = a_0$). We start with the ansatz and the boundary conditions: There are no free charges or monopoles in both regions. A possible model for an interface vacuum-MF is given in Figure C.1.

$$\begin{aligned} \mathbf{E} &= -\nabla\phi^e, \\ \nabla^2\phi^e &= 0, \end{aligned} \tag{C.1}$$

$$\begin{aligned} \mathbf{B} &= -\nabla\phi^m, \\ \nabla^2\phi^m &= 0. \end{aligned} \tag{C.2}$$

Satisfying the Laplace equation the potentials for the fields can be written using Legendre polynomials, where we assume invariance in ϕ:

$$\phi^{e,m} = \sum_l \left(\alpha_l^{e,m} r^l + \beta_l^{e,m} \frac{1}{r^{l+1}} \right) P_l(cos\theta). \tag{C.3}$$

The boundary conditions for an interface are given using the normal **n** and tangential **t** components of the fields by:

$$\begin{aligned} \mathbf{D}_1\mathbf{n} &= \mathbf{D}_2\mathbf{n}, \\ \mathbf{E}_1\mathbf{t} &= \mathbf{E}_2\mathbf{t}, \\ \mathbf{B}_1\mathbf{n} &= \mathbf{B}_2\mathbf{n}, \\ \mathbf{H}_1\mathbf{t} &= \mathbf{H}_2\mathbf{t}. \end{aligned} \tag{C.4}$$

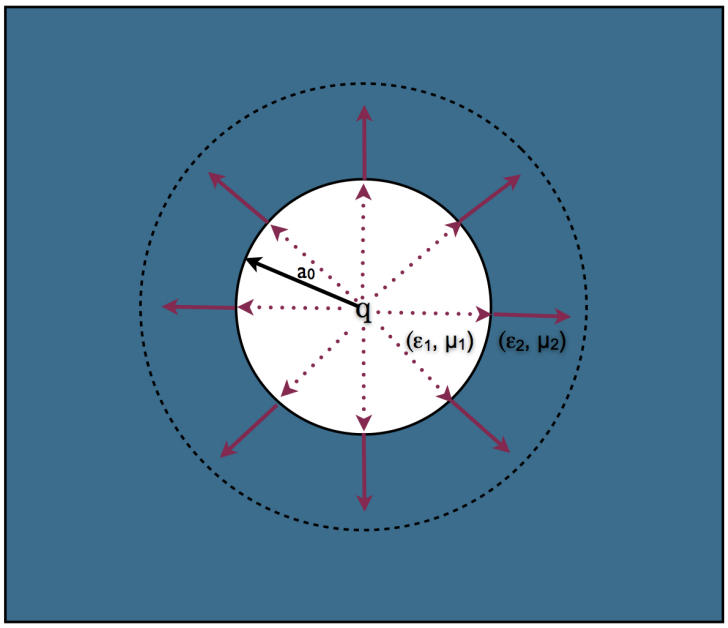

Figure C.1: Model of a charge sitting in the centre of a spherical interface vacuum/MF of radius a_0 with (ϵ_1, μ_1) surrounded by a multiferroic with (ϵ_2, μ_2). The charge in the center induces a magnetic flux in the mutliferroic.

The boundary conditions (C.4) using Legendre polynomials turn into:

$$\epsilon_1 \frac{\partial \phi_1^e}{\partial r} = \epsilon_2 \frac{\partial \phi_2^e}{\partial r} - 2\alpha P_3 \frac{\partial \phi_2^m}{\partial r}, \tag{C.5}$$

$$\frac{\partial \phi_1^e}{\partial \theta} = \frac{\partial \phi_2^e}{\partial \theta}, \tag{C.6}$$

$$\frac{1}{\mu_1} \frac{\partial \phi_1^m}{\partial \theta} = \frac{1}{\mu_2} \frac{\partial \phi_2^m}{\partial \theta} + 2\alpha P_3 \frac{\partial \phi_2^e}{\partial \theta}, \tag{C.7}$$

$$\frac{\partial \phi_1^m}{\partial r} = \frac{\partial \phi_2^m}{\partial r}. \tag{C.8}$$

Model

Inside the sphere (see Fig.C.1) we write the potentials as a sum of the Coulomb potential of a point charge and the electrostatic potential of the

material (ϵ_1, μ_1):

$$\phi_1^e = \frac{q}{\epsilon_1} \sum_l \frac{1}{r^{l+1}} P_l(\cos\theta) + \sum_l \left(\frac{r}{a_0}\right)^l \alpha_l P_l(\cos\theta). \tag{C.9}$$

The same goes for the magnetic potential:

$$\phi_1^m = \sum_l \left(\frac{r}{a_0}\right)^{l+1} \delta_l P_l(\cos\theta). \tag{C.10}$$

In the region outside the sphere we note that the electric (e) and magnetic (m) potentials can be written in Legendre polynomials and have the following form:

$$\phi_2^e = \sum_l \left(\frac{a_0}{r}\right)^{l+1} \gamma_l P_l(\cos\theta), \tag{C.11}$$

$$\phi_2^m = \sum_l G_l \frac{1}{r^{l+1}} P_l(\cos\theta) + \sum_l \left(\frac{a_0}{r}\right)^l \beta_l P_l(\cos\theta). \tag{C.12}$$

Results for the coefficients

In the following we are giving an example on how to calculate the coefficients for the wave functions.
Using the boundary conditions C.5 to C.8 and C.9 to C.12 we can write down the coefficients:

$$\alpha_l = -\frac{q}{\epsilon_1} \frac{1}{a_0^{l+1}} + \gamma_l, \tag{C.13}$$

$$\beta_l = \left(\frac{G_l}{a_0^{l+1}} - \delta_l\right) \frac{l+1}{l}, \tag{C.14}$$

$$\gamma_l = -\frac{1}{a^{l+1}} \frac{\left(q\frac{2l+1}{l+1} + G_l\left(1 + \lambda + \frac{\frac{1}{\mu_2}\left(\frac{l}{l+1}-1\right)}{\frac{l}{l+1}\frac{1}{\mu_1}+\frac{1}{\mu_2}}\right)\right)}{\lambda\frac{l}{l+1}\left(\frac{l}{l+1}\frac{1}{\mu_1}+\frac{1}{\mu_2}\right) - \left(\epsilon_2 + \epsilon_1\frac{l}{l+1}\right)}, \tag{C.15}$$

$$\delta_l = \frac{\frac{G_l}{a^{l+1}}\frac{1}{\mu_2}\left(\frac{l}{l+1}-1\right) + \frac{\lambda l}{l+1}\gamma_l}{\frac{1}{\mu_2}+\frac{1}{\mu_1}\frac{l}{l+1}}. \tag{C.16}$$

Using spherical symmetry we can ignore all the terms of l except $l = 0$, $\lambda = \kappa a$ and we write $G_0 = g$. The coefficients now become:

$$\delta_0 = -\frac{g}{a_0}, \tag{C.17}$$

$$\gamma_0 = \frac{1}{\epsilon_2}\left(\lambda\delta_0 + \frac{q}{a_0}\right) = \frac{1}{\epsilon_2 a_0}(\lambda g + q), \tag{C.18}$$

$$\alpha_0 = -q\frac{1}{\epsilon_1 a_0} + \gamma_0 = \frac{q}{a_0}\left(\frac{1}{\epsilon_2} - \frac{1}{\epsilon_1}\right) + g\frac{1}{\epsilon_2}\frac{\lambda}{a_0}. \tag{C.19}$$

Results for the fields $l = 0$

We find the equations for the electric and magnetic potentials inside (in) and outside (out) the spherical vaccuum

$$\phi^e_{in} = \frac{q}{\epsilon_1}\frac{1}{r} + \frac{1}{a_0\epsilon_2}(q + \lambda g) - q\frac{1}{\epsilon_1 a_0}, \tag{C.20}$$

$$\phi^e_{out} = \frac{q + \lambda g}{r\epsilon_2}, \tag{C.21}$$

$$\phi^m_{in} = -\frac{g}{a_0^2}r + \frac{2g}{a_0}, \tag{C.22}$$

$$\phi^m_{out} = \frac{g}{r}. \tag{C.23}$$

Time-dependence for $\vec{M}$ and $\vec{P}$

To derive the time-dependencies for $\vec{M}$ and $\vec{P}$ we use perturbations of first order for $\vec{M}$ and $\vec{P}$ and neglect time derivatives of spacial changes in both functions.

$$(\nabla\mathbf{M})^2 = \sum_{i,j}\partial_i M_j \partial_i M_j, \tag{C.24}$$

$$\delta(\nabla\mathbf{M})^2 = \sum_{ij}\partial_i(M + \delta M)_j \partial_i(M + \delta M)_j, \tag{C.25}$$

$$\nabla_i\delta M_j\nabla_i M_j + \nabla_i M_j\nabla_i\delta M_j = \nabla_i(\delta M_j\nabla_i M_i) - \delta M_j\nabla_i^2 M_j, \tag{C.26}$$

$$\underbrace{\nabla_i(\delta M_j\nabla_i M_i)}_{\to 0} - \delta M_j\nabla_i^2 M_j, \tag{C.27}$$

$$\frac{\delta}{\delta M_j}(\nabla\mathbf{M})^2 = -\sum_{i,j}\nabla_i^2 M_j, \tag{C.28}$$

$$(\partial_t\mathbf{M})^2 = \sum_{i,j}\partial_t M_j \partial_t M_j, \tag{C.29}$$

$$(\partial_t\mathbf{M})^2 = \sum_{j}\partial_t(M(t) + \delta M(t))_j \partial_t(M(t) + \delta M(t))_j, \tag{C.30}$$

$$\partial_t \delta M_j \partial_t M_j + \partial_t M_j \partial_t \delta M_j = \partial_t (\delta M_j \partial_t M_i) - \delta M_j \partial_t^2 M_j, \tag{C.31}$$

$$\underbrace{\partial_t (\delta M_j \partial_t M_i)}_{\to 0} - \delta M_j \partial_t^2 M_j, \tag{C.32}$$

$$\frac{\delta}{\delta M_j} (\partial_t \mathbf{M})^2 = -\sum_j \partial_t^2 M_j, \tag{C.33}$$

Solutions for $\vec{M}$ and $\vec{P}$

Solving Eq.3.18 gives the following expression:

$$(\chi_m - \rho_m |\mathbf{k}|^2 + \pi_m \omega^2)(\chi_p - \rho_p |\mathbf{k}|^2 + \pi_p \omega^2) - \kappa^2 = 0. \tag{C.34}$$

Bibliography

[1] M.Z. Hasan and C.L. Kane, Rev. Mod. Phys. **82**, 3045 (2010).

[2] NDT Resource Centre, `http://www.ndt-ed.org/EducationResources/CommunityCollege/MagParticle/Physics/Measuring.htm`.

[3] K. von Klitzing, G. Dorda, and M. Pepper, Phys. Rev. Lett. **45**, 494 (1980).

[4] Tsuneya Ando, Yukio Matsumoto, and Yasutada Uemura, J. Phys. Soc. Jpn. **39** (1975)

[5] D. J. Thouless, M. Kohmoto, M. P. Nightingale, and M. den Nijs, Phys. Rev. Lett. **49**, 405 (1982).

[6] M. Sitte, Quantum Hall Effect and Surface Criticality in 3D Topological Insulators.

[7] F. D. M. Haldane, Phys. Rev. Lett. **61**, 2015 (1988).

[8] C. L. Kane and E. J. Mele, Phys. Rev. Lett. **95**, 226801 (2005).

[9] M. König *e*t al., J. Phys. Soc. Jpn.**77** (2008).

[10] X. Qi and S.-C. Zhang, Physics Today **63(1)**, 33 (2010);

[11] S. Murakami, N. Nagaosa and S.-C.Zhang, Phys. Rev. Let. **93**, 156804 (2005).

[12] J. Sinova *e*t al., Phys. Rev. Let. **92**, 126603 (2004).

[13] C. L. Kane and E. J. Mele, Phys. Rev. Lett. **95**, 146802 (2005).

[14] C.Wu, Bernevig, S.-C. Zhang, Phys. Rev. Lett. **96**,106401 (2006).

[15] S. Murakami et al., Science **301**, 1348 (2003).

[16] M. König *e*t al. Science **318**, 766 (2007).

[17] B. Büttner *e*t al. , Nat. Phys. **7**, 1914 (2011).

[18] Xia et al., Nature Physics 5, **398** (2009)

[19] H. Zhang *e*t al., Nat. Phys. **5**, 438 (2009).

[20] Zhang *e*t al., Nat. Phys. **1270**, (2009).

[21] Y. Zhang *e*t al., Nat. Phys. **6**, 584, (2010).

[22] L. Fu, C. L. Kane, and E. J. Mele, Phys. Rev. Let. **98**, 106803 (2007).

[23] H.-Z. Lu *e*t al. Phys. Rev. B **81**, 115407 (2010).

[24] Q. Liu, C.-X. Liu, C. Xu, X.-L. Qi, and S.-C. Zhang, Phys. Rev. Lett. **102**, 156603(2009).

[25] Stanford Education, `http://www-ssrl.slac.stanford.edu/newsletters/headlines/headlines_08-10.html`

[26] C.-Z. Chang *e*t al., Science **340** 6129, (2013).

[27] R. Yu *e*t al., Science textbf329 5987, (2010).

[28] X.-L. Qi *e*t al. Science **323**. 1184 (2009).

[29] R. Li, J. Wang, X.-L. Qi and S.-C. Zhang, Nat. Phys. **6** 1534, (2010).

[30] L. Fu and C. L. Kane, Phys. Rev. Lett. **100**, 096407 (2008).

[31] X.-L. Qi and S.-C. Zhang,Rev. Mod. Phys. **83**, 1057 (2011).

[32] D. Hsieh et al., Nature(London) **460**, 1101 (2009).

[33] T. Hanaguri, K. Igarashi, M. Kawamura, H. Takagi, and T. Sagasawa, Phys. Rev. B **82**, 081305 (2010).

[34] X.-L. Qi, T. L. Hughes, and S.-C. Zhang, Phys. Rev. B **78**, 195424 (2008).

[35] A. M. Essin, J. E. Moore, and D. Vanderbilt, Phys. Rev. Lett. **102**, 146805 (2009).

[36] R. R. Biswas and A. V. Balatsky, Phys. Rev. B **81**, 233405 (2010).

[37] R. Yu, W. Zhang, H.-J. Zhang, S.-C. Zhang, X. Dai and Z. Fang, Science **329**, 61 (2010).

[38] J.-H. Jiang and S. Wu, Phys. Rev. B **83**, 205124 (2011).

[39] T. Yokohama, Phys. Rev. B **84**, 113407 (2011).

[40] J.-J. Zhu, D.-X. Yao, S.-C. Zhang, and K. Chang, Phys. Rev. Lett. **106**, 097201 (2011).

[41] D. A. Abanin and D. A. Pesin, Phys. Rev. Lett. **106**, 136802 (2011).

[42] V. N. Men'shov, V. Tugushev, and E. Chulkov, JETP Lett. **94**, 629 (2011).

[43] A. Nunez and J. Fernndez-Rossier, Solid State Commun. **152**, 403 (2012).

[44] T. Habe and Y. Asano, Phys. Rev. B **85**, 195325 (2012).

[45] Y. L. Chen *e*t al., Science **329**, 659 (2010).

[46] L. A. Wray *e*t al., Nat. Phys. **7**, 32 (2010).

[47] C.-Z. Chang, J.-S. Zhang, M.-H. Liu, Z.-C. Zhang, X. Feng, K. Li, L.-L. Wang, X. Chen, X. Dai, Z. Fang et al. , arXiv:1108.4754.

[48] J. Honolka, A. A. Khajetoorians, V. Sessi, T. O. Wehling, S. Stepanow, J.-L. Mi, B. B. Iversen, T. Schlenk, J. Wiebe, N. Brookes et al. , Phys. Rev. Lett. **108**, 256811 (2012).

[49] M. R. Scholz, J. Sánchez-Barriga, D. Marchenko, A. Varykhalov, A. Volykhov, L. V. Yashina, and O. Rader, Phys. Rev. Lett, **108**, 256810 (2012).

[50] T. Valla, Z.-H. Pan, D. Gardner, Y. S. Lee, and S. Chu, Phys. Rev. Lett. **108** (2012).

[51] S.-Y. Xu, L. A. Wray, N. Alidoust, Y. Xia, M. Neupane, C. Liu, H.-W. Ji, S. Jia, R. J. Cava and M. Z. Hasan, Nature Physics **8**, 616 (2012).

[52] T. M. Schmidt, R. H. Miwa, and A. Fazzio, Phys. Rev. B **84**, 245418 (2011).

[53] C.-X. Liu, X.-L. Qi, H. J. Zhang, X. Dai, Z. Fang, and S.-C. Zhang Phys. Rev. B **82**, 045122 (2010).

[54] P. G. Silvestrov, P. W. Brouwer, and E. G. Mishchenlo, Phys. Rev. B 86, 075302 (2012).

[55] J. Vleck, *The Theory of Electronic and Magnetic Susceptibilities* (Oxford University Press, London, 1932).

[56] Y. S. Hor, A. Richardella, P. Roushan, Y. Xia, J. G. Checkelsky, A. Yazadani, M. Z. Hasan, N. P. Ong, and R. J. Cava, Phys Rev. B **79**, 195208 (2009).

[57] T. Dietl, H. Ohno, F. Matsukura, J. Cibert, and D. Ferrand, Science **287**, 1019 (2000).

[58] L. Brey and G. Gómez-Santos, Phys. Rev. B **68**, 115206 (2003).

[59] M. J. Calderón, G. Gómez-Santos, and L. Brey, Phys.Rev. B **66**, 075218 (2002).

[60] M. Abolfath, T. Jungwirth, J. Brum, and A. H. MacDonald, Phys. Rev. B **63**, 054418 (2001).

[61] J. Fernández-Rossier and L. J. Sham, Phys. Rev. B **64**, 235323 (2001).

[62] P. M. Chaikin and T. C. Lubensky, Principles of Condensed Matter Physics, (Cambridge University Press, London, 1995).

[63] L. Brey, H. A. Fertig, and S. Das Sarma, Phys. Rev. Lett. **99**, 116802 (2007).

[64] G. Rosenberg and M. Franz, Phys. Rev. B. **85**, 195119 (2012).

[65] Z. Salman, E. Pmjakushina, V. Pmjakushina, A. Kanigel, K. Chashka, K. Conder, E. Morenzoni, T. Prokscha, K. Sedlak and A. Suter, ArXiv: 1203.4850.

[66] D. Khomskii, Physics 2, 20 (2009).

[67] N. Spaldin, S.-W. Cheong, R. Ramesh, Physics Today, (2010).

[68] Frank Wilczek, Phys. Rev. Lett. 58, 17991802 (1987).

[69] Hehl *e*t al., Physical Review A **77**, 022106 (2008).

[70] A. Shuvaev *e*t al., Phys. Rev. Lett. **111** 227201, (2013).

[71] Pimenov *e*t al., Nature Physics doi:10.1038/nphys212 (2006).

[72] N. Kida *e*t al., Phys. Rev. B **80**, 220406, (2009).

[73] M. Mochizuki and N. Nagaosa , Phys. Rev. Lett. **105**, 147202, (2010).

[74] Y. Ando, ArXiv e-prints (2013), 1304.5693.

[75] R. R. Nair, P. Blake, A. N. Grigorenko, K. S. Novoselov, T. J. Booth, T. Stauber, N. M. R. Peres, and A. K. Geim, Science 320, 1308 (2008)

[76] T. Stauber, N. M. R. Peres, and A. K. Geim, Phys. Rev.B **78**, 085432 (2008).

[77] Z. Li and J. P. Carbotte, Phys. Rev. B **87**, 155416 (2013).

[78] X. Xiao and W. Wen, Phys. Rev. B **88**, 045442 (2013).

[79] D. Schmeltzer and K. Ziegler, ArXiv e-prints (2013),1302.4145.

[80] N.M. Peres and J. E.Santos, Journal of Physics: Condensed Matter **25**, 305801 (2013).

[81] A. D. LaForge, A. Frenzel, B. C. Pursley, T. Lin, X. Liu, J. Shi, and D. N. Basov, Phys. Rev. B **81**, 125120 (2010).

[82] P. Di Pietro, F. M. Vitucci, D. Nicoletti, L. Baldassarre, P. Calvani, R. Cava, Y. S. Hor, U. Schade, and S. Lupi, Phys. Rev. B **86**, 045439 (2012).

[83] A. Akrap, M. Tran, A. Ubaldini, J. Teyssier, E. Giannini, D. van der Marel, P. Lerch, and C. C. Homes, Phys. Rev. B **86**, 235207 (2012).

[84] K. W. Post, B. C. Chapler, L. He, X. Kou, K. L. Wang, and D. N. Basov, Phys. Rev. B **88**,075121 (2013).

[85] A. G. Grushin and A. Cortijo, Phys. Rev. Lett. **106**, 020403 (2011).

[86] W.-K. Tse and A. H. MacDonald, Phys. Rev. Lett. **105**, 057401 (2010).

[87] W.-K. Tse and A. H. MacDonald, Phys. Rev. B **84**, 205327 (2011).

[88] A. Karch, Phys. Rev. Lett. **103**, 171601 (2009).

[89] M.-C. Chang and M.-F. Yang, Phys. Rev. B **80**, 113304 (2009).

[90] C.-Z. Chang *e*t al. Science **340**, 167 (2013).

[91] R. Valdes Aguilar, A. V. Stier, W. Liu, L. S. Bilbro, D. K. George, N. Bansal, L. Wu, J. Cerne, A. G. Markelz, S. Oh, et al., Phys. Rev. Lett. **108**, 087403 (2012).

[92] G. S. Jenkins, A. B. Sushkov, D. C. Schmadel, M.-H. Kim, M. Brahlek, N. Bansal, S. Oh, and H. D. Drew, Phys. Rev. B **86**, 235133 (2012).

[93] R. Shimano *e*t al., Nat Commun. **4** 1841 (2013).

[94] J. Wang, B. Lian, H. Zhang, and S.-C. Zhang, Phys. Rev. Lett. **111**, 086803 (2013).

[95] H.-Z. Lu, A. Zhao, and S.-Q. Shen, Phys. Rev. Lett. **111**, 146802 (2013).

[96] J. Linder, T. Yokoyama, and A. Sudbø, Phys. Rev. B **80**, 205401 (2009).

[97] Y. Zhang *e*t al., Nature Physics **6**, 584 (2010).

[98] H.-Z. Lu *e*t al., Phys. Rev. B **81**, 041307 (2010).

[99] C.-X. Liu, H. Zhang, B. Yan, X.-L. Qi, T. Frauenheim, X. Dai, Z. Fang, and S.-C. Zhang, Phys. Rev. B **81**, 041307 (2010).

[100] H. Zhang, *e*t al., Nature Phys. **5**, 438 (2009).

[101] M. Lasia and L. Brey, Phys. Rev. B **86**, 045317 (2012).

[102] D.-H. Lee, Phys. Rev. Lett. **103**, 196804 (2009).

[103] O. Vafek, Phys. Rev. B **84**, 245417 (2011).

[104] L. Brey and H. A. Fertig, Phys. Rev. B **89**, 085305 (2014).

[105] G. Giuliani and G. Vignale, Quantum Theory of the Electron Liquid (Cambridge University Press, 2005), 1st ed.

[106] T. Stauber and G. Gomez-Santos, Phys. Rev. B **82**, 155412 (2010).

[107] T. Stauber, P. San-Jose, and L. Brey, New Journal of Physics **15**, 113050 (2013).

[108] P. B. Allen, Conceptual Foundations of Material Properties: A standard model for calculation of ground and excited state properties. (M.L.Cohen and S.G.Loiiue Eds.Elsevier, Amsterdam, 2006).

[109] V. P. Gusynin, S. G. Sharapov, and J. P. Carbotte, Phys. Rev. B **75**, 165407 (2007).

[110] S. H. Abedinpour, G. Vignale, A. Principi, M. Polini, W.-K. Tse, and A. H. MacDonald, Phys. Rev. B **84**, 045429 (2011).

[111] E. Prada, P. San-Jose, L. Brey, and H. Fertig, Solid State Communications **151**, 1075 (2011).

[112] Wen-Yu Shan, Hai-Zhou Lu and Shun-Qing Shen, New Journal of Physics 12 (2010).